Mesure de la section efficace différentielle de production des bosons W et de l'asymétrie de charge avec l'expérience ATLAS à l'énergie dans le centre de masse de $\sqrt{s}$=7 TeV

Dimitra Tsionou

The University Of Sheffield.

UNIVERSITÉ DE GRENOBLE

THÈSE

Pour obtenir le grade de

DOCTEUR DE L'UNIVERSITÉ DE GRENOBLE

préparée dans le cadre d'une cotutelle entre l'*Université de Grenoble* et l'*Université de Sheffield*

Spécialité : **Physique Subatomique et Astroparticules**

Arrêté ministériel : le 6 janvier 2005 -7 août 2006

Présentée par

Dimitra TSIONOU

Thèse dirigée par **Lucia Di Ciaccio** et **Efstathios Paganis**

préparée au sein des **Laboratoire d'Annecy-le-Vieux de Physique des Particules** et **Université de Sheffield**
dans **l'École Doctorale de Physique**

Mesure de la section efficace différentielle de production de bosons W et de l'asymétrie de charge avec l'expérience ATLAS à l'énergie dans le centre de masse de √s=7 TeV

Thèse soutenue publiquement le **24 juillet 2012**
devant le jury composé de :

M. David Charlton
Université de Birmingham, Examinateur
M. Davide Costanzo
Université de Sheffield, Examinateur
Mme. Lucia Di Ciaccio
Université de Savoie - LAPP, Directrice de thèse
Mme. Lydia Fayard-Iconomidou
LAL - Université d'Orsay, Rapporteur
M. Paolo Iengo
Université de Naples, Examinateur
M. Yannis Karyotakis
LAPP - Université de Savoie, Président du jury
M. Efstathios Paganis
Université de Sheffield, Directeur de thèse
M. Roberto Tenchini
Université de Pisa, Rapporteur

Université Joseph Fourier / Université Pierre Mendès France / Université Stendhal / Université de Savoie / Grenoble INP

Measurement of the Differential Production Cross Section of W Bosons and Charge Asymmetry at $\sqrt{s} = 7$ TeV with the ATLAS Detector

Dimitra TSIONOU

A thesis submitted for the degree of Doctor of Philosophy in Physics

September 2012

University of Sheffield

Measurement of the Differential Production Cross Section of W Bosons and Charge Asymmetry at $\sqrt{s} = 7$ TeV with the ATLAS Detector

Dimitra TSIONOU

A thesis submitted for the degree of Doctor of Philosophy in Physics

for the joint program between

Université de Grenoble

Laboratoire d' Annecy-le-Vieux de Physique de Particules

and

University of Sheffield - Department of Physics and Astronomy

Supervisors:

Lucia Di Ciaccio — Université de Savoie/LAPP
Stathes Paganis — University of Sheffield

September 2012

To my family

ABSTRACT

This document presents a measurement of the production cross section of W bosons and of its charge asymmetry in proton-proton collisions at a centre of mass energy of 7 TeV with the ATLAS detector. These measurements provide information on the momentum fraction of the protons carried by the partons contributing to the W production and therefore allow to better understand the parton distribution functions of the proton.

The W candidate events are selected in the $W \to e\nu$ decay mode. The LAr electromagnetic calorimeter plays an important role in the detection of electrons and the author has worked on the on-line energy reconstruction in the LAr detectors. A subject which is treated in some detail is the evaluation of the charge misidentification rates for electrons and positrons. This is a key ingredient for charge related measurements such as the W charge asymmetry.

In this document, the W production cross section times the branching ratio is studied inclusively, as a function of the lepton pseudorapidity and as a double differential measurement as a function of the lepton pseudorapidity and transverse energy. The charge asymmetry measurement is presented as a function of the lepton pseudorapidity and as a double differential measurement as well. The data were recorded by the ATLAS detector in 2011 and correspond to 4.7 fb^{-1}.

RÉSUMÉ

Ce manuscrit présente une mesure de la section efficace de production des bosons W et de l'asymétrie de charge dans les collisions proton-proton avec l'expérience ATLAS à une énergie dans le centre de masse de 7 TeV. Ces mesures posent des contraintes sur la fraction d'impulsion des protons portée par les partons qui contribuent à la production des bosons W et donc elles permettent d'ameliorer notre compréhension des fonctions de distribution de partons.

Dans l'analyse, les événements de signal sont sélectionnés dans le canal électronique $W \to e\nu$. Le calorimètre électromagnétique à Argon Liquide joue un rôle important pour la détection des électrons. L'auteur de cette thèse a travaillé sur la reconstruction en ligne de l'énergie dans les détecteurs à LAr. Un aspect important pour les mesures liées à la charge électrique, comme l'asymétrie de charge du boson W, est l'évaluation du taux de misidentification de la charge pour des électrons et des positons.

Dans ce manuscrit, la section efficace de production de bosons W multipliée par le rapport de branchement est présentée de façon inclusive, en fonction de la pseudorapidité du lepton, et comme mesure différentielle en deux dimensions (c'est à dire en fonction de la pseudorapidité et de l'énergie transverse du lepton). La mesure de l'asymétrie de charge est aussi présentée en fonction de la pseudorapidité du lepton uniquement et en fonction de la pseudorapidité et de l'énergie transverse du lepton. Les données ont été enregistrées par l'expérience ATLAS en 2011 et correspondent à 4.7 fb^{-1}.

ACKNOWLEDGEMENTS

This work would not have been possible without the help and the support of a lot of people. First of all, I would like to thank my supervisor Lucia Di Ciaccio for the time she invested in me, her encouragement throughout these years, her immediate response everytime I needed her help and an "encadrement" that fitted my personality in the best possible way, and my supervisor Stathes Paganis for his support from the moment I started my thesis and the dynamic first year that was vital for my following work. They were both so willing to share their knowledge with me. During the hard times of the thesis, they were always supportive and caring for my well-being. I would also like to thank my professor Chara Petridou who introduced me to particle physics and motivated me to start this thesis as well as for her concern all this time.

I am also indebted to Emmanuel Sauvan, Corinne Goy, Vincenzo Lombardo, Isabelle Wingerter-Seez, Remi Lafaye and Alain Bazan as well as the rest of the ATLAS members for always being there to discuss on detector performance and physics. I would like to thank Matt Robinson as well for his priceless help on technical issues. I could not forget the director Yannis Karyotakis who welcomed me at LAPP and the secretarial department, especially Chantal Vallée for being so efficient and gentle. I would like to show my gratitude to Lydia Fayard-Iconomidou and Roberto Tenchini for accepting to be the "rapporteurs" for this thesis as well as Dave Charlton, Yannis Karyotakis, Davide Costanzo and Paolo Iengo for accepting to be in my "jury de thèse".

I am grateful to two people I got to know during my first year in Sheffield, Christos Anastopoulos and Nicolas Kerschen for their patience, their help and for always being there when I needed them. I would also like to thank Simon Owen and Xu Da who started their thesis at Sheffield the same year as me and accompanied me to the various student activities including the RAL summer school.

During the following years at LAPP, I met a lot of fellow students and researchers that made life in Annecy much more enjoyable. First of all, my

officemates Iro Koletsou and Maud Schwöerer for making my daily life much more pleasant They are amazing people: they never complained about the piles of papers on my desk and even though we were in the same office all day they would still invite me for dinner or go out on weekends! The list gets longer with Mayuko who is always very eager to help, Olivier who always stopped by my office for a small chat, Matthieu who is one of the most patient people I have ever met, Louis with his amazing driving skills, Oanh who apart from her thesis also takes care of her two year-old daughter, Ludovica, the fellow mediterranean student, with whom we tried to discover the night life in Annecy and the newest members of the group Elisabeth and Houry.

But apart from the ATLAS group there were and still are many interesting people at LAPP and LAPTh (and not only): Armand, Loïc, Guillaume C., Timur, Florent, Plamen who were there before me, Gwénaële the only non-ATLAS female we used to hang out with, the students who started their thesis the same year as me Guillaume D., Florian and Timothée, the new students Guilhem and Laurent who gradually took over organising "des sorties thésards" and of course Caroline and Bénédicte who have been so kind and friendly all this time.

Last but not least, θα ήθελα να ευχαριστήσω την οικογένειά μου που ακόμα κι αν ήταν στην Ελλάδα ήταν πάντα δίπλα μου. Οι γονείς μου και οι αδερφές μου με στήριξαν όλο αυτό το διάστημα ακόμα και όταν ήμουν κουρασμένη και πίστευα ότι δε θα τα καταφέρω. Φυσικά ως κλασική ελληνική οικογένεια, μιλούσαμε στο τηλέφωνο σε καθημερινή βάση!

Θέλω επίσης να ευχαριστήσω τους φίλους μου και ιδιαίτερα τη Μαρία, τη Βάσω και τον Κώστα που με δέχονται όπως είμαι και κυρίως γι αυτό που είμαι. Χάρη σ΄ αυτούς πέρασα ωραία φοιτητικά χρόνια και τους είμαι ευγνώμων για τα γέλια που έχουμε κάνει κι ελπίζω θα συνεχίσουμε να κάνουμε!

Contents

1 Theoretical Introduction **1**

1.1 The Standard Model Theory 1

1.1.1 The Theory of Electromagnetic Interactions 2

1.1.2 The Theory of the Strong Interactions 3

1.1.3 The Theory of the Electroweak Interactions 3

1.1.4 Higgs mechanism 5

1.2 W physics and Parton Density Functions 5

1.2.1 Factorisation theorem 5

1.2.2 Parton Distribution Functions 6

1.2.3 W Production in pp Collisions 9

1.2.4 Decay of W Bosons 11

1.2.5 Overview of Past W Cross-section Measurements 12

1.2.6 Overview of Past W Asymmetry Measurements 13

2 The ATLAS detector **16**

2.1 Detector Overview 17

2.2 Inner Detector 18

2.3 Calorimetry 21

2.3.1 LAr Electromagnetic Calorimeter 21

2.3.2 Hadronic Calorimeter 24

2.4 Muon Spectrometer 26

2.5 Magnet System 30

2.6 Trigger 30

3 Signal Reconstruction in the LAr Calorimeters **33**

3.1 LAr Calorimeter channel structure 33

3.2 LAr Calorimeter Readout 34

3.2.1 LAr calorimeter front-end boards 34

3.2.2 LAr electronic calibration 38

3.2.3 LAr calorimeter back-end electronics 38

3.3 Digital Signal Processor 39

3.3.1 Principle of the Calculations 39

3.3.2 DSP Constants and Computations 41

3.3.3 Packing of the Input 43

3.3.4 Packing of the Results 43

3.4 Role of the DSP computations 44

3.5 Validation of the DSP Computations 45

3.5.1 Offline Test Results 46

3.5.2 Validation during collision runs 47

3.5.3 Specific examples of DSP code validation and improvements 48

4 Performance Studies **52**

4.1 Electromagnetic Cluster Reconstruction 53

4.1.1 Sliding-Window Clustering 53

4.2 Electron Reconstruction 54

4.3 EM Cluster Energy Calibration 54

4.4 In-situ Electron Calibration 56

4.5 Electron Identification 57

4.6 Electron Isolation 60

4.7 Charge Identification 60

4.7.1 Method and Analysis Selection 60

4.7.2 QCD Background Evaluation 63

4.7.3 Charge (Mis)Identification Results 65

4.8 E_T^{miss} Reconstruction 74

4.8.1 Calculation and Calibration of the E_T^{miss} calorimeter term 74
4.8.2 Calculation of the E_T^{miss} muon term 75
4.8.3 E_T^{miss} resolution 76
4.8.4 E_T^{miss} Linearity in $W \to e\nu$ Events 76
4.9 Conclusion 80

5 $W \to e\nu$ Analysis **81**
5.1 Event Selection 81
5.1.1 Event Preselection Requirements 81
5.1.2 $W \to e\nu$ Selection 82
5.2 Electroweak Background Estimation 84
5.3 QCD background estimation for the $W \to e\nu$ selection 86
5.3.1 Selection of the QCD sample 87
5.3.2 Measuring the signal isolation efficiencies ε_{sig} 88
5.3.3 Measuring the number of candidate events 90
5.3.4 Results of the QCD background estimation 90

6 W cross-section Measurement and Charge Asymmetry **94**
6.1 W cross-section Measurement 94
6.1.1 Method 94
6.1.2 C_W Correction Factors 96
6.1.3 C_W Systematic Uncertainties 98
6.1.4 Systematic Uncertainties from the Number of W Candidate Events . . . 102
6.1.5 Charge Misidentification Correction 103
6.2 W Cross-section Results 104
6.3 W Charge Asymmetry Measurement 110
6.4 Conclusion 114

7 Double Differential Measurement **115**
7.1 Analysis 115
7.2 W Cross-section Measurement 119

7.3 W Charge Asymmetry Measurement 122
7.4 Conclusion 123

Bibliography **124**

List of Figures

1.1 Table of the elementary fermions and of gauge bosons of the three interactions in the Standard Model [1]. 2

1.2 Measurements of the strong coupling constant α_s as a function of the energy scale from a number of different experiments [6]. 4

1.3 Graphical representation of the potential energy of a complex field φ. The minima correspond to a non-zero value of the energy and there is an infinite possible choices to minimise the energy. It is the choice of one of these minima that causes the spontaneous symmetry breaking. 6

1.4 Kinematic phase space of the ATLAS and CMS experiments in terms of x and Q^2 compared to the kinematic region of various previous experiments from fixed target and $p\bar{p}$ and ep colliders [14]. 7

1.5 Feynman representation of few diagrams describing the W^+ production. *Top row:* The first diagram corresponds to the leading-order while the last two correspond to next-to-leading order W^+ production. *Bottom row:* Representative Feynman diagrams for the next-to-next-to-leading order W production. 7

1.6 Parton distribution functions of the proton at next-to-leading order (NLO) for two different scales Q^2 as predicted by the MSTW collaboration. The band represents the 68% confidence level [15]. 8

1.7 Parton flavour decomposition of W^+ (*solid line*) and W^- (*dashed line*) total cross-sections in $p\bar{p}$ and pp colliders as a function of the centre of mass energy. In $p\bar{p}$ collisions the decomposition is the same for W^+ and W^- [18]. 9

1.8 Rapidity distributions for the W^- (*left*) and W^+ (*right*) production at the LHC at $\sqrt{s} = 14$ TeV. The distributions are shown for LO, NLO and NNLO as computed using the MRST PDF sets. Each distribution is symmetric in Y; only half of the rapidity range is shown in each case [19]. 10

1.9 Measured values of W cross-sections at TeVatron, $Sp\bar{p}S$, RHIC and ATLAS experiments compared to the NNLO prediction as a function of the centre of mass energy [27]. . . . 12

1.10 Rapidity distributions of W^+, W^- and the decay leptons for: *Left* $p\bar{p}$ collisions [33] and *Right* pp collisions without applying any kinematic requirements. 14

1.11 $D0$ muon charge asymmetry as a function of the muon pseudorapidity for two p_T ranges $20 < p_T^\mu < 35$ GeV and $p_T^\mu > 35$ GeV compared to the theoretical prediction of CTEQ6.6. The top right windows show the difference between the muon charge asymmetry and the central value of CTEQ6.6. The yellow band represents the uncertainty of the CTEQ6.6 prediction [32]. 14

1.12 CDF W charge asymmetry as a function of the W rapidity compared to the NLO and NNLO theory predictions [33]. 15

2.1 Cut-away view of the ATLAS detector. The dimensions of the detector are 25 m in height and 44 m in length. The overall weight of the detector is approximately 7000 tonnes [34]. 16

2.2 Two-dimensional view of a quarter-section of the ATLAS inner detector showing each of the major detector elements with the dimensions of the active regions and envelopes. The region very close to the interaction point is shown enlarged at the bottom of the picture [34]. 19

2.3 Drawing showing the sensors and structural elements crossed by a charged track in the barrel ID [34]. 19

2.4 Material distribution (X_0) at the exit of the ID envelope, including the services and thermal enclosures. The distribution is shown as a function of $|\eta|$ and averaged over φ. The breakdown indicates the contributions of external services and of individual sub-detectors, including services in their active volume [36]. 20

2.5 Cut-away view of the ATLAS calorimeter system [34]. 22

2.6 Sketch of a part of the barrel module where the different layers are clearly visible with the ganging of electrodes in φ. The granularity in η and φ of the cells of each of the three layers and of the trigger towers is also shown [37]. 24

2.7 Segmentation in depth and η of the tile-calorimeter modules in the central (left) and extended (right) barrels. The bottom of the picture corresponds to the inner radius of the tile calorimeter. The tile calorimeter is symmetric with respect to the interaction point [34]. 26

2.8 Schematic $R-\varphi$ (left) and $R-z$ (right) views of a part of the Hadronic End-Cap calorimeter. The semi-pointing layout of the readout cells is indicated by the dashed lines. Dimensions are in *mm* [34]. 27

2.9 Schematic diagram showing the three FCal modules located in the end-cap cryostat. The material in front of the FCal and the shielding plug behind it are also shown. The black regions are structural parts of the cryostat. The diagram has a larger vertical scale for clarity [34]. 27

2.10 Cut-away view of the ATLAS muon system [34]. 28

2.11 Barrel toroid as installed in the underground cavern; note the symmetry of the supporting structure. The temporary scaffolding and green platforms were removed once the installation was complete. The scale is indicated by the person standing in between the two bottom coils. Also visible are the stainless-steel rails carrying the barrel calorimeter with its embedded solenoid, which await translation towards their final position in the centre of the detector [34]. 31

2.12 Block diagram of the ATLAS trigger. Additional information is used for the HLT in order to reduce the trigger rate. 31

3.1 Geometry and structure of the barrel electrodes [37]. 35

3.2 Block diagram of the LAr readout electronics. The electrical circuit in the LAr is depicted at the bottom, followed above by the on-detector front-end electronics crate and at the top (left) by a schematic view of the readout crate with its ROD boards and TTC modules. In this diagram warm preamplifiers are located in the FEB. This is the case for the EM and FCal1 calorimeters while for the HEC the preamplifiers are located in the LAr. Also indicated at the middle and top (right) are the LAr front-end tower builder electronics and the interfaces to the L1 trigger system with its central trigger processor (CTP) [34]. . . . 36

3.3 Ionisation pulse in a LAr cell and FEB output signal after bi-polar shaping. Also indicated are the sampling points every 25 ns. During normal data-taking the signal is sampled 5 times (or 7 times for some cosmics runs). A maximum of 32 samples can be attained and is used for calibration purpose (OFCs) [39]. 37

3.4 Block diagram of the FEB architecture, depicting the data-flow for four of the 128 channels [34]. 37

3.5 *Top:* photograph of the ROD PU with its two clearly visible DSPs. The PU measures 120 mm $\times$ 85 mm. *Bottom:* block diagram of the PU board with two TMS320C6414 Texas Instruments DSPs [39]. 40

3.6 Comparison between the calibration (black) and physics pulse (red) for a middle cell in the EM barrel [42]. 42

3.7 Example of validation plots from events generated by the DspTest code. E_{online} is the cell energy computed by emulating the DSP response and E_{offline} the energy computed with full precision. 46

3.8 Example of validation plots from events generated by the DspTest code. T_{online} is the cell time computed by emulating the DSP calculation and T_{offline} the time computed using full precision. The distributions are within ± 10 ps apart from low energies and large times where the precision of the LUT dominates. A cut on the cell energy $E > 500$ MeV is applied. The *right* plot shows the difference between T_{offline} and T_{online} for the cases where T_{offline} is within ± 1 ns. 47

3.9 Distribution of $(Q_{\text{offline}} - Q_{\text{online}})/\sqrt{Q_{\text{offline}}}$ as a function of Q_{offline} obtained with the DspTest code. The values of this quantity are not within ± 1 due to saturation of certain quantities on the DSP (see paragraph 3.5.3). 48

3.10 Online monitoring plots of the DSP behaviour showing the difference between the E_{online} and E_{offline} for the four different energy ranges. The second plot shows a detailed view of the first two energy ranges where one can see that the ΔE is within the expected precision (1 MeV for the first energy range and 8 MeV for the second one). 49

3.11 Online monitoring plots of the DSP behaviour showing the distribution for the difference of T_{offline} and T_{online}. The majority of the events are within ± 10 ps. Larger differences are also observed because of the usage of the LUT. 49

3.12 Plot produced online during data-taking showing the correlation between Q_{offline} and Q_{online}. For the points that are not on the $Q_{\text{online}} = Q_{\text{offline}}$ line, saturation has occurred on the DSP computation as explained in paragraph 3.5.3. 50

4.1 Schematic view of an electromagnetic shower developing in the ATLAS LAr calorimeter. The shower may start developing before it reaches the presampler loosing some energy in the material in front of the calorimeter. Some part of the shower energy is lost in the material between the presampler and the first calorimeter layer. The "out-of-cluster energy" corresponds to the energy which is lost when the size of the cluster is smaller than the shower lateral extension. The "leakage energy" is the energy lost if the shower is not contained by the calorimeter depth [46]. 55

4.2 Expected fractional energy resolution of the EM calorimeter for electrons of different energies as a function of pseudorapidity [50]. 56

4.3 *Left*: The energy-scale correction factor α as a function of the pseudorapidity of the electron cluster derived from fits to $Z \to ee$ data [51]. *Right*: Reconstructed di-electron mass distributions for $Z \to ee$ decays when both electrons are in the barrel region after applying the baseline 2011 $Z \to ee$ calibration. The data are compared to the signal Monte Carlo expectation. The fits of a Breit-Wigner convolved with a Crystal Ball function are shown. The Gaussian width of the Crystal Ball function is given both for data and MC simulation [47]. 57

4.4 Efficiencies measured from $Z \to ee$ events and predicted by MC for the medium identification criteria *Left:* as a function of E_T (integrated over $|\eta| < 2.47$ excluding the transition region $1.37 < |\eta| < 1.52$) *Right:* as a function of η (integrated over $20 < E_T < 50$ GeV). The results for the data are shown with their statistical (inner error bars) and total (outer error bars) uncertainties. The statistical error on the MC efficiencies plotted as open squares is negligible. For clarity, the data and MC points are slightly displaced horizontally in opposite directions [51]. 59

4.5 Efficiencies measured from $Z \to ee$ events and predicted by MC for the tight identification criteria as a function of E_T (integrated over $|\eta| < 2.47$ excluding the transition region $1.37 < |\eta| < 1.52$) (*left*) and of η (integrated over $20 < E_T < 50$ GeV) (*right*). Compared to the medium efficiencies, the efficiencies for tight electrons are lower. [51]. 59

4.6 Schematic representation of the cone definition used for calorimetric isolation. 60

4.7 *Top row:* The distribution of the tag-probe mass for probe electrons* passing track quality identification level with $|\eta_{probe}| < 0.4$ is shown in the case of SS pairs (tag electron, probe electron) in the left plot and for OS pairs (tag electron, probe positron) in the right plot; *Bottom row:* Same distributions for the case where the probe electron* satisfies the loose++ identification requirements. The "shoulder" seen at around 60 GeV is due to the lepton kinematic cuts. 63

4.8 *Top row:* The tag-probe mass distribution for probe electrons* passing the medium++ identification level with $|\eta_{probe}| < 0.4$ is shown for SS pairs (tag electron, probe electron) in the left plot and for OS pairs (tag electron, probe positron) in the right plot; *Bottom row:* Same distributions for probe electrons* satisfying the tight++ identification requirements. The shoulder seen at ~ 60 GeV is caused by the kinematic cuts applied on the electron* selection. 64

4.9 *Left plot:* Template fit results on the tag-probe mass distribution using $Z \to ee$ Monte Carlo and a data-driven QCD sample for SS pairs (tag electron, probe electron) for probes satisfying the track quality requirements and $|\eta_{probe}| < 0.4$. Dots represent the data points. The histograms are normalised to the fit results; *Right plot:* Same distribution for OS pairs (tag electron, probe positron). 65

4.10 *Left plot:* Comparison between charge identification for (probe) electrons *(blue)* and (probe) positrons *(red)* passing the track quality requirements; *Right plot:* Charge misidentification for electrons and positrons at track quality level. 67

4.11 Plots showing the data - Monte Carlo comparison at track quality level for (a) charge misidentification using (-)- pairs [the brackets indicate the sign of the tag]; (b) charge misidentification using (+)+ pairs; (c) charge identification using (-)+ pairs; (d) charge identification using (+)- pairs. 68

4.12 *Left plot:* Comparison between charge identification and charge misidentification for electrons satisfying the track quality requirements (on the graph the values 1-(charge misidentification) are plotted); *Right plot:* Comparison between charge identification and charge misidentification for track quality positrons. 68

4.13 *Left plot:* Comparison between charge identification (OS measurement) for electrons (blue) and positrons (red) passing the loose++ identification; *Right plot:* Charge misidentification (SS measurement) for electrons and positrons at loose++ level. 69

4.14 Plots showing the data - Monte Carlo comparison at loose++ level for (a) charge misidentification using (-)- pairs [the brackets indicate the sign of the tag]; (b) charge misidentification using (+)+ pairs; (c) charge identification using (-)+ pairs; (d) charge identification using (+)- pairs. 69

4.15 *Left plot:* Comparison between charge identification and charge misidentification for loose++ electrons (on the plot the values 1-(charge misidentification) are plotted; *Right plot:* Comparison between charge identification and charge misidentification for loose++ positrons. 70

4.16 Comparison between charge identification rates for electrons (blue) and positrons (red) passing the medium++ identification. 70

4.17 Plots showing the data - Monte Carlo comparison at medium++ level for (a) charge identification using (-)+ pairs [the brackets indicate the sign of the tag]; (b) charge identification using (+)- pairs. 71

4.18 Comparison between medium++ probes and medium++ probes that have triggered the event (a) charge identification using (-)+ pairs [the brackets indicate the sign of the tag]; (b) charge identification using (+)- pairs. 71

4.19 Comparison between charge identification for electrons (blue) and positrons (red) passing the tight++ identification. 72

4.20 Plots showing the data - Monte Carlo comparison at tight++ level for (a) charge identification using (-)+ pairs [the brackets indicate the sign of the tag]; (b) charge identification using (+)- pairs. 72

4.21 E/p distribution comparison between data and Monte Carlo for all tight++ probes in the pseudorapidity region (a) $|\eta_{probe}| < 0.42$ (b) $1.52 < |\eta_{probe}| < 1.74$ (first bin after crack) and (b) $2.32 < |\eta_{probe}| < 2.47$ (last η bin). 73

4.22 Comparison between tight++ probes and tight++ probes that have triggered the event (a) charge identification using (-)+ pairs [the brackets indicate the sign of the tag]; (b) charge identification using (+)- pairs. 74

4.23 *Left plot:* distribution of E_T^{miss} as measured in a data sample of $Z \to ee$ candidates. The expectation from Monte Carlo simulation is superimposed and normalised to data, after each MC sample is weighted with its corresponding cross-section. The ratio of the data and the MC distribution is shown below the plot. *Right plot:* E_x^{miss} and E_y^{miss} resolution as a function of the total transverse energy in calorimeters for $Z \to ee$ events in data. The $\sum E_T$ is at the EM scale and E_x^{miss}, E_y^{miss} are scaled by the ratio $\sum E_T(EM)/\sum E_T$. Different calibration procedures of E_T^{miss} are compared. The curve is the fit to the resolution of RefFinal E_T^{miss}, and fit values are indicated for all E_T^{miss} calibration schemes used [52]. 77

4.24 Same plot as Fig. 4.23 for W candidate events. *Left plot:* Distribution of E_T^{miss} as measured in a data sample of $W \to e/nu$ candidates. *Right plot:* E_x^{miss} and E_y^{miss} resolution as a function of the total transverse energy in calorimeters for $W \to e/nu$ events in data. Different calibrations of E_T^{miss} are compared. The curve is the fit to the resolution of RefFinal E_T^{miss}, and fit values are indicated for all E_T^{miss} calibration schemes used [52]. 77

4.25 E_T^{miss} linearity and resolution as measured on simulated events. The Monte Carlo conditions correspond to the full 2011 data-taking. The selection includes only lepton requirements. 78

4.26 E_T^{miss} linearity as a function of p_T^{ν} measured on $W \to e\nu$ events. The left plot represents low pile-up conditions while the right plot high pile-up conditions. The linearity of E_T^{miss} is shifted to higher values for high pile-up conditions. 79

4.27 E_T^{miss} linearity (left) and resolution (right) after a selection including electron, E_T^{miss} and m_T^W requirements. Compared to Fig. 4.25 it is evident that the E_T^{miss} linearity is highly affected by the additional selection criteria. This is also seen in the right plot where the mean of the distribution is also shifted. The resolution of the E_T^{miss} is not significantly affected. 79

5.1 Efficiencies for the EF_e20_medium *circles*, EF_e22_medium *squares* and EF_e22vh_medium1 *triangles* triggers as a function of η_e and $p_{T,e}$ as measured on 2011 data. The error bars represent both statistical and systematic uncertainties [53]. 82

5.2 Distribution of the isolation variable $E_T^{cone}30$ for data, signal MC and QCD samples using the selected QCD sample. 88

5.3 Isolation efficiencies ε_{QCD} for electrons *(red)* and positrons *(blue)* as measured using a specially selected QCD sample. 89

5.4 Isolation efficiencies ε_{sig} for electrons *(red)* and positrons *(blue)* as measured on $Z \to ee$ data using a Tag&Probe method. The total uncertainty (statistical and systematic) is shown. 89

5.5 Number of QCD background events for electrons *(red)* and positrons *(blue)* before *top plot* and after *bottom plot* the isolation cut as computed using the described matrix method. The uncertainties shown are both statistical and systematic contributions from the error propagation of each term in eq. 5.4. 91

5.6 Distribution of the electron pseudorapidity (*top*) and E_T^{miss} (*bottom*) in the selected $W \to e\nu$ sample. The simulation is normalised to the data luminosity. The QCD background shapes are taken from background control samples with relaxed electron identification criteria (bottom) and are normalised to the total number of QCD events expected, as described in the text. 93

6.1 Purity of the signal sample in the pseudorapidity region used for the analysis. The purity is measured as the ratio of the number of generated and reconstructed events in a given bin divided by the number of reconstructed events in that bin. For illustration purposes only bins with purity greater than 0.1% are shown on the plot. 97

6.2 C_W correction factors for electrons (*red*) and positrons (*blue*). The error bars represent both statistical and systematic uncertainties. 97

6.3 Distributions of the z position of the reconstructed primary vertex for the Monte Carlo production used for 2011 analyses. Data (black dots) are compared to the simulation (hatched histograms), before (*left*) and after (*right*) applying the reweighting procedure [55]. 100

6.4 *Left plot:* Reconstruction efficiencies measured from $Z \to ee$ events and predicted by Monte Carlo as a function of the pseudorapidity. *Right plot:* Tight identification efficiencies measured from $W \to e\nu$ events and predicted by Monte Carlo as a function of the pseudorapidity [51]. 101

6.5 Charge identification efficiencies used to correct from the measured number of W^+ and W^- events to the true number of W^+ and W^- produced. 104

6.6 The comparison between the 2011 obtained results and the theoretical prediction. The data uncertainties include statistical, systematic and luminosity contributions while the theoretical uncertainties include the PDF and α_s errors. 105

6.7 The comparison between the 2011 obtained results extrapolated to the fiducial kinematic region used for the 2010 analysis and the 2010 ATLAS published results are shown for the electron channel and for the electron and muon channels combined. 106

6.8 The differential $\frac{d\sigma}{d|\eta|}$ cross-section measurements for W^+ and W^- are shown. The left plot shows the cross-section for the W production in each $|\eta|$ bin while the right plot shows the same results divided by the bin size. The luminosity uncertainty is not included. 107

6.9 The combined differential $d\sigma/d|\eta_l|$ cross sections, for W^+ (*left*) and W^- (*right*) are shown in the fiducial region and their comparison to the NNLO theory predictions using various PDF sets. The ratio of theoretical predictions to data is also shown. Theoretical points are displaced for clarity within each bin [57]. 108

6.10 Comparison between 2010 and 2011 cross-section results presented as a ratio of cross-sections for W^+ (*left plot*) and W^- (*right plot*). The 2011 results are extrapolated to the fiducial region used for the 2010 measurements. The comparison is shown for the 2010 electron channel and combined results. 108

6.11 Comparison between the measured and predicted differential cross-sections for the W^+ (*left plot*) and W^- (*right plot*) production. The predicted cross-sections are presented at next-to-leading order for the MSTW2008 and CT10 PDF sets. 109

6.12 Predictions for the ratio $r_s = 0.5(s+\bar{s})/\bar{d}$, at $Q^2 = 1.9\ \text{GeV}^2$, $x = 0.023$. Points: global fit results using the PDF uncertainties using the ATLAS W and Z 2010 measurements and the comparison to different PDF sets [58]. 109

6.13 Measured W charge asymmetry as a function of the lepton pseudorapidity $|\eta_e|$ compared to theoretical predictions. This measurement uses the full 2011 statistics. The kinematic requirements are $E_T^e > 25$ GeV, $p_T^\nu > 25$ GeV and $m_T^W > 40$ GeV. The transition region $1.37 < |\eta| < 1.52$ is excluded from the analysis. 111

6.14 W charge asymmetry measured by the ATLAS experiment in 2010 as a function of the lepton pseudorapidity $|\eta_l|$ compared with theoretical predictions calculated to NNLO. Theoretical points are displaced for clarity within each bin [57]. 112

6.15 *Left*: W charge asymmetry measured using the 2010 (*blue*) and 2011 (*red*) data respectively extrapolated to the same fiducial region. The 2010 measurement represents the combined electron and muon asymmetry measurements while the 2011 analysis includes only the electron measurement. *Right*: Comparison of the 2011 measurement to the theoretical prediction of MC@NLO using the MSTW2008 and CT10 PDFs at NLO. 112

6.16 CMS results showing the comparison of the measured lepton charge asymmetry to different PDF models for lepton $p_T > 25$ GeV/c (*top*) and lepton $p_T > 30$ GeV/c (*bottom*). The error bars include both statistical and systematic uncertainties. The PDF uncertainty band is corresponding to the 90% confidence interval (C.I.). The bin width for each data point is shown by the filled bars on the bottom. The data points are placed at the centre of pseudorapidity bins, except that for display purposes the first three data points are shifted $+0.025$ (-0.025) for electrons (muons) [59]. 113

6.17 *Left:* LHCb results of the W charge asymmetry in bins of lepton pseudo-rapidity compared to the MCFM prediction. The shaded area is the uncertainty arising from the MSTW08NLO PDF set [60]. *Right:* The lepton charge asymmetry from W boson decays in bins of absolute pseudorapidity for the three different experiments ATLAS, CMS and LHCb [61]. 113

7.1 Distribution of the isolation variable E_T^{cone30} for the data, signal MC and QCD sample for electrons with transverse energy $25 < E_T < 30$ GeV (*left plot*) and $40 < E_T < 50$ GeV (*right plot*). 116

7.2 Charge-blind identification rates for the pseudorapidity region $|\eta| < 0.21$ (*left*) and $2.18 < |\eta| < 2.47$ (*right*). The charge identification is slightly lower for low E_T electrons*. Similar results are obtained in the other η bins. 117

7.3 Purity of the signal sample for the E_T and $|\eta|$ bins used in this analysis. 117

7.4 C_W correction factors for electrons (*red*) and positrons (*blue*) as a function of the electron pseudorapidity for the four different E_T bins. The error bars represent both statistical and systematic uncertainties. 118

7.5 Double differential cross-section measurement for W^+ and W^- production. Each plot shows the cross-section as a function of the electron pseudorapidity for different bins of the electron transverse energy. The results are normalised to the bin size. The luminosity uncertainty is not included. 119

7.6 Double differential measurement for the W^+ cross-section and its comparison to the theoretical prediction. The MSTW2008 and CT10 PDF predictions are shown at NLO. The results are presented as a function of the positron pseudorapidity for four different E_T regions. 120

7.7 Double differential measurement for the W^- cross-section and its comparison to the theoretical prediction. The MSTW2008 and CT10 PDF predictions are shown at NLO. The results are presented as a function of the electron pseudorapidity for four different E_T regions. 121

7.8 Double differential W charge asymmetry measurement as a function of $|\eta|$ and E_T. In each of the plots the W charge asymmetry is shown as a function of the electron pseudorapidity for different bins of the electron transverse energy. Both statistical and systematic uncertainties are considered. The theoretical prediction given by the MSTW2008 (*blue*), CT10 (*red*) and HERAPDF1.5 (*green*) PDF sets is also shown. 122

List of Tables

2.1 Design performance of the ATLAS detector. Note that, high-p_T muons can be measured independently in the muon spectrometer and in the tracking system. The units for E and p_T are in GeV [34]. 17

2.2 Main geometrical parameters of the inner-detector system [34]. 21

2.3 Main parameters of the EM calorimeter system [34]. 23

2.4 Main parameters of Hadronic and Forward Calorimeter [34]. 25

2.5 Main parameters of the muon spectrometer. Numbers in brackets for the MDT's and the RPC's refer to the final configuration of the detector in 2009 [34]. 29

3.1 Thickness of the LAr gap and the absorber (lead) in the EM calorimeter [37]. 34

3.2 Packed constants that are loaded on the DSP ($f' = fR_1$). The energy, time and quality factor OFCs are scaled by 2^{n_a}, 2^{n_b} and 2^{n_h} respectively in order to have maximum precision when packed as 16-bit integers [41]. 44

3.3 Energy values and the precision for each energy range are presented [41]. 44

3.4 Ranges and online precision for energy, time and quality factor. ΔQ is defined as the difference between Q_{offline} and Q_{online}. 46

4.1 Definition of the variables used for loose++, medium++ and tight++ electron identification cuts for the region $|\eta| < 2.47$ [48]. 58

5.1 Triggers used for the $W \to e\nu$ analysis and the corresponding luminosity. The "vh" characters in the trigger name indicate that a requirement on the hadronic leakage was used to ensure a lower trigger rate while keeping a very high efficiency of the electron trigger. . . 82

5.2 Signal and background Monte Carlo samples as well as the generators used in the simulation. For each sample, the production cross-section multiplied by the branching ratio (BR), used for normalisation, is given. The electroweak W and Z cross-sections are calculated at NNLO, $t\bar{t}$ at approximate NNLO and the diboson cross-sections at NLO. The available luminosity of each sample is also given [54]. 85

5.3 Fraction of the electroweak background contributions expected in data and their statistical uncertainty computed using MC samples after the selection cuts described in Section 5.1. 85

5.4 Number of events before and after the final isolation cut given in units of 10^3. For the signal and the electroweak background contributions the numbers are extracted from simulation. The QCD events are obtained with the described data-driven technique. The errors shown are only statistical. 92

5.5 Number of events before and after the final isolation cut. The last column represents the sum of the signal Monte Carlo, the electroweak background Monte Carlo and the QCD background. The errors shown are only statistical. 92

6.1 Table summarising the systematic uncertainties considered for the inclusive C_W^- and C_W^+ correction factors. 98

6.2 Table summarising the main systematic uncertainties considered for the C_W^- correction factors for the differential measurement in bins of the electron pseudorapidity 99

6.3 Table summarising the main systematic uncertainties considered for the C_W^+ correction factors for the differential measurement in bins of the electron pseudorapidity 99

6.4 Cross-sections times the leptonic branching ratios for W^+ and W^- production within the fiducial region of the measurement. *Top*: The measured cross-sections using the full 2011 data are shown. The uncertainties denote the statistical (stat), the experimental systematic (syst) and the luminosity (lumi) uncertainties. *Bottom*: Theoretical prediction obtained using the FEWZ program at NNLO with the MSTW2008 PDF set. 105

6.5 Cross-sections times the leptonic branching ratios for W^+ and W^- production within the fiducial region of the measurement used for the 2010 analysis. *Top*: Results showing the ATLAS electron measurement performed using the 2010 data. *Middle*: Results showing the combined (electron and muon) ATLAS measurement performed using the 2010 data. *Bottom*: Results showing the measurement performed in this thesis extrapolated to the fiducial region of the 2010 measurement. The statistical (stat), experimental systematic (syst), the luminosity (lumi) uncertainties and acceptance (acc) uncertainties are shown. . 106

6.6 Table showing the asymmetry results as a function of the charged lepton pseudorapidity and its statistical and systematic uncertainties. 110

Chapter 1

Theoretical Introduction

The Standard Model of particle physics is a theory that describes the elementary particles and their interactions. It was developed during the 20th century and its theoretical formulation was finalised during the 1970s. The Standard Model theory is very successful: it has predicted many new particles that were later discovered (W and Z bosons, t quark, ...) and it describes remarkably well the experimental results observed until now [1].

In the beginning of this chapter, the Standard Model theory will be briefly described. In addition, a theoretical introduction on W physics and parton density functions will follow to motivate the analysis of this thesis.

1.1 The Standard Model Theory

There are four fundamental interactions in nature: electromagnetic, weak, strong and gravitational interactions. The first two interactions are "unified" in the electroweak model and with the addition of the strong interaction, they form the Standard Model of particle physics.

The elementary particles of the Standard Model are presented in Fig. 1.1. The quarks (u, c, t, d, s, b) are fermions of spin $\frac{1}{2}$ with a fractional electric charge of $+2/3$ or $-1/3$, as indicated in the figure. The t quark, the heaviest fermion, was the last one to be discovered by the CDF and D0 experiments in 1995. There are 6 leptons (e, μ, τ, ν_e, ν_μ, ν_τ). They are fermions of spin $\frac{1}{2}$ and three of them are electrically neutral. Each of these quarks and leptons has its own charge conjugate state, its antiparticle. In addition to quarks and leptons there are 12 bosons of spin 1 which are the carriers of the electromagnetic, weak and strong interactions. The photon is the carrier of the electromagnetic force and is massless. It interacts with any particle that has an electric charge. The $W^\pm$ and Z bosons are the carriers of the weak interactions and have a mass of ~ 80 GeV and ~ 91 GeV respectively. The carriers of the strong interactions are the

[1] There are reasons to believe that the Standard Model is only a low energy manifestation of a more fundamental theory. This aspect will not be treated here.

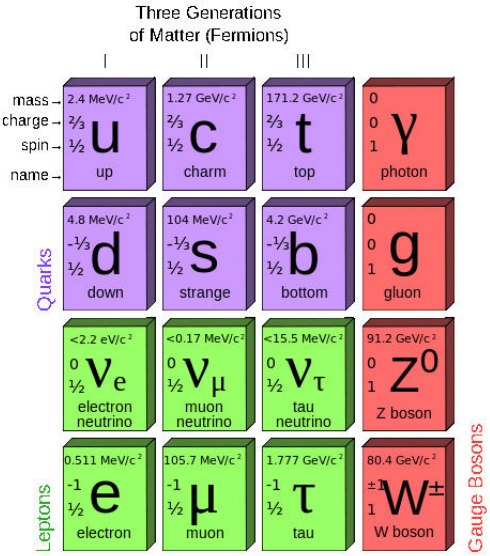

Figure 1.1: Table of the elementary fermions and of gauge bosons of the three interactions in the Standard Model [1].

gluons. There are 8 gluons that interact with particles carrying the strong charge called colour. The Standard Model is a quantum field theory where the elementary particles are represented by fields (spinor fields for the fermions and vector fields for the bosons [2].

1.1.1 The Theory of Electromagnetic Interactions

Quantum Electrodynamics (QED) is the field theory describing the electromagnetic interactions of particles. A fundamental aspect is the conservation of the electric charge which is related to the invariance of the theory under global gauge transformations. QED is also invariant under local gauge transformations of the fields represented by the group of unitary matrix $U(1)$. The langrangian which includes the description of the electromagnetic interaction between a charged fermion field, Ψ, of charge Q and a vector boson field, A_μ, is expressed as:

$$L = -\frac{1}{4}F_{\mu\nu}F^{\mu\nu} + \bar{\Psi}(i\gamma^\mu\partial_\mu - m)\Psi - A_\mu \cdot eQ(\bar{\Psi}\gamma^\mu\Psi) \tag{1.1}$$

where the first term describes the kinetic energy of the boson field (interpreted as the photon), the second term the fermion kinematics (including the fermion mass term) and the third term the interaction between the fermion and the photon field, A_μ.

A bosonic mass term of the form $\frac{1}{2}\mu_\gamma^2 A^\mu A_\mu$ in the lagrangian would break the local gauge invariance. The mass of the photon is $\mu_\gamma = 0$, therefore the gauge invariance is preserved and the range of the interaction is infinite.

The strength of an interaction is characterised by a coupling constant. The coupling con-

stant in QED is $g_e = \sqrt{4\pi\alpha}$.In appropriate units g_e is the fundamental charge (the charge of the positron).At low energy, the value of the α is $\frac{1}{137}$, the fine-structure constant [3].

1.1.2 The Theory of the Strong Interactions

A number of particles sensitive to the strong interactions (hadrons) were discovered before the 1960s. The results from deep inelastic scattering experiments showed that the hadrons are composed of effectively pointlike constituents. In particular, it was proposed that they are formed by partons that determine the hadron properties (valence quarks) and by virtual partons composed of quarks, antiquarks and gluons collectively called the sea. The hadrons are classified in two categories: the *baryons* composed of three valence quarks and the *mesons* composed of a quark-antiquark valence pair. The six quarks were discovered from the 1960s to 1995. Evidence of gluons, the gauge bosons of QCD, was found in e^+e^- collision events with the discovery of final states with three jets [5].

The discovery of the Δ^{++} baryon opened a puzzle. This particle is composed by three u quarks with exactly the same quantum numbers. This fact violates the Pauli principle. To preserve this principle, a new quantum number called "colour" was introduced giving to the quarks a new degree of freedom. This quantum number can assume three values called blue, red or green (antiblue, antired or antigreen for the antiquarks). The particles we observe, baryons and mesons, are colourless.

The introduction of the colour led to the construction of the Quantum Chromodynamics (QCD), the theory of the strong interaction. QCD is a quantum field theory, invariant under the local gauge transformations of the fields described by matrices belonging to the group $SU(3)$. The local gauge invariance introduces eight fields, the gluons. The gluons are massless but unlike the photon (which is neutral and cannot interact directly with other photons) they carry the colour charge and thus can interact with other gluons.

The strength of the interaction is characterised by the coupling constant $g_s = \sqrt{4\pi\alpha_s}$. Fig. 1.2 shows the dependence of α_s on the energy of the interaction. The long distance regime, relevant for low momenta ($Q \leq 1$ GeV), is characterised by a strong coupling $\alpha_s \sim O(1)$ which explains the fact that the quarks are confined in hadrons and cannot emerge as free particles. On the contrary, in the short distance regime, $Q \gg 1$ GeV, the coupling constant is $\alpha_s \ll 1$. The decrease of α_s with energy brings to the properties of the QCD the asymptotic freedom that allows to describe the high energy interactions between protons using perturbation theory in terms of scattering among quasi-free partons (quarks and gluons) [7].

1.1.3 The Theory of the Electroweak Interactions

After the discovery of the nuclear β decay, it appeared clear that a new interaction had to be added to explain this phenomenon. Given the observed lifetime, the interaction was called "weak". The

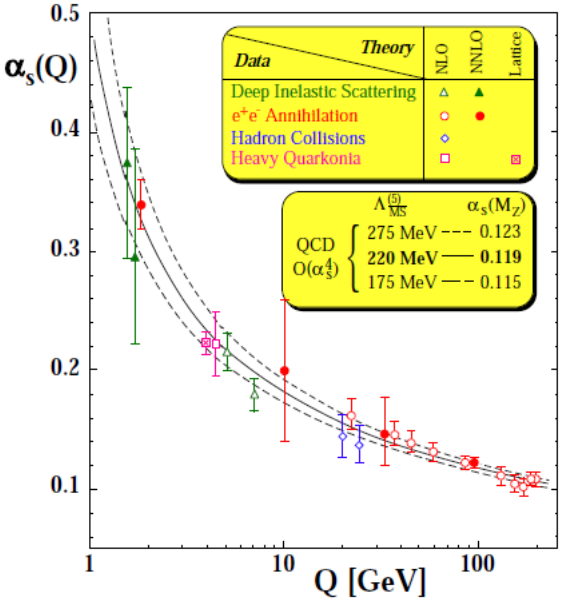

Figure 1.2: Measurements of the strong coupling constant α_s as a function of the energy scale from a number of different experiments [6].

experiment on ^{60}Co [8], showed for the first time that this new interaction, unlike the electromagnetic and strong interactions, violates the parity conservation. Several experiments showed that the weak interaction only acts on left-handed particles and on right-handed antiparticles. The first theory of the weak interaction was presented by Fermi. The theory was put in its present form by Glashow, Salam and Weinberg [9, 10, 11]. The Glashow-Salam-Weinberg model treats the weak and electromagnetic interactions as different manifestations of a single electroweak force. The electroweak interaction is invariant under local gauge transformations of the fields described by matrices forming the group $SU(2)_L \times U(1)$. The requirement of local gauge invariance introduces four massless fields of spin 1: W^1_μ, W^2_μ, W^0_μ with a coupling constant g (for the $SU(2)_L$) and B_μ with a different coupling constant g' (for the $U(1)$). The two physical bosons W^+ and W^- responsible for the charged current interactions are linear combinations of the first two fields:

$$W^\pm_\mu = \frac{1}{2}(W^1_\mu \mp W^2_\mu)$$

while the Z^0 boson and the photon which are the physical particles responsible for the neutral current interactions are a combination of the two neutral fields:

$$A_\mu = W^0_\mu \sin\theta_W + B_\mu \cos\theta_W$$

$$Z^0_\mu = W^0_\mu \cos\theta_W - B_\mu \sin\theta_W$$

where θ_W is the Weinberg angle and $\cos\theta_W = \frac{M_W}{M_Z}$. Bosonic mass terms ($\frac{1}{2}M^2_W W_\mu W^\mu$, $\frac{1}{2}M^2_B B_\mu B^\mu$) as well as fermionic mass terms ($m\Psi\bar{\Psi}$) would break the local gauge invariance $SU(2)_L \otimes U(1)$.

Therefore at this stage of the Standard Model construction all particles are massless [7].

1.1.4 Higgs mechanism

As mentioned earlier, the local gauge invariance $SU(2)_L \times U(1)$ implies that the W and Z bosons of the electroweak model as well as the fermions are massless. However, the W and Z masses have been measured and found to be $O(100)$ GeV. This problem along with the problem of the origin of the mass of quarks and leptons is solved by introducing the Higgs-Brout-Englert-Guralnik-Hagen-Kibble mechanism.

Mass terms in the langrangian appear thanks to the mechanism of the "spontaneous" breaking of the local gauge symmetry $SU(2)_L \otimes U(1)$. Four new scalar real fields in the form of a complex doublet are introduced:

$$\varphi = \begin{pmatrix} \varphi^+ \\ \varphi^0 \end{pmatrix} = \frac{1}{\sqrt{2}} \begin{pmatrix} \varphi_1 + i\varphi_2 \\ \varphi_3 + i\varphi_4 \end{pmatrix}.$$

The langrangian of this doublet contains a term interpreted as the potential energy of the φ field. As an example, fig. 1.3 shows the form of this potential energy. Its minimum value is non-zero. There is an infinite number of minima corresponding to $|\varphi| = \frac{\mu^2}{2\lambda} = \frac{u^2}{2}$, where μ and λ are two parameters of the potential and u is a chosen vacuum expectation value of one of the four fields. The choice of a particular minimum leads to the spontaneous symmetry breaking and to the appearance of mass terms for the W and Z bosons in the langrangian. Of the initial four degrees of freedom corresponding to the four scalar fields, three are used to give mass to the W^+, W^- and Z bosons. The remaining one results in a new boson of spin 0, the Higgs boson, which is at present actively searched at LHC. The masses of the W and Z are related by the following equations:

$$M_W = \frac{1}{2}ug \quad , \quad M_Z = \frac{1}{2}u\sqrt{g^2 + g'^2} \quad \text{and} \quad M_W = M_Z \cos\theta_W .$$

The Higgs field also gives masses to the fermions by a Yukawa interaction with the fermion fields.

The $U(1)$ symmetry and the $SU(3)$ colour symmetry remain unbroken and therefore their carriers, photon and gluons, remain massless [7].

1.2 W physics and Parton Density Functions

1.2.1 Factorisation theorem

According to the factorisation theorem [12], in proton-proton collisions the cross-section of a hard scattering $\sigma_{pp\to X}$ can be factorised into two contributions: a term representing the cross-section of the parton interaction and a term corresponding to the momentum distribution of the partons

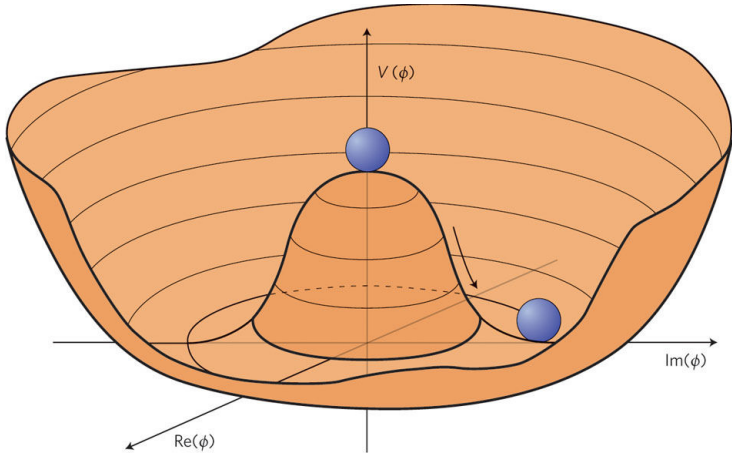

Figure 1.3: Graphical representation of the potential energy of a complex field φ. The minima correspond to a non-zero value of the energy and there is an infinite possible choices to minimise the energy. It is the choice of one of these minima that causes the spontaneous symmetry breaking.

inside the colliding protons (PDFs). Therefore the cross-section $\sigma_{pp\to X}$ can be written as:

$$\sigma_{pp\to X} = PDF \otimes \sigma_{hard\ scatter} = \sum_q \int dx_1 dx_2 f_q(x_1, Q^2) f_{\bar{q}}(x_2, Q^2) \otimes \hat{\sigma}_{q\bar{q}\to X} \tag{1.2}$$

where x_1 and x_2 are the momentum fractions of the protons carried by the partons q and $\bar{q}$ respectively and f_q ($f_{\bar{q}}$)represents the momentum fraction distribution of a parton q ($\bar{q}$) which depends also on the four momentum of the process Q^2. Given that at short distance (high energy regime) $\alpha_s \ll 1$, perturbation theory can be applied, the partonic cross-section can be expressed as a power series expansion of the α_s coupling constant:

$$\hat{\sigma}_{q\bar{q}\to X} = \underbrace{\hat{\sigma}_0}_{LO} + \underbrace{\alpha_s \hat{\sigma}_1}_{NLO} + \underbrace{\alpha_s^2 \hat{\sigma}_1}_{NNLO} + O(\alpha_s^3). \tag{1.3}$$

LO refers to the leading order, NLO to the next-to-leading order and NNLO to the next-to-next-to-leading order calculations. An example of different Feynman diagrams for the production of W bosons are shown in Fig. 1.5 for LO, NLO and NNLO.

1.2.2 Parton Distribution Functions

The parton distribution functions (PDFs) are defined as the probability of finding a parton in a proton with a certain momentum fraction x, at momentum transfer Q^2. The set of distributions $f_i(x, Q^2)$ describe how the momentum of the proton is shared between the individual partons ($f_i =$ valence quark, see quarks and gluons). Fig. 1.6 displays an example of $xf(x, Q^2)$ distributions for the valence quarks u and d, the sea quarks $\bar{u}$, $\bar{d}$, s, $\bar{s}$, b, $\bar{b}$ and the gluon g for two different scales $Q^2 = 10\ \text{GeV}^2$ and $Q^2 = 10^4\ \text{GeV}^2$. At low x, it is the gluon PDF that always dominates.

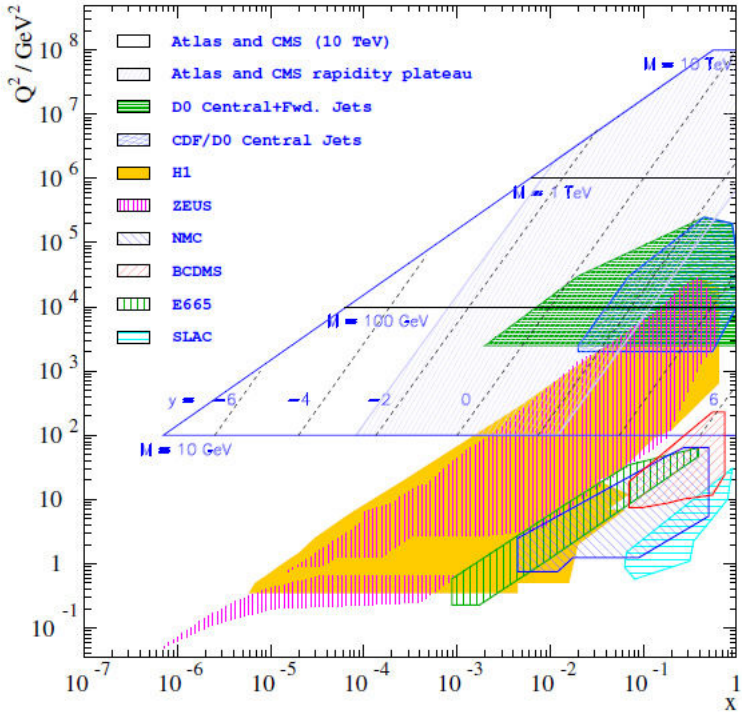

Figure 1.4: Kinematic phase space of the ATLAS and CMS experiments in terms of x and Q^2 compared to the kinematic region of various previous experiments from fixed target and $p\bar{p}$ and ep colliders [14].

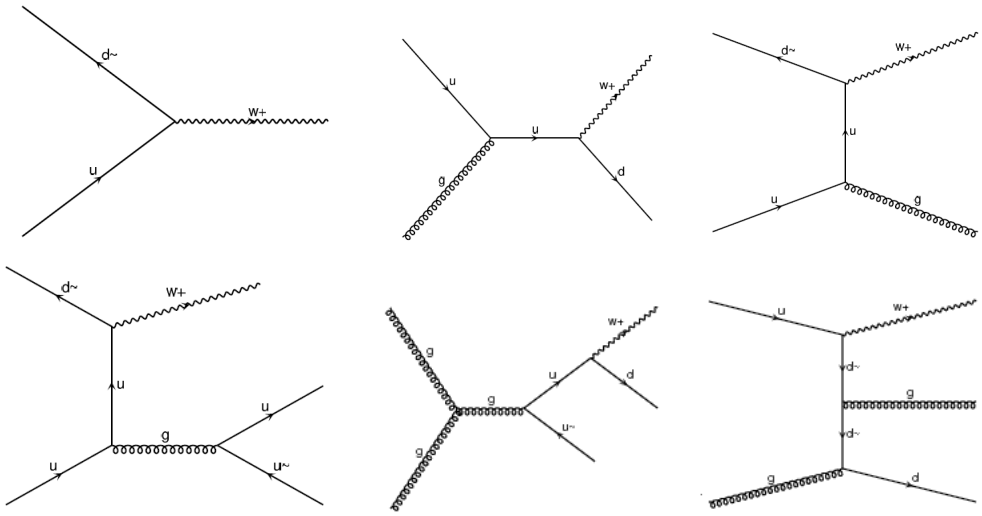

Figure 1.5: Feynman representation of few diagrams describing the W^+ production. *Top row:* The first diagram corresponds to the leading-order while the last two correspond to next-to-leading order W^+ production. *Bottom row:* Representative Feynman diagrams for the next-to-next-to-leading order W production.

At higher scales the contributions from the sea quarks and especially from the gluons become more important.

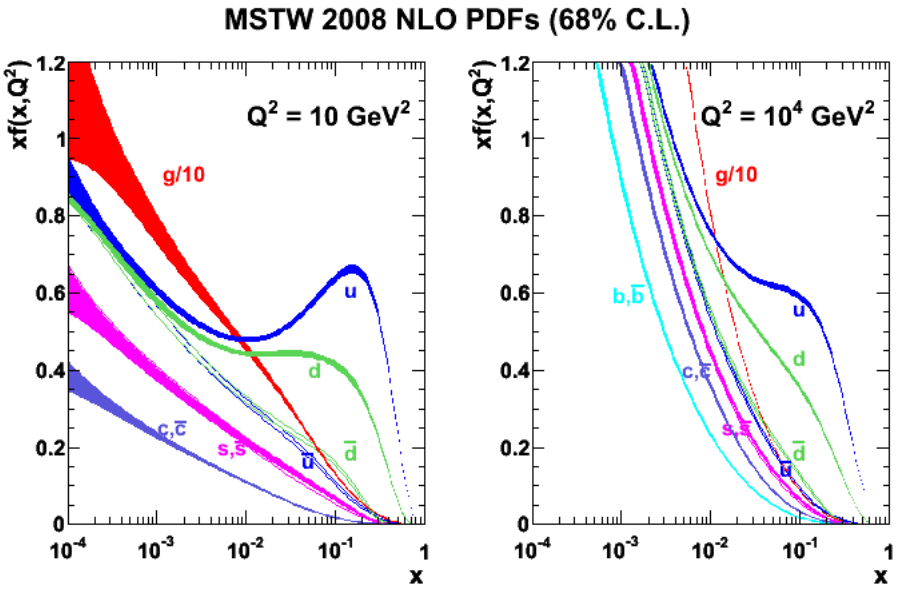

Figure 1.6: Parton distribution functions of the proton at next-to-leading order (NLO) for two different scales Q^2 as predicted by the MSTW collaboration. The band represents the 68% confidence level [15].

Perturbative QCD predicts the evolution of the PDF with Q^2 through the DGLAP equations [13]. However, the PDFs themselves are not calculated perturbatively but are derived by fitting the experimental data in fixed target and collider experiments.

Impact of PDF Uncertainties

At hadron colliders, the PDFs play an important role in calculating the cross-section of different processes. Their uncertainty induce a theoretical uncertainty on the predicted cross-section. For example the impact of the PDF uncertainties on the prediction of the Higgs production cross-section at LHC or of new physics cannot be ignored. In particular, the use of different PDF sets has an effect of 15% on the Higgs cross-section at $\sqrt{s} = 8$ TeV [16].

An underestimation of the PDFs and of their uncertainties could lead to false discoveries, and an overestimation could hide a genuine signal of new physics. As an example, the first measurements of high E_T di-jet production cross-section at TeVatron reported a significant excess over the prediction [17]. However, this excess was explained by an underestimation of the gluon PDF and its uncertainty.

Since for most of the kinematic region at LHC (Fig. 1.4), one relies on extrapolations of the PDFs fitted to measurements obtained at a lower centre of mass energy, it is necessary to further

constrain the PDFs using LHC data. Some of the measurements that can be used for that purpose are the Z and $W^{\pm}$ cross-sections as well as the W charge asymmetry that will be discussed later on.

1.2.3 W Production in pp Collisions

In pp colliders, at leading order the W bosons are produced from the annihilation of a quark-antiquark pair as shown in the first diagram of Fig. 1.5. Since the proton is composed of two u and one d valence quarks, it is more likely to have a $u\bar{d}$ interaction than a $d\bar{u}$ one. This results in a enhanced W^+ production compared to the W^-. The decomposition of the W^+ and W^- cross-sections in terms of the contribution from the scattering of different quarks is shown in Fig. 1.7 and Fig. 1.8 shows the W^+ and W^- differential cross-sections as a function of the rapidity y depending on the order of the calculation.

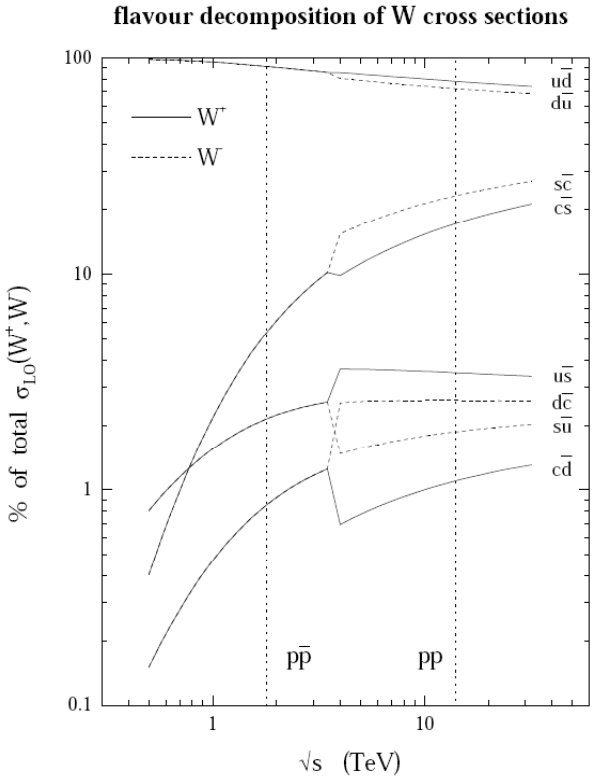

Figure 1.7: Parton flavour decomposition of W^+ (*solid line*) and W^- (*dashed line*) total cross-sections in $p\bar{p}$ and pp colliders as a function of the centre of mass energy. In $p\bar{p}$collisions the decomposition is the same for W^+ and W^- [18].

The rapidity of a particle (in particular of a W boson) is defined as:

$$y_W = \frac{1}{2}\ln\frac{E^W + p_z^W}{E^W - p_z^W} \tag{1.4}$$

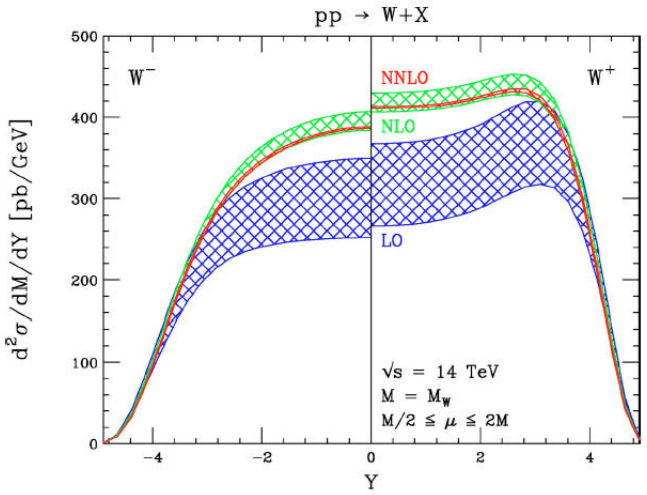

Figure 1.8: Rapidity distributions for the W^- (*left*) and W^+ (*right*) production at the LHC at $\sqrt{s} = 14$ TeV. The distributions are shown for LO, NLO and NNLO as computed using the MRST PDF sets. Each distribution is symmetric in Y; only half of the rapidity range is shown in each case [19].

where E is the particle energy and p_z is the particle momentum along the z-axis (in our case the z-axis is defined by the beam direction).

At first approximation, the quarks in the proton can be assumed to have no transverse momentum. In this case, the boost of the produced resonance along the z axis depends only on the difference between the momentum fractions x_1 and x_2 of the colliding quarks:

$$\beta_W = \frac{x_1 - x_2}{x_1 + x_2} \quad \text{and} \quad y_w = \frac{1}{2} \ln \frac{x_1}{x_2}. \tag{1.5}$$

The momentum fractions of the incoming quarks for a given W rapidity is therefore:

$$x_1 = \frac{M}{\sqrt{s}} e^{y_W} \quad \text{and} \quad x_2 = \frac{M}{\sqrt{s}} e^{-y_W} \tag{1.6}$$

where M is the energy of the process ($M^2 = Q^2$) and $\sqrt{s}$ the centre of mass energy of the collision. For W production ($M = M_W$) and for the LHC 2011 data-taking ($\sqrt{s} = 7$ TeV) at $y = 0$ (central rapidity) the two x values are equal to ~ 0.01. Moving away from central rapidity, one parton goes to lower x values and the other to higher x as illustrated in Fig. 1.4. Over the measurable rapidity range of the ATLAS experiment $|y_W| \leq 3$, the x values remain in the region of $0.0006 < x < 0.23$. According to Fig. 1.6, in this x region the contribution from the gluons is dominant followed by the contribution from the u and d quarks.

1.2.4 Decay of W Bosons

In practise, the particles which are measured are the decay products of the W bosons. This thesis will focus on the leptonic decay of the W to an electron (positron) and an antineutrino (neutrino) $W \to e\nu$. The branching ratio of the W leptonic decays is $(10.80 \pm 0.09\%)$ while the decay branching ratio of W to hadrons is higher $(67.60 \pm 0.27\%)$ [20]. The clean signature of the $W \to e\nu$ decay allows a very good detection and measurement of these events.

The W decays are governed by the $V-A$ structure of the weak charged interaction. As a consequence, the angular distribution of the charged lepton from the W decay in the W rest frame is not isotropic and the charged lepton is emitted preferentially in the direction opposite to the direction of the W spin orientation. At LHC at LO, the W is produced with $p_T = 0$ and in two possible states of helicity $\lambda = \pm 1$. Therefore at LO the differential cross-section in terms of the angle θ^*_W between the direction of the charged lepton in the W rest frame and the W direction in the laboratory frame is:

$$\frac{d\sigma}{d\cos\theta^*_{W,l}} \propto (1 + Q\lambda\cos\theta^*_{W,l})^2$$

where Q is the charge of the boson and λ is the W helicity.

To constrain the PDFs it would be better to use directly the W rapidity and transverse momentum and give the cross-sections as a function of y_W and p_T^W. However, since the neutrino of the W decay escapes detection it is hard to reconstruct the W momentum (magnitude and direction). For this reason, the charged lepton quantities are used to express the differential cross-section since they have a better resolution. In principle, the W transverse momentum can be reconstructed using the $\overrightarrow{p_T^{miss}}$ [2] variable which corresponds to the neutrino transverse momentum but this only provides information in the transverse plane.

Starting from the equation [3]:

$$(\tilde{p}_e + \tilde{p}_\nu)^2 = M_W^2 \tag{1.7}$$

the momentum of the neutrino along the z-axis can be calculated as:

$$p_z^\nu = \frac{-\beta \pm \sqrt{\beta^2 - 4\alpha\gamma}}{2\alpha} \tag{1.8}$$

where the terms α, β and γ correspond to [4]:

$$\alpha = p_{Te}^2$$

[2] The missing transverse momentum in an event is defined as $\overrightarrow{p_T^{miss}} = -\sum_{i=1}^{N} \overrightarrow{p_{T_i}}$ where N indicates the number of final state particles of the event.

[3] $\tilde{p}_e^\mu$, $\tilde{p}_\nu^\mu$ are the four-momenta of the electron and of the neutrino respectively: $\tilde{p}_e(E_e, p_{xe}, p_{ye}, p_{ze})$, $\tilde{p}_\nu(E_\nu, p_{x\nu}, p_{y\nu}, p_{z\nu})$.

[4] p_{Te} and $p_{T\nu}$ are the momenta of the electron and of the neutrino respectively in the plane orthogonal to the beam.

$$\beta = -(2(p_{x\nu}p_{xe} + p_{y\nu}p_{ye})p_{ze} + M_W^2 p_{ze})$$

$$\gamma = -(\frac{M_W^2}{2} + p_{x\nu}p_{xe} + p_{y\nu}p_{ye})^2 + E_e^2 p_{T\nu}^2$$

Unfortunately the eq. 1.7 gives rise to a twofold ambiguity corresponding to the two possible solutions of eq. 1.8 for p_z^ν. Once the ambiguity is resolved, in the approximation that the W has width equal to zero ($M_W = 80.385 \pm 0.015$ GeV) the W rapidity can then be calculated as shown in eq. 1.4 taking into account that

$$p_{zW} = p_{ze} + p_{z\nu}. \tag{1.9}$$

The transverse momentum of the W boson is computed as:

$$\overrightarrow{p_{TW}} = \overrightarrow{p_{Te}} + \overrightarrow{p_T^{miss}}. \tag{1.10}$$

1.2.5 Overview of Past W Cross-section Measurements

The W boson was discovered by the UA1 and UA2 experiments at $Sp\bar{p}S$. Its production cross-section has been measured in previous experiments such as UA1 [21] and UA2 [22], CDF [23, 24] and D0 [25] at Fermilab at two different centre of mass energies The PHENIX experiment at the RHIC collider has also measured the W cross-section in pp collisions at $\sqrt{s} = 0.5$ TeV [26]. Fig. 1.9 shows the measured W cross-section for a number of experiments as well as the expected cross-sections as a function of the centre of mass energy. The ATLAS experiment has published the measurement of the W cross-section using the data collected in 2010.

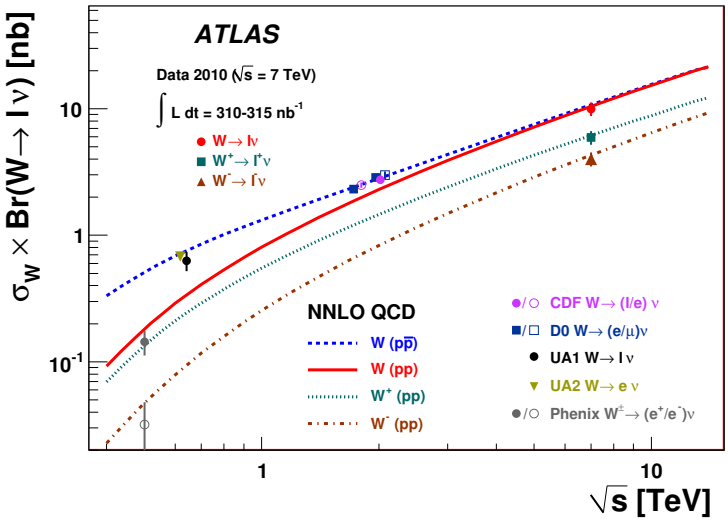

Figure 1.9: Measured values of W cross-sections at TeVatron, $Sp\bar{p}S$, RHIC and ATLAS experiments compared to the NNLO prediction as a function of the centre of mass energy [27].

In $p\bar{p}$ collisions the production cross-section is the same for both W^+ and W^- while as explained in Section 1.2.3 at pp colliders, the W^+ production cross-section is higher than the W^-

one.

1.2.6 Overview of Past W Asymmetry Measurements

In $p\bar{p}$ collisions since the contribution from the u quarks in the proton is enhanced compared to the d one, the W^+ ($u\bar{d}$ combination) is more likely to move in the direction of the proton. For the same reason W^- ($d\bar{u}$ combination) is more likely to move in the same direction as the $\bar{p}$. This effect produces a charge asymmetry (see Fig. 1.10) in the W rapidity distribution.

In pp collisions an overall charge asymmetry in the W production and a rapidity dependent asymmetry exists. The charge asymmetry is defined as:

$$A = \frac{\sigma_{W^+} - \sigma_{W^-}}{\sigma_{W^+} + \sigma_{W^-}}.$$

The overall charge asymmetry as well as the charge asymmetry as a function of y (Fig. 1.8) can be used to constrain the PDFs because they are related to the momentum distribution of u and d quarks in the proton. At LO where the dominant W^+ and W^- production mechanism is $u\bar{d}$ and $d\bar{u}$ respectively, the asymmetry can be expressed as:

$$A_W(y) \approx \frac{u(x_1)\bar{d}(x_2) - d(x_1)\bar{u}(x_2)}{u(x_1)\bar{d}(x_2) + d(x_1)\bar{u}(x_2)}. \tag{1.11}$$

For small x values, the contribution of sea quarks is $\bar{u} \sim \bar{d} \sim \bar{q}$ and the above expression can be simplified to:

$$A_W(y) \approx \frac{u-d}{u+d} \approx \frac{u_v - d_v}{u_v + d_v + 2\bar{q}} \tag{1.12}$$

which indicates that the asymmetry is sensitive to the valence quarks PDFs. The advantage of using the asymmetry rather than the W^+ and W^- cross-sections in PDF fits is that in the ratio some of the uncertainties cancel out.

The W charge asymmetry as function of the W rapidity y is defined as:

$$A_W(y) = \frac{\frac{d\sigma_{W^+}}{dy} - \frac{d\sigma_{W^-}}{dy}}{\frac{d\sigma_{W^+}}{dy} + \frac{d\sigma_{W^-}}{dy}}. \tag{1.13}$$

For the reasons explained earlier, it is usually the lepton asymmetry rather than the direct W asymmetry that is used. The lepton asymmetry is defined as $A_l(\eta) = \frac{d\sigma_{W^+}/d\eta - d\sigma_{W^-}/d\eta}{d\sigma_{W^+}/d\eta + d\sigma_{W^-}/d\eta}$ where η is the pseudorapidity of the charged lepton, an approximation of the rapidity when $m \ll E$. Fig. 1.10 shows the W and lepton rapidity distributions in $p\bar{p}$ and pp collisions.

The lepton asymmetry is a convolution of the W production charge asymmetry and the well known asymmetry from the $V-A$ W decay. Since the $V-A$ asymmetry is well understood (see Section 1.2.4) the lepton asymmetry is equally sensitive to the parton distribution. In practice,

higher order QCD effects introduce a dependence of the charged lepton decay angle and as a consequence of the lepton asymmetry on the W polarisation.

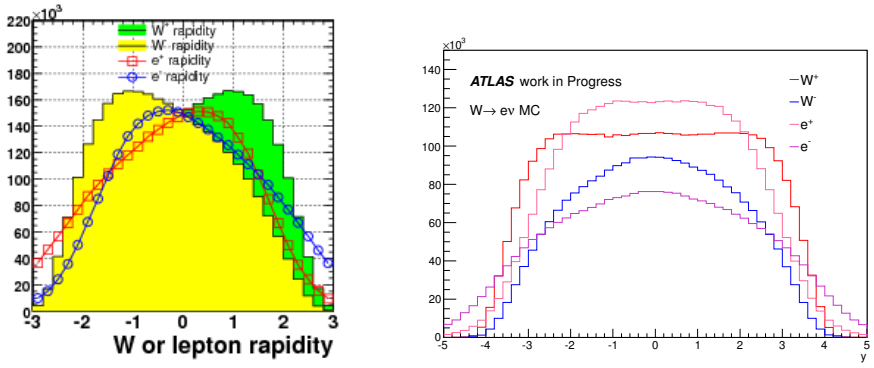

Figure 1.10: Rapidity distributions of W^+, W^- and the decay leptons for: *Left* $p\bar{p}$ collisions [33] and *Right* pp collisions without applying any kinematic requirements.

The forward-backward charge asymmetry due to the preferred direction of W^+ and W^- has been measured by both the CDF [28, 29] and the D0 [30, 31] collaborations and the data have been included in global PDF fits. The D0 charge asymmetry results were given as a function of the pseudorapidity of the lepton for two different p_T bins (Fig. 1.11). The results show some discrepancy compared to the prediction at large lepton p_T which has also been confirmed by CDF. This was acsribed to the fact that the PDFs used were based on measurements done previously.

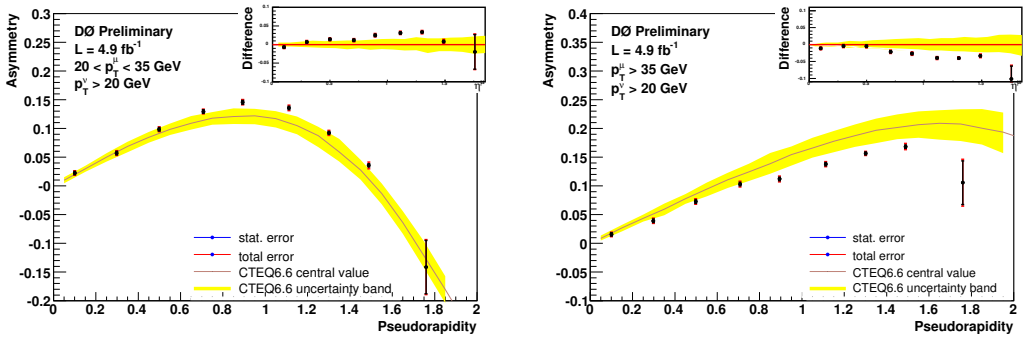

Figure 1.11: $D0$ muon charge asymmetry as a function of the muon pseudorapidity for two p_T ranges $20 < p_T^\mu < 35$ GeV and $p_T^\mu > 35$ GeV compared to the theoretical prediction of CTEQ6.6. The top right windows show the difference between the muon charge asymmetry and the central value of CTEQ6.6. The yellow band represents the uncertainty of the CTEQ6.6 prediction [32].

The CDF collaboration has performed a direct charge asymmetry measurement where the W rapidity is estimated using kinematic constraints and an iterative weighting procedure based on the angular distribution of the decay. The results displayed in Fig. 1.12 show a good agreement between the data and the theory prediction.

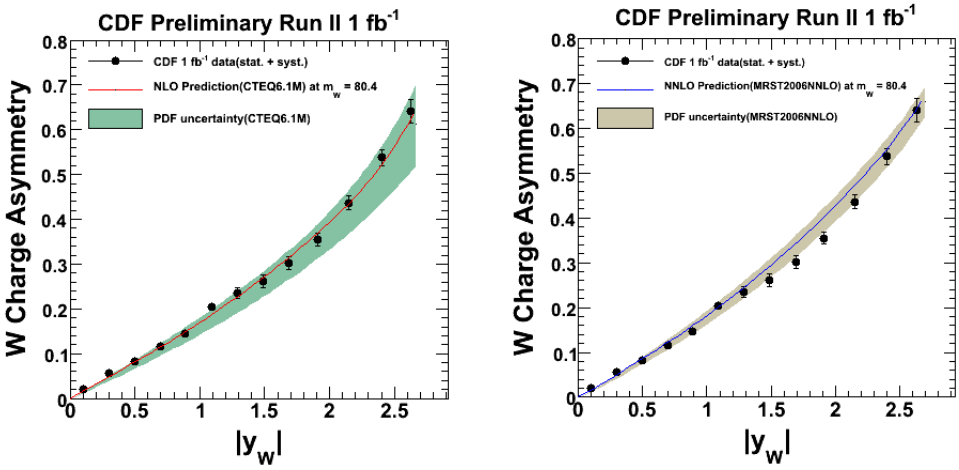

Figure 1.12: CDF W charge asymmetry as a function of the W rapidity compared to the NLO and NNLO theory predictions [33].

The asymmetry measurements performed at LHC with the 2010 data sample will be briefly presented in Section 6.3.

Chapter 2

The ATLAS detector

ATLAS (**A** **T**oroidal **L**HC **A**pparatu**S**) is one of the main experiments of the Large Hadron Collider situated at CERN, Geneva. It is a general purpose detector optimised for discovering the Standard Model Higgs boson but also able to investigate New Physics phenomena and to provide high precision measurements in the QCD and electroweak sector.

The ATLAS detector, shown in Figure 2.1, comprises tracking devices, calorimeters and a muon spectrometer.

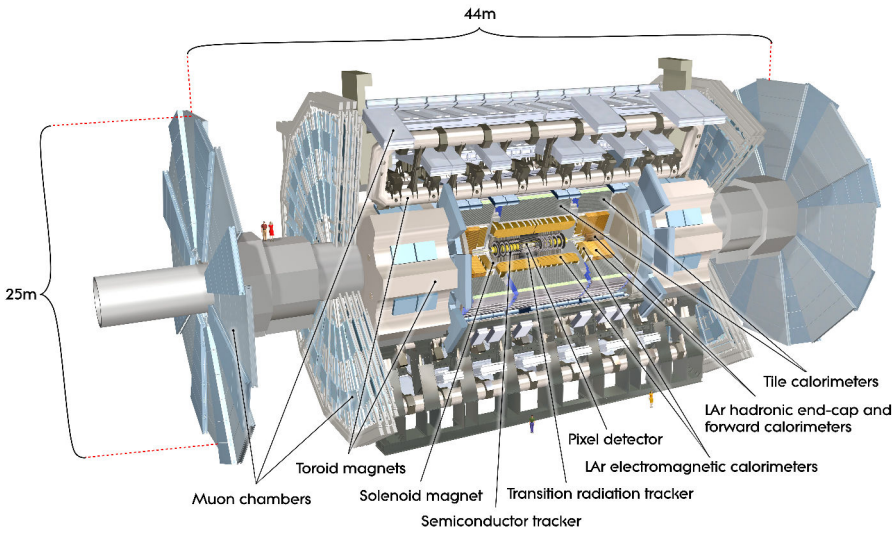

Figure 2.1: Cut-away view of the ATLAS detector. The dimensions of the detector are 25 m in height and 44 m in length. The overall weight of the detector is approximately 7000 tonnes [34].

Detector Component	Required resolution	η coverage	
		Measurement	Trigger
Tracking	$\sigma_{p_T}/p_T = 0.05\% p_T \otimes 1\%$	± 2.5	
Electromagnetic calorimetry	$\sigma_E/E = 10\%/\sqrt{E} \otimes 0.7\%$	± 3.2	± 2.5
Hadronic calorimetry (jets)			
- barrel and end-cap	$\sigma_E/E = 50\%/\sqrt{E} \otimes 3\%$	± 3.2	± 3.2
- forward	$\sigma_E/E = 100\%/\sqrt{E} \otimes 10\%$	$3.1 < \lvert\eta\rvert < 4.9$	$3.1 < \lvert\eta\rvert < 4.9$
Muon spectrometer	$\sigma_{p_T}/p_T = 10\%$ at $p_T = 1$TeV	± 2.7	± 2.4

Table 2.1: Design performance of the ATLAS detector. Note that, high-p_T muons can be measured independently in the muon spectrometer and in the tracking system. The units for E and p_T are in GeV [34].

2.1 Detector Overview

The coordinate system used to describe the ATLAS detector and the particles emerging from the p-p collisions are briefly summarised here. The nominal interaction point is defined as the origin of a right-handed coordinate system, while the beam direction defines the z-axis and the $x-y$ plane is transverse to the beam direction. The positive x-axis is defined as pointing from the interaction point to the centre of the LHC ring and the positive y-axis is defined as pointing upwards. The side-A of the detector is defined as that with positive z and the side-C is that with negative z. Some of the basic variables used widely within the ATLAS experiment are listed below.

- The azimuthal angle φ is measured around the beam axis.
- The polar angle θ is the angle with respect to the beam axis.
- The transverse momentum p_T of a particle is the projection of its momentum p onto the $x-y$ plane.
- The missing transverse momentum in an event is defined as $\overrightarrow{p_T^{miss}} = -\sum_{i=1}^{N} \overrightarrow{p_{T_i}}$ where N indicates the number of final state particles of the event. The transverse quantities p_T and $|\overrightarrow{p_T^{miss}}|$ are invariant under the Lorentz transformations along the z-axis.
- The transverse energy E_T for a given particle is given by the relation $E_T = E \sin\theta$ where E is the particle energy. The missing transverse energy is also used ($E_T^{miss} = |\overrightarrow{p_T^{miss}}|$).
- The rapidity y of a particle is defined as $y = \frac{1}{2} \ln \frac{E + p_z}{E - p_z}$ where p_z is the particle momentum along the z-axis. For particles of small mass with respect to their energy ($m \ll E$) the rapidity can be approximated by the pseudorapidity $\eta = -\ln\tan(\theta/2)$. The calculation of η has the advantage that doesn't require the identification of the particle.

- The distance ΔR between two particles a, b is defined in the pseudorapidity-azimuthal plane as $\Delta R = \sqrt{\Delta\eta^2 + \Delta\varphi^2}$ where $\Delta\eta$ is the distance $|\eta_a - \eta_b|$, $\Delta\varphi = |\varphi_a - \varphi_b|$ and η and φ are the azimuthal and polar angle of the particle tracks.

The general requirements for a general purpose LHC detector dictated by the vast area of possible physics analyses are [34]:

- fast, radiation-hard electronics and sensor elements as well as high detector granularity in order to handle the particle fluxes and to reduce the influence of overlapping events,
- large acceptance in pseudorapidity η with almost full azimuthal angle coverage φ,
- good charged-particle momentum resolution and reconstruction efficiency in the inner tracker including vertex detectors close to the interaction region for tagging of τ-leptons and b-jets and detection of secondary vertices,
- very good electromagnetic calorimetry for electron and photon identification and measurements, complemented by full-coverage hadronic calorimetry for accurate jet and missing transverse energy measurements,
- good muon identification and momentum resolution over a wide range of momenta with the ability to determine unambiguously the charge of high p_T muons and
- highly efficient triggering low transverse-momentum objects with sufficient background rejection.

In the following sections, the different components of the ATLAS detector are briefly described with particular attention to the Liquid Argon calorimeters since the author of this thesis has worked on those specific sub-detectors.

2.2 Inner Detector

The ATLAS Inner Detector (ID) — shown in Figures 2.2 and 2.3 — is designed to provide excellent momentum resolution as well as primary and secondary vertex position measurements within the pseudorapidity range $|\eta| < 2.5$ as well as electron identification within $|\eta| < 2.0$. It consists of three independent but complementary detectors: the Pixel Detector, the Semi-Conductor Tracker (SCT) and the Transition Radiation Tracker (TRT). An important requirement for the construction of the ID was that the sub-systems need to be able to withstand large integrated irradiation.

The **Pixel Detector** is the closest detector to the beam pipe thus allowing to measure tracks in the region very close to the interaction point. It consists of three cylindrical layers in the barrel region and three disk layers in the end-caps. There is a total of 1744 silicon sensors each with

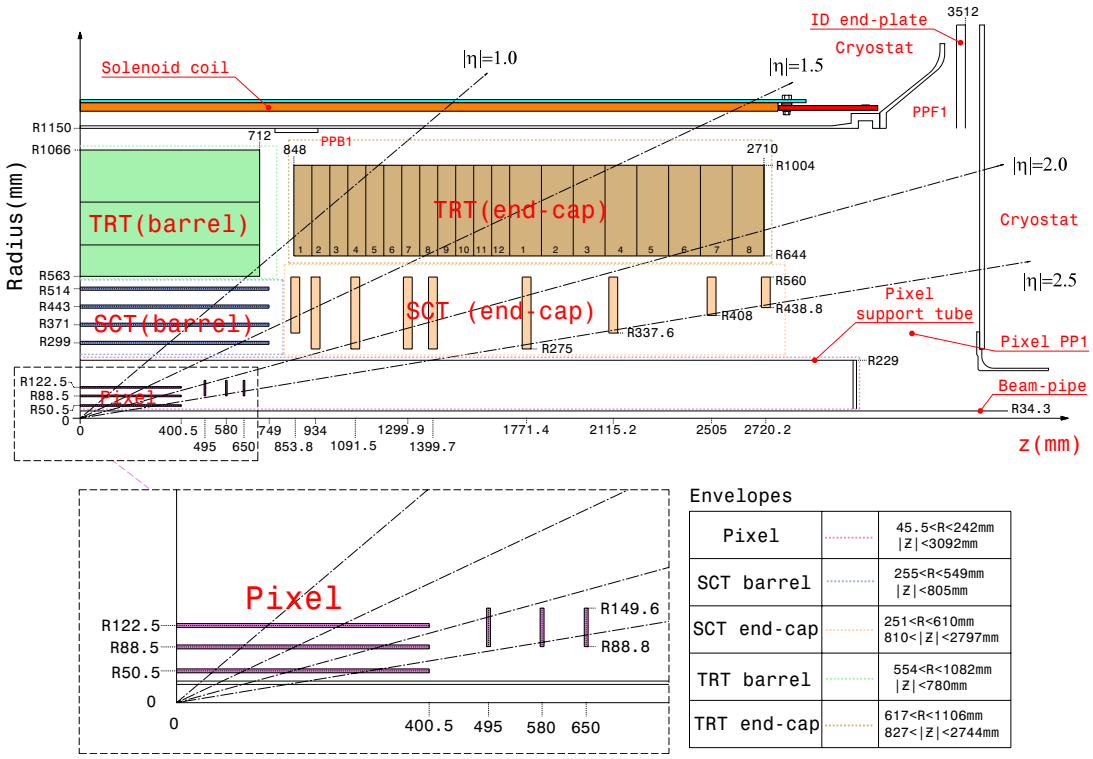

Figure 2.2: Two-dimensional view of a quarter-section of the ATLAS inner detector showing each of the major detector elements with the dimensions of the active regions and envelopes. The region very close to the interaction point is shown enlarged at the bottom of the picture [34].

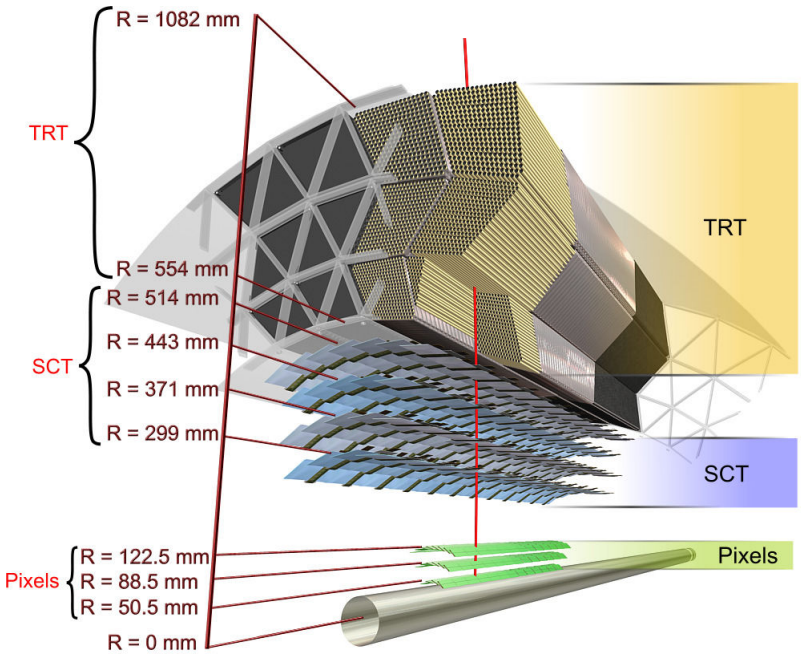

Figure 2.3: Drawing showing the sensors and structural elements crossed by a charged track in the barrel ID [34].

46080 readout channels. The nominal pixel size is 50×400 μm^2. The intrinsic spatial resolution of the barrel detector is 10 μm in $(R-\varphi)$ and 115 μm in (z) [34].

The **SCT** is a silicon micro-strip detector. It consists of four double layers in the barrel region giving four space-points and nine disk layers in the end-caps for a total number of readout channels of ≈ 6 million. For each set of two layers, one is parallel to the beam axis to measure $R-\varphi$ and the other layer is set at an angle of 40 mrad to measure the z coordinate. The intrinsic spatial resolution in the barrel region is 17μm in $(R-\varphi)$ and 580 μm in (z) [35].

The **TRT** consists of layers of 4 mm straw tubes with a gas mixture of 70% Xe, 27% CO_2 and 3% O_2. It covers the pseudorapidity range $|\eta| < 2.0$ and has an intrinsic resolution of 130 μm in $(R-\varphi)$.

The reconstruction of the tracks in the ID is affected by the following issues [34]:

- many electrons lose most of their energy through bremsstrahlung before reaching the electromagnetic calorimeter,
- a significant percentage of photons convert before reaching the electromagnetic calorimeter (Figure 2.4 shows the material distribution at the end of the ID) and
- a good fraction of charged pions will undergo inelastic hadronic interactions inside the ID.

In Table 2.2 the geometrical characteristics of the inner detector system are summarised.

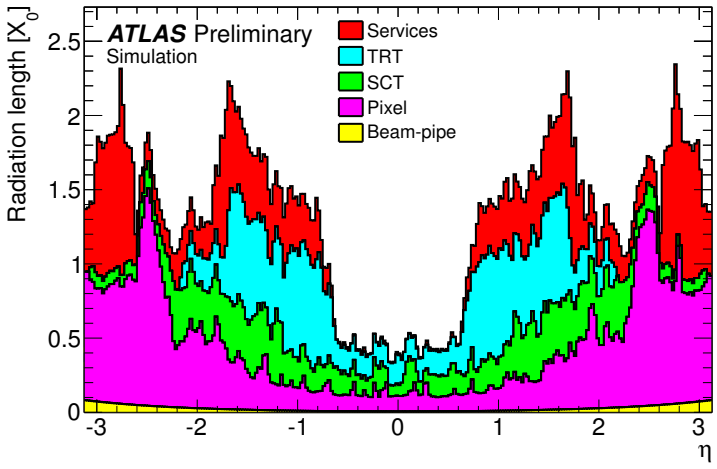

Figure 2.4: Material distribution (X_0) at the exit of the ID envelope, including the services and thermal enclosures. The distribution is shown as a function of $|\eta|$ and averaged over φ. The breakdown indicates the contributions of external services and of individual sub-detectors, including services in their active volume [36].

Item		Radial extension (mm)	Length (mm)
Overall ID envelope		$0 < R < 1150$	$0 < \|z\| < 3512$
Beam-pipe		$29 < R < 36$	
Pixel	Overall envelope	$45.5 < R < 242$	$0 < \|z\| < 3092$
3 cylindrical	layers Sensitive barrel	$50.5 < R < 122.5$	$0 < \|z\| < 400.5$
3 disks	Sensitive end-cap	$88.8 < R < 149.6$	$495 < \|z\| < 650$
SCT	Overall envelope	$255 < R < 549$ (barrel)	$0 < \|z\| < 805$
		$251 < R < 610$ (end-cap)	$810 < \|z\| < 2797$
4 cylindrical layers	Sensitive barrel	$299 < R < 514$	$0 < \|z\| < 749$
2×9 disks	Sensitive end-cap	$275 < R < 560$	$839 < \|z\| < 2735$
TRT	Overall envelope	$554 < R < 1082$ (barrel)	$0 < \|z\| < 780$
		$617 < R < 1106$ (end-cap)	$827 < \|z\| < 2744$
73 straw planes	Sensitive barrel	$563 < R < 1066$	$0 < \|z\| < 712$
160 straw planes	Sensitive end-cap	$644 < R < 1004$	$848 < \|z\| < 2710$

Table 2.2: Main geometrical parameters of the inner-detector system [34].

2.3 Calorimetry

The ATLAS calorimeters, shown in Figure 2.5, cover a pseudorapidity range $|\eta| < 4.9$. They provide electron, photon, jet energy and E_T^{miss} measurements. The electromagnetic (EM) calorimeter with its fine granularity is suited for precision measurements of electron and photon energy (see Table 2.1). It has a total thickness of ~ 22 radiation lengths (X_0) in the barrel and ~ 24 X_0 in the end-cap region allowing to contain the electromagnetic shower for a wide energy range of electrons and photons.

The approximately ten interaction lengths (λ) of EM and hadronic calorimeter in the barrel and in the end-cap region are suitable to provide good energy resolution for high energy jets (see Table 2.1). The total thickness (which is $\sim 9\lambda$ at $\eta = 0$ with the addition of the outer support) reduces punch-through well below the level of prompt or decay muons. Together with the large η-coverage, this thickness will also ensure a good E_T^{miss} measurement.

2.3.1 LAr Electromagnetic Calorimeter

The EM calorimeter is divided into a barrel part ($|\eta| < 1.475$) and two end-cap components ($1.375 < |\eta| < 3.2$) each housed in their own cryostat. The LAr EM calorimeters share a common vacuum vessel with the central solenoid thus eliminating two vacuum walls. The EM barrel calorimeter consists of two identical half-barrels separated by a small gap (4 mm) at $z = 0$. Each

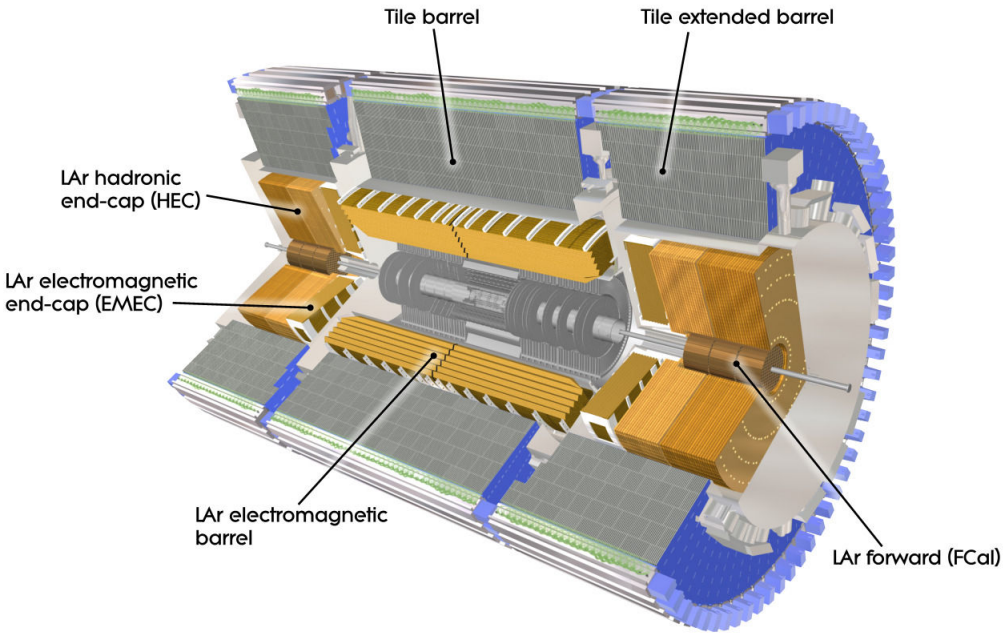

Figure 2.5: Cut-away view of the ATLAS calorimeter system [34].

end-cap is mechanically divided into two coaxial wheels: an outer wheel covering the region $1.375 < |\eta| < 2.5$ and an inner wheel covering the region $2.5 < |\eta| < 3.2$.

The EM calorimeter is a lead-LAr detector with accordion shaped kapton-copper electrodes and lead absorber plates. The accordion geometry provides complete coverage in φ without azimuthal uninstrumented regions and a fast extraction of the signal at the back or at the front of the electrodes. In the barrel the accordion waves run along R and the folding angles of the waves vary with the radius to keep the liquid-argon gap constant. In the end-caps, the waves run along z and the liquid-argon gap increases with radius. The accordion geometry leads to a very uniform response in terms of linearity and resolution as a function of φ.

In the region $|\eta| < 2.5$ the EM calorimeter is segmented into three longitudinal sections as shown in Figure 2.6. The first layer (strips) has a very fine granularity in η mainly for $\pi^0 - \gamma$ separation, the second layer (middle) is where most of the energy of the electrons and photons is deposited and the third layer (back) measures the energy of the tail of the shower. In the region $|\eta| < 1.8$, a shower detector (presampler) is used to correct for the energy lost upstream of the calorimeter. The presampler consists of an active LAr layer of thickness 1.1 cm (0.5 cm) in the barrel (end-cap) region. In the range $2.5 < |\eta| < 3.2$ the EM calorimeter (inner wheel) is segmented into two layers and has a coarser granularity. The granularity of the different layers of the EM calorimeter is shown in Table 2.3.

The EM calorimeter and its electronics will be described in Chapter 3 in more detail.

EM Calorimeter				
	Barrel		**End-cap**	
Number of layers and $\|\eta\|$ coverage				
Presampler	1	$\|\eta\| < 1.52$	1	$1.5 < \|\eta\| < 1.8$
Calorimeter	3	$\|\eta\| < 1.35$	2	$1.375 < \|\eta\| < 1.5$
	2	$1.35 < \|\eta\| < 1.475$	3	$1.5 < \|\eta\| < 2.5$
			2	$2.5 < \|\eta\| < 3.2$
Granularity $\Delta\eta \times \Delta\varphi$ versus $\|\eta\|$				
Presampler	0.025×0.1	$\|\eta\| < 1.52$	0.025×0.1	$1.5 < \|\eta\| < 1.8$
Calorimeter 1st layer	$0.025/8 \times 0.1$	$\|\eta\| < 1.40$	0.050×0.1	$1.375 < \|\eta\| < 1.425$
	0.025×0.025	$1.40 < \|\eta\| < 1.475$	0.025×0.1	$1.425 < \|\eta\| < 1.5$
			$0.025/8 \times 0.1$	$1.5 < \|\eta\| < 1.8$
			$0.025/6 \times 0.1$	$1.8 < \|\eta\| < 2.0$
			$0.025/4 \times 0.1$	$2.0 < \|\eta\| < 2.4$
			0.025×0.1	$2.4 < \|\eta\| < 2.5$
			0.1×0.1	$2.5 < \|\eta\| < 3.2$
Calorimeter 2nd layer	0.025×0.025	$\|\eta\| < 1.40$	0.050×0.025	$1.375 < \|\eta\| < 1.425$
	0.075×0.025	$1.40 < \|\eta\| < 1.475$	0.025×0.025	$1.425 < \|\eta\| < 2.5$
			0.1×0.1	$2.5 < \|\eta\| < 3.2$
Calorimeter 3rd layer	0.050×0.025	$\|\eta\| < 1.35$	0.050×0.025	$1.5 < \|\eta\| < 2.5$
Number of readout channels				
Presampler	7808		1536 (both sides)	
Calorimeter	101760		62208 (both sides)	

Table 2.3: Main parameters of the EM calorimeter system [34].

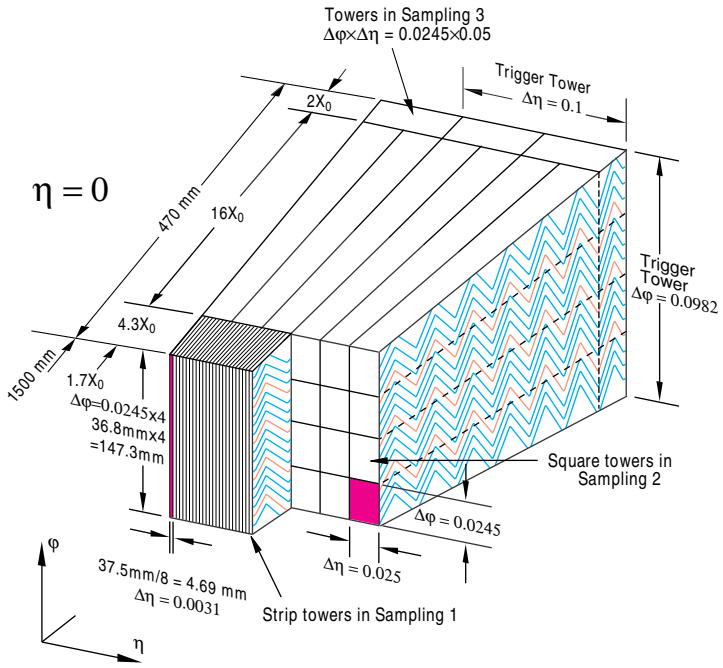

Figure 2.6: Sketch of a part of the barrel module where the different layers are clearly visible with the ganging of electrodes in φ. The granularity in η and φ of the cells of each of the three layers and of the trigger towers is also shown [37].

2.3.2 Hadronic Calorimeter

Tile Calorimeter

The tile calorimeter (Figure 2.7) is a sampling calorimeter that uses steel as absorber and scintillating tiles as active medium. It is placed after the liquid argon EM calorimeter covering the region $|\eta| < 1.7$ and is divided into a central and two extended barrels. The barrel part covers the region $|\eta| < 1.0$ and the two extended barrel components the range $0.8 < |\eta| < 1.7$. The barrel and extended barrels are divided azimuthally into 64 modules. Radially, the tile calorimeter extends from an inner radius of 2.28 m to an outer radius of 4.25 m. It is longitudinally segmented in three layers approximately 1.5, 4.1 and 1.8 λ thick for the barrel and 1.5, 2.6, and 3.3 λ for the extended barrel. Two sides of the scintillating tiles are read out by wavelength shifting fibres into two separate photomultiplier tubes. In η, the readout cells built by grouping fibres into the photomultipliers are pseudo-projective towards the interaction region [34].

LAr Hadronic End-Cap Calorimeter

The Hadronic End-cap Calorimeter (HEC), shown in Figure 2.8, consists of two independent wheels per end-cap: a front wheel (HEC1) and a rear wheel (HEC2) located directly behind the end-cap EM calorimeter and sharing the same LAr cryostats. To reduce the drop in material

LAr Hadronic End-cap			
$\|\eta\|$ coverage		$1.5 < \|\eta\| < 3.2$	
Number of layers		4	
Granularity $\Delta\eta \times \Delta\varphi$		0.1×0.1	$1.5 < \|\eta\| < 2.5$
		0.2×0.2	$2.5 < \|\eta\| < 3.2$
Readout Channels		5632 (both sides)	
LAr Forward Calorimeter			
$\|\eta\|$ coverage		$3.1 < \|\eta\| < 4.9$	
Number of layers		3	
Granularity $\Delta x \times \Delta y$		FCall: 3.0×2.6	$3.15 < \|\eta\| < 4.30$
		FCall: ∼four times finer	$3.10 < \|\eta\| < 3.15$,
			$4.30 < \|\eta\| < 4.83$
		FCall: 3.3×4.2	$3.24 < \|\eta\| < 4.50$
		FCall: ∼four times finer	$3.20 < \|\eta\| < 3.24$,
			$4.50 < \|\eta\| < 4.81$
		FCall: 5.4×4.7	$3.32 < \|\eta\| < 4.60$
		FCall: ∼four times finer	$3.29 < \|\eta\| < 3.32$,
			$4.60 < \|\eta\| < 4.75$
Readout Channels		3524 (both sides)	
Scintillator Tile Calorimeter			
	Barrel	**Extended Barrel**	
$\|\eta\|$ coverage	$\|\eta\| < 1.0$	$0.8 < \|\eta\| < 1.7$	
Number of layers	3	3	
Granularity $\Delta\eta \times \Delta\varphi$	0.1×0.1	0.1×0.1	
Last layer	0.2×0.1	0.2×0.1	
Readout Channels	5760	4092 (both sides)	

Table 2.4: Main parameters of Hadronic and Forward Calorimeter [34].

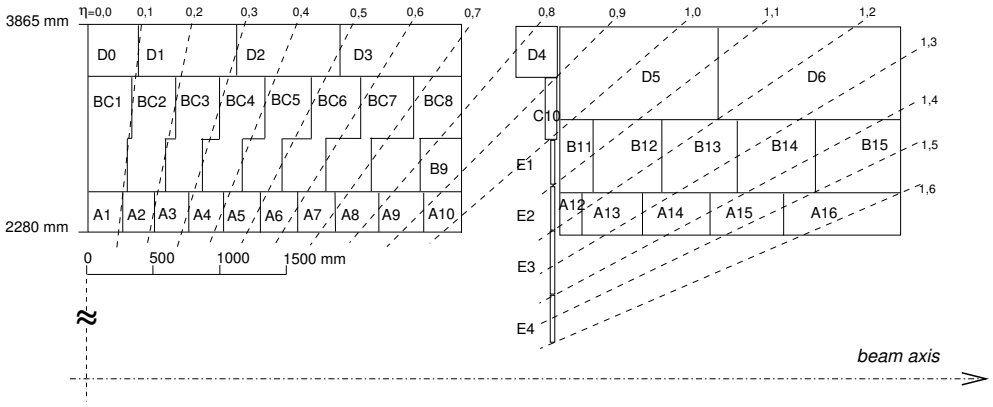

Figure 2.7: Segmentation in depth and η of the tile-calorimeter modules in the central (left) and extended (right) barrels. The bottom of the picture corresponds to the inner radius of the tile calorimeter. The tile calorimeter is symmetric with respect to the interaction point [34].

density at the transition between the HEC and the Forward Calorimeter (around $|\eta| = 3.1$), the HEC extends out to $|\eta| = 3.2$, thereby overlapping with the Forward Calorimeter. Similarly, the HEC η range slightly overlaps with the η of the tile calorimeter ($|\eta| < 1.7$) by extending to $|\eta| = 1.5$. Each wheel is divided into two segments in depth thus making a total of four layers per end-cap. The wheels closest to the interaction point are built from 25 mm parallel absorber copper plates, while those further away use 50 mm absorber copper plates (for all wheels the first plate is half-thickness). The inner radius of the wheel is 0.475 m (except in the overlap region with the forward calorimeter where the radius is 0.372 m) and the outer radius is 2.03 m. The copper plates are interleaved with 8.5 mm LAr gaps, providing the active medium for this sampling calorimeter.

LAr Forward Calorimeter

The Forward Calorimeters (FCal) are located in the same cryostats as the end-cap calorimeters and provide coverage over the region $3.1 < |\eta| < 4.9$ (see Figure 2.9). The FCal is approximately 10 λ deep, and consists of three modules in each end-cap: the first (FCal1) uses copper and is optimised for electromagnetic measurements, while the other two (FCal2, FCal3) use tungsten and measure predominantly the energy of hadronic interactions. The close vicinity and coupling between these systems result in a quite hermetic design, which minimises energy losses in cracks between the calorimeter systems and also limits the backgrounds which reach the muon system.

2.4 Muon Spectrometer

The Muon Spectrometer (Figure 2.10) is designed to detect charged particles exiting the barrel and end-cap calorimeters and to measure their momentum in the pseudorapidity range $|\eta| < 2.7$. It is based on the magnetic bending of muon tracks in the large superconducting air-core toroidal

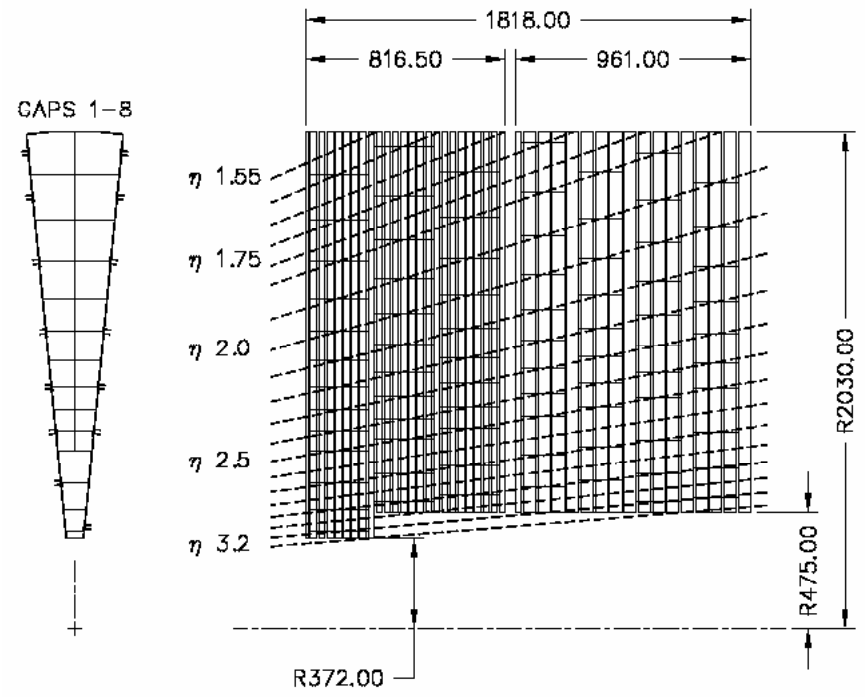

Figure 2.8: Schematic $R-\varphi$ (left) and $R-z$ (right) views of a part of the Hadronic End-Cap calorimeter. The semi-pointing layout of the readout cells is indicated by the dashed lines. Dimensions are in *mm* [34].

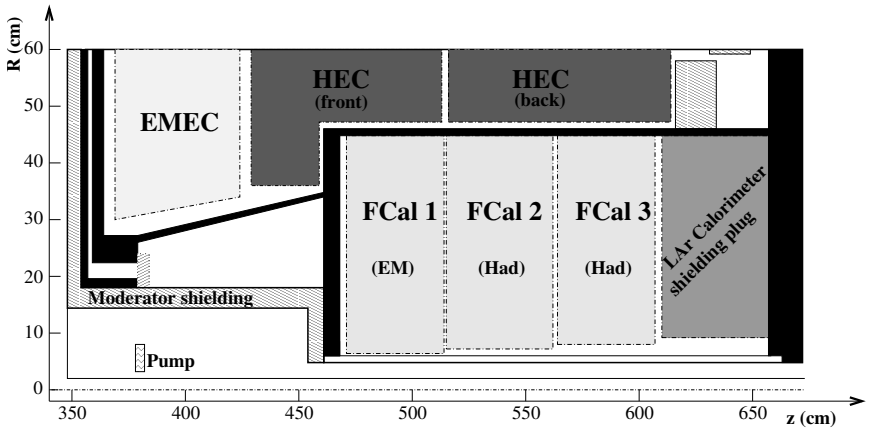

Figure 2.9: Schematic diagram showing the three FCal modules located in the end-cap cryostat. The material in front of the FCal and the shielding plug behind it are also shown. The black regions are structural parts of the cryostat. The diagram has a larger vertical scale for clarity [34].

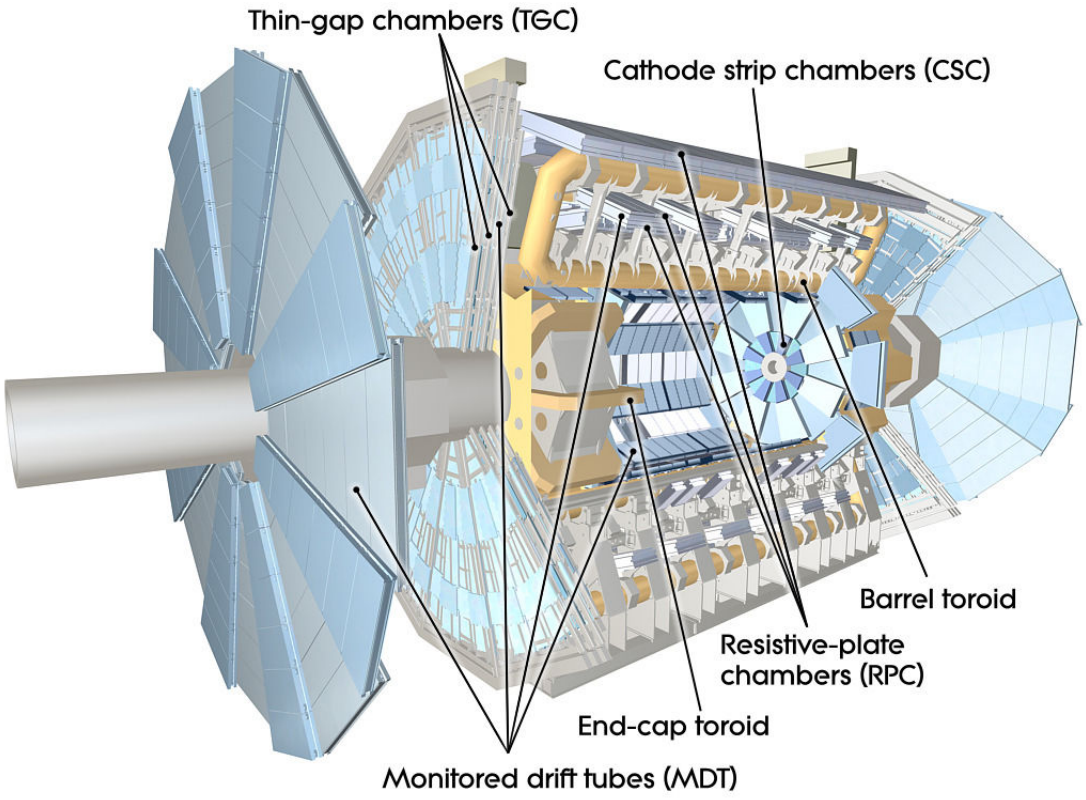

Figure 2.10: Cut-away view of the ATLAS muon system [34].

Monitored drift tubes	**MDT**
- Coverage	$\|\eta\| < 2.7$ (innermost layer: $\|\eta\| < 2.0$)
- Number of chambers	1088 (1150)
- Number of channels	339 000 (354 000)
- Function	Precision tracking
Cathode strip chambers	**CSC**
- Coverage	$2.0 < \|\eta\| < 2.7$
- Number of chambers	32
- Number of channels	31 000
- Function	Precision tracking
Resistive plate chambers	**RPC**
- Coverage	$\|\eta\| < 1.05$
- Number of chambers	544 (606)
- Number of channels	359 000 (373 000)
- Function	Triggering, second coordinate
Thin gap chambers	**TGC**
- Coverage	$1.05 < \|\eta\| < 2.7$ (2.4 for triggering)
- Number of chambers	3588
- Number of channels	318 000
- Function	Triggering, second coordinate

Table 2.5: Main parameters of the muon spectrometer. Numbers in brackets for the MDT's and the RPC's refer to the final configuration of the detector in 2009 [34].

magnets, instrumented with separate trigger and high-precision tracking chambers. Over the range $|\eta| < 1.4$, magnetic bending is provided by the large barrel toroid while for $1.6 < |\eta| < 2.7$, muon tracks are bent by the two end-cap magnets. Over $1.4 < |\eta| < 1.6$, usually referred to as the transition region, magnetic deflection is provided by a combination of barrel and end-cap fields. This magnet configuration provides a field which is mostly orthogonal to the muon trajectories, while reducing the degradation of resolution due to multiple scattering. The main parameters of the muon chambers are listed in Table 2.5.

In the barrel region, tracks are measured in chambers arranged in three cylindrical layers around the beam axis while in the transition and end-cap regions, the chambers are installed in planes perpendicular to the beam in three layers.

Over most of the η-range, a precision measurement of the track coordinates and the momentum is provided by Monitored Drift Tubes (MDT's). At large pseudorapidities ($2 < |\eta| < 2.7$), multiwire proportional chambers are used. They are called Cathode Strip Chambers (CSCs) and have cathodes segmented into strips with higher granularity, to withstand the demanding rate and background conditions. The stringent requirements on the relative alignment of the muon cham-

ber layers are met by the combination of precision mechanical-assembly techniques and optical alignment systems both within and between muon chambers.

The trigger part of the muon system covers the pseudorapidity range $|\eta| < 2.4$. Resistive Plate Chambers (RPC's) are used in the barrel and Thin Gap Chambers (TGC's) in the end-cap regions. The trigger chambers for the muon spectrometer serve a threefold purpose: provide bunch-crossing identification, provide well-defined p_T thresholds, and measure the muon coordinate in the direction orthogonal to that determined by the precision-tracking chambers [34].

2.5 Magnet System

ATLAS features a unique hybrid system of four large superconducting magnets producing a solenoidal and toroidal fields.

The solenoid is aligned on the beam axis and provides a 2 T axial magnetic field in the inner detector region, while minimising the thickness in front of the barrel electromagnetic calorimeter. To achieve the desired calorimeter performance, the layout was carefully optimised to keep the material thickness in front of the calorimeter as low as possible, resulting in a solenoid assembly contributing a total of ~ 0.66 radiation lengths.

A barrel toroid and two end-cap toroids (see Figure 2.11) produce a toroidal magnetic field of approximately 0.5 T and 1 T in the central and end-cap regions of the muon spectrometer respectively. Each of the three toroids consists of eight coils assembled radially and symmetrically around the beam axis. The end-cap toroid coil system is rotated by 22.5° with respect to the barrel toroid coil system in order to provide radial overlap and to optimise the bending power at the interface between the two coil systems [34].

2.6 Trigger

The Trigger and Data Acquisition (TDAQ) systems, the timing- and trigger-control logic, and the Detector Control System (DCS) are partitioned into sub-systems, typically associated with sub-detectors, which have the same logical components and building blocks. The trigger system has three distinct levels: level one (L1), level two (L2) and the event filter (EF). The L2 and EF form the High-Level Trigger (HLT). Each trigger level refines the decisions made at the previous level and, where necessary, applies additional selection criteria. The L1 trigger uses a limited amount of the total detector information to make a decision in less than 2.5μs, reducing the rate to about 75 kHz. The two higher levels (HLT) access more detector information for a final design rate of up to 200 Hz with an event size of approximately 1.3 MByte. Figure 2.12 shows the chain between these three trigger levels. During the 2010 data-taking, the rate of the EF trigger was increased to ~ 300 Hz.

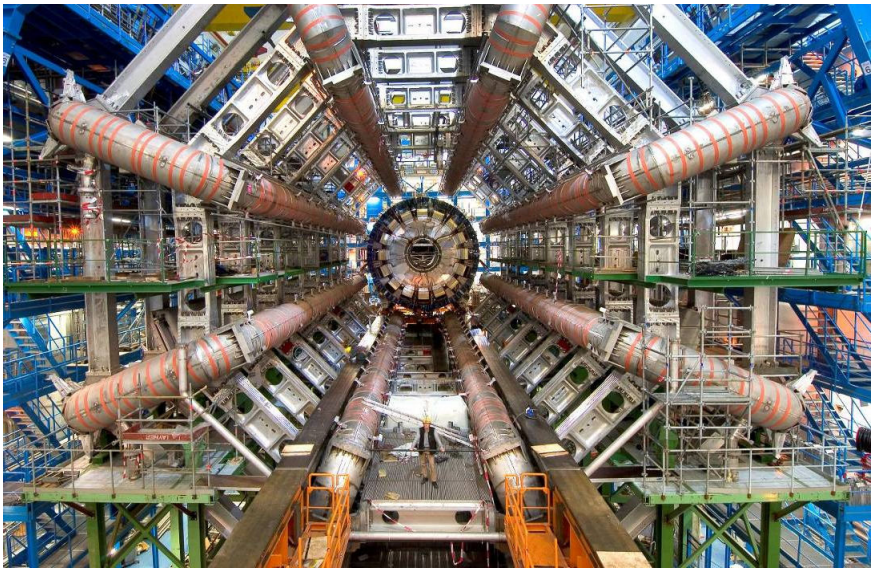

Figure 2.11: Barrel toroid as installed in the underground cavern; note the symmetry of the supporting structure. The temporary scaffolding and green platforms were removed once the installation was complete. The scale is indicated by the person standing in between the two bottom coils. Also visible are the stainless-steel rails carrying the barrel calorimeter with its embedded solenoid, which await translation towards their final position in the centre of the detector [34].

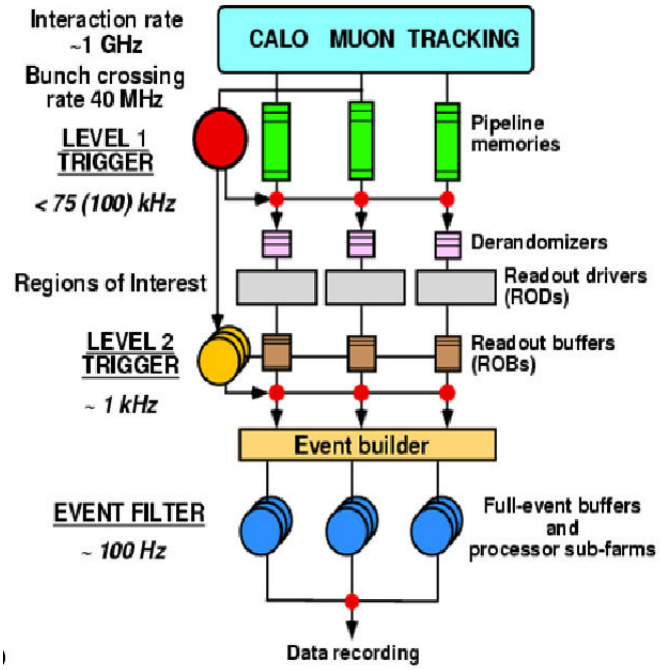

Figure 2.12: Block diagram of the ATLAS trigger. Additional information is used for the HLT in order to reduce the trigger rate.

The L1 trigger searches for high transverse-momentum muons, electrons, photons, jets, and τ-leptons decaying into hadrons, as well as large missing and total transverse energy. Its selection criteria are based on information from a subset of detectors. High transverse-momentum muons are identified using trigger chambers in the barrel and end-cap regions of the muon spectrometer. Calorimeter selections are based on reduced-granularity information from all the calorimeters. Results from the L1 muon and calorimeter triggers are processed by the central trigger processor, which implements a trigger "menu" made up of combinations of trigger selections. Pre-scaling of trigger menu items is also available, allowing optimal use of the bandwidth as luminosity and background conditions change. Events passing the L1 trigger selection are transferred to the next stages of the detector-specific electronics and subsequently to the data acquisition via point-to-point links.

In each event, the L1 trigger also defines one or more regions in η and φ within the detector for which the selection process has identified intersting features (Regions-of-Interest - RoI's). The RoI data include information on the type of feature identified and the criteria passed, e.g. a threshold. This information is subsequently used by the high-level trigger.

The L2 selection is seeded by the RoI information provided by the L1 trigger over a dedicated data path. L2 selections use, at full granularity and precision, all the available detector data within the RoI's (approximately 2% of the total event data). The L2 menus are designed to reduce the trigger rate to approximately 3.5 kHz, with an event processing time of about 40 ms, averaged over all events. The final stage of the event selection is carried out by the event filter, which reduces the event rate to roughly 200 Hz. Its selections are implemented using offline analysis procedures within an average event processing time of the order of 4 s [34].

Chapter 3

Signal Reconstruction in the LAr Calorimeters

In this chapter the work accomplished by the author of this thesis on the **D**igital **S**ignal **P**rocessor (DSP) is presented. The DSP is the part of the back-end electronics of the LAr calorimeters which computes the energy, the time and a quality factor of the signals produced by the particles crossing the detector thus reducing the data flow by a factor of 2. The monitoring of the DSP calculations, the validation and improvement of the DSP code are the contribution of the author of this thesis. These are very crucial tasks to ensure an optimal response of the LAr calorimeters. These detectors play a major role in the $W \to e\nu$ measurements. To introduce the accomplished work, a very brief description of the LAr channel structure and electronics is presented in the first part of this chapter.

To meet the LHC requirements, the LAr electromagnetic (EM) calorimeters have a very good energy resolution, linearity, speed of response and a powerful electron and photon identification. In particular, to ensure a linear response over a wide energy range the EM calorimeter cells electronics cover a dynamic range from 50 MeV to an upper bound of ~ 4 TeV energy deposited in the cell. Here the lower bound corresponds to the typical electronic noise per channel and the upper bound to the maximum energy deposited in a calorimeter cell by electrons produced in decays of Z' and W' bosons with masses of 5-6 TeV. The HEC calorimeter is used for measurements of the energy and angles of jets and the FCal provides a large rapidity coverage ($|\eta| < 4.9$).

3.1 LAr Calorimeter channel structure

In Figure 3.1 the electrode structure of the barrel calorimeter is shown. Every electrode comprises three copper and two kapton layers: the two outer copper layers are connected to the high voltage and the inner copper layer which is connected to the readout electronics, collects the current induced by the ionisation electrons drifting in the liquid argon gap. The electrodes are segmented in pads that define the readout cells. Each cell consists of a lead absorber plate, a liquid argon gap, a

	Rapidity	Lead Thickness	Liquid Argon Thickness
EMB	$\|\eta\| < 0.8$	1.5 mm	2.1 mm
	$0.8 < \|\eta\| < 1.475$	1.1 mm	2.1 mm
EMEC	$1.375 < \|\eta\| < 2.5$	1.7 mm	2.8 - 0.9 mm
	$2.5 < \|\eta\| < 3.2$	2.2 mm	3.1 - 1.8 mm

Table 3.1: Thickness of the LAr gap and the absorber (lead) in the EM calorimeter [37].

readout electrode and a second liquid argon gap. The thickness of the LAr gap and of the absorber plates in the EM calorimeter are shown in Table 3.1.

An electron or a photon hitting the EM calorimeter interacts mainly within the lead absorbers and creates an electromagnetic shower. The charged component of the shower ionises the LAr and the charges produced drift in the electric field created by the high voltage applied on the outer copper layers of the electrode. An electric signal is then induced on the inner copper layer of the electrode. The signals from different longitudinal compartments of the calorimeter are read out at both sides of the electrodes, i.e. at the front and back of the calorimeter where they are received by summing boards and then sent to the Front-end boards (FEBs) [40].

3.2 LAr Calorimeter Readout

3.2.1 LAr calorimeter front-end boards

The general architecture of the LAr readout electronics is shown in Figure 3.2. The analog signal from the mother-boards on the calorimeter is transmitted to the front-end electronics mounted on the front-end boards (FEBs). The FEBs are housed in the front-end crates which are installed on the cryostat feedthroughs. There is a total of 1524 FEBs where the signal is amplified, shaped and digitised.

Each FEB processes up to 128 calorimeter channels. At the exit of the preamplifiers, the signal is split into three overlapping linear gain scales with a ratio of $1/9.3/93$ (low, medium and high gain) and shaped in the form of a bipolar pulse through a $CR-(RC)^2$ analogue filter with a time constant of 15 ns. The (CR) signal differentiation is applied in order to shorten the ionisation pulse, while the two (RC) integrations allow to reduce the pile-up and electronic noise. In Figure 3.3 the pulse of a LAr cell is shown before and after the bipolar shaping.

The shaped signals are then sampled at the LHC bunch-crossing frequency of 40 MHz by four-channel switched-capacitor array (SCA) analogue pipelines that store the signals during the L1 trigger latency ($\sim 2\ \mu$s). For events accepted by the L1 trigger, the signal is read out using the optimal gain and digitised by a 12-bit analog-to-digital converter (ADC) as shown in Figure 3.4. The FEBs also have the task to sum the signal of adjacent calorimeter cells inside each depth layer

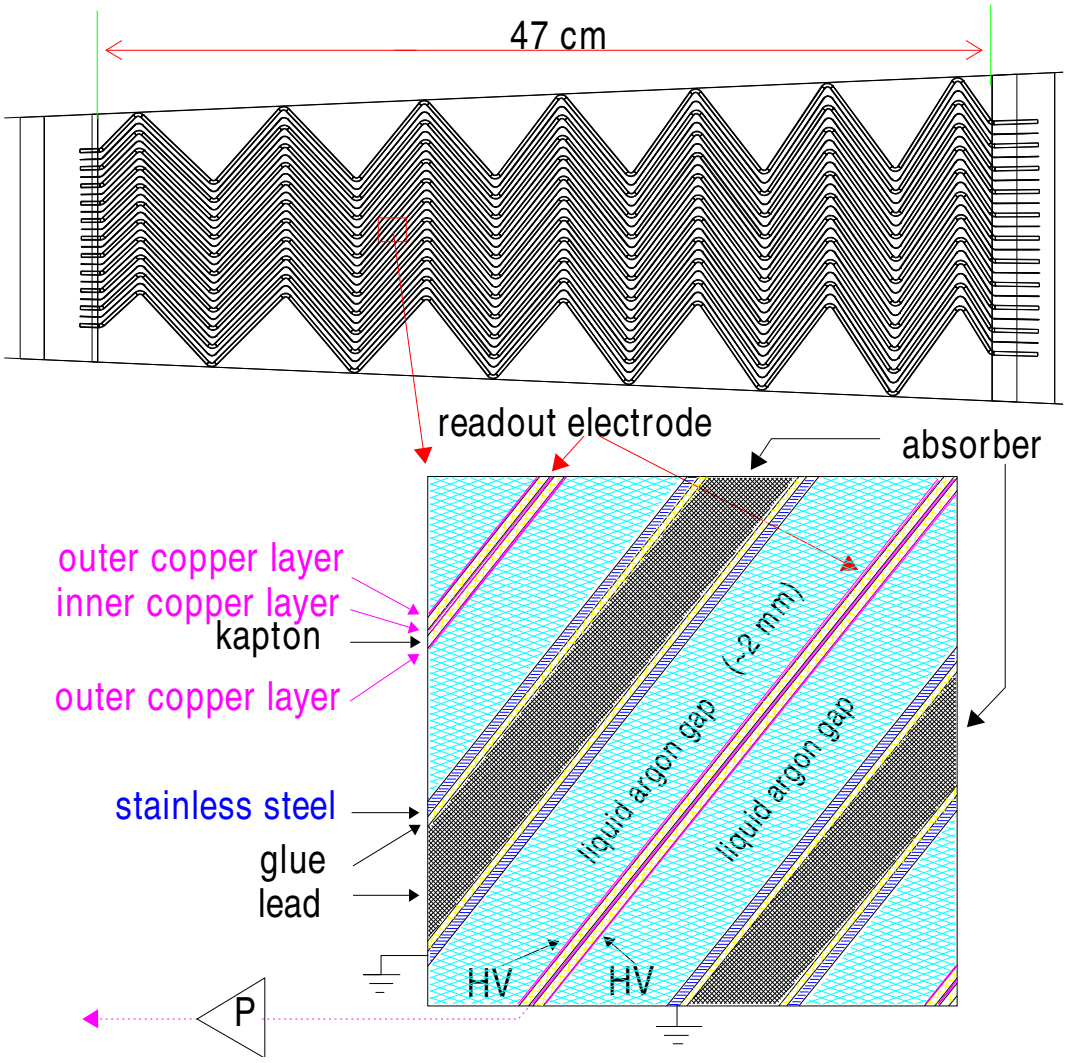

Figure 3.1: Geometry and structure of the barrel electrodes [37].

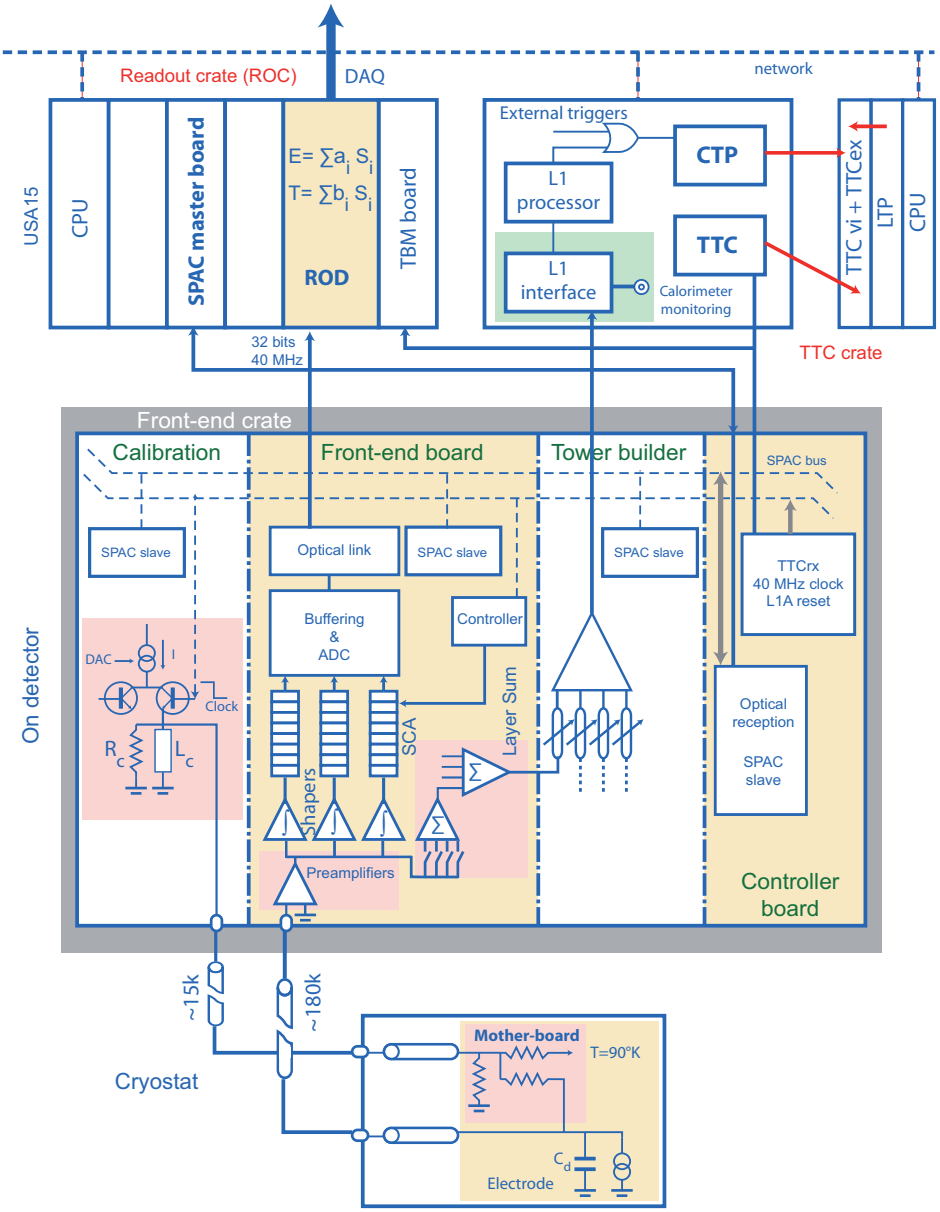

Figure 3.2: Block diagram of the LAr readout electronics. The electrical circuit in the LAr is depicted at the bottom, followed above by the on-detector front-end electronics crate and at the top (left) by a schematic view of the readout crate with its ROD boards and TTC modules. In this diagram warm preamplifiers are located in the FEB. This is the case for the EM and FCal1 calorimeters while for the HEC the preamplifiers are located in the LAr. Also indicated at the middle and top (right) are the LAr front-end tower builder electronics and the interfaces to the L1 trigger system with its central trigger processor (CTP) [34].

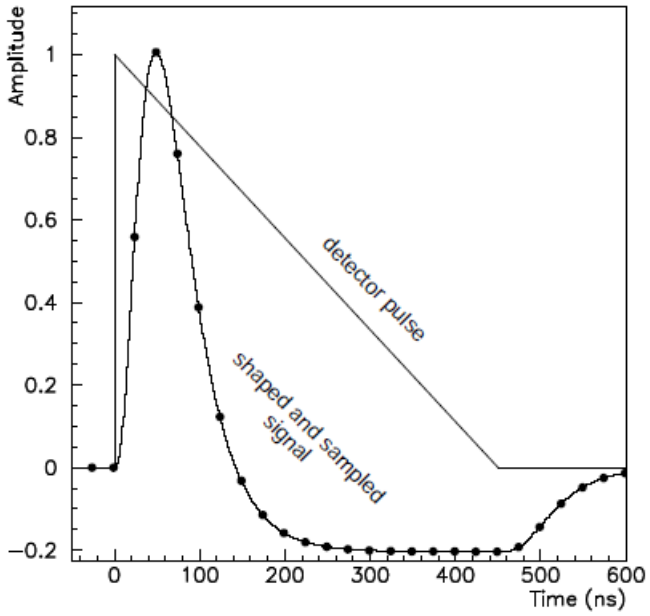

Figure 3.3: Ionisation pulse in a LAr cell and FEB output signal after bi-polar shaping. Also indicated are the sampling points every 25 ns. During normal data-taking the signal is sampled 5 times (or 7 times for some cosmics runs). A maximum of 32 samples can be attained and is used for calibration purpose (OFCs) [39].

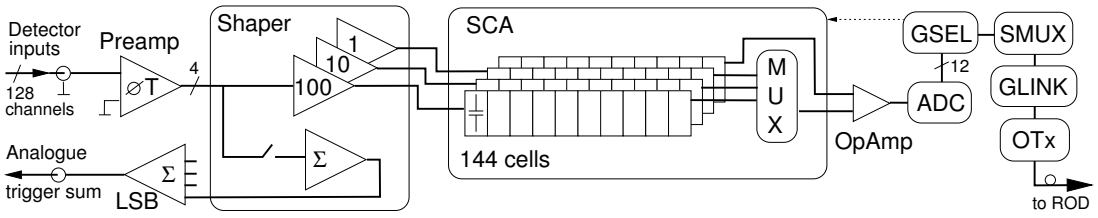

Figure 3.4: Block diagram of the FEB architecture, depicting the data-flow for four of the 128 channels [34].

and to prepare the input for the tower builder boards. Towers of calorimeter cells are used for the L1 trigger [34] [38] [41].

3.2.2 LAr electronic calibration

To calibrate the energy response of the LAr calorimeter a system of electronics calibration boards [43] (situated in the front-end crate) is used to send precise pulses to the electrodes. A voltage pulse set by a 16-bit DAC (Digital-to-Analog Converter) which simulates the physics signal is applied across an injector resistance R_{inj} of very precise value in the cold directly on the electrode. In the FCal, the pulse is applied at the base-plane of the front-end crates where it is split in two. One of the split pulses goes directly into the FEBs and is used for calibration. Non-uniformity of the calibration pulse amplitude affects directly the constant term in the energy resolution function and therefore the measurement of high energy electromagnetic showers. The calibration system is designed to limit this contribution to the constant term to less than 0.25% for the EM calorimeter, less than 1% for the HEC and less than 2% for the FCal [34].

There are three different types of calibration runs taken in periods without beam collisions (such as the time between LHC fills) in order to equalise the response of the LAr calorimeter cells: pedestals, delays and ramps. Sets of calibration runs are acquired for each of the three LAr electronic readout gains (high, medium, and low). During *pedestal* runs no signal is injected into the calorimeter cells thus the electronics baseline level and the electronic noise for each cell are measured. *Delay* runs measure the shape of the pulse as a function of time for each readout cell. *Ramp* runs are used to extract the response of each cell as a function of the injected current in DAC units. The values of the current used varies according to the gain of the electronics being probed [42].

3.2.3 LAr calorimeter back-end electronics

The digital signals from the FEBs are then transmitted via optical links to the back-end electronics which are located in the main cavern, 70 m away from the detector. The Readout Driver system (ROD), the core of the back-end electronics, digitally processes the data before transmitting it to the data acquisition system at a L1 trigger rate of 75 kHz.

Each ROD module receives data from up to 8 FEBs (ie. up to 1024 channels) through 8 optical fibres. The ROD motherboard houses 4 processing units (PU) and each PU is equipped with two Digital Signal Processors (DSP), thus each DSP processes one FEB. Each DSP is preceded by an input FPGA (InFPGA) used to perform quality checks of the input data.

The DSP has three main tasks:

- synchronise the FEB data with the Trigger-Time and Control (TTC) signals,

- process the data coming from the InFPGA and apply an optimal-filtering method to compute the energy, time and a quality factor of the signal for each cell and
- prepare and send the data to the ROD motherboard.

3.3 Digital Signal Processor

In Figure 3.5 a photograph of the DSP is shown. As anticipated from the introduction, the DSP computes the energy, time and quality factor of the signal for each cell and transmits to DAC the five measured samples for cells with energy above a given threshold. The author of this thesis has worked on the validation of the DSP code and on the monitoring of its response.

The main constraints on the DSP computation are summarised below. These constraints have an impact on the precision of the DSP calculations.

- Since the DSP needs to send the results at a L1 trigger rate of 75 kHz, the **time** for each DSP to process the whole FEB is required to be less than ~ 12 μsec on average.
- The constants needed for the DSP computations have to be formatted and packed — since the DSP only performs integer computations — before being loaded on the DSP to reduce the **memory consumption**.
- In order to minimise the **bandwidth** needed for the transmission of the DSP results, it is essential to minimise the amount of data sent while keeping maximum information.

3.3.1 Principle of the Calculations

The first calculated quantity is the cell **energy**. This is done according to the following formula:

$$E = \underbrace{F_{DAC\rightarrow\mu A} \times F_{\mu A\rightarrow MeV} \times C_{HV} \times \frac{1}{\frac{M_{phys}}{M_{cal}}}}_{f} \times (R_0 + R_1 \times A_{ADC}) \tag{3.1}$$

where each term is explained below.

- A_{ADC} is the peak amplitude of the signal pulse in ADC counts and is computed as

$$A_{ADC} = \sum_{i=0}^{N_{samples}-1} \mathrm{a}_i (s_i - p)$$

where p is the pedestal, s_i the digitised signal samples in ADC counts, a_i the energy optimal filtering coefficients (OFCs) and $N_{samples}$ is the number of samples used for the computation

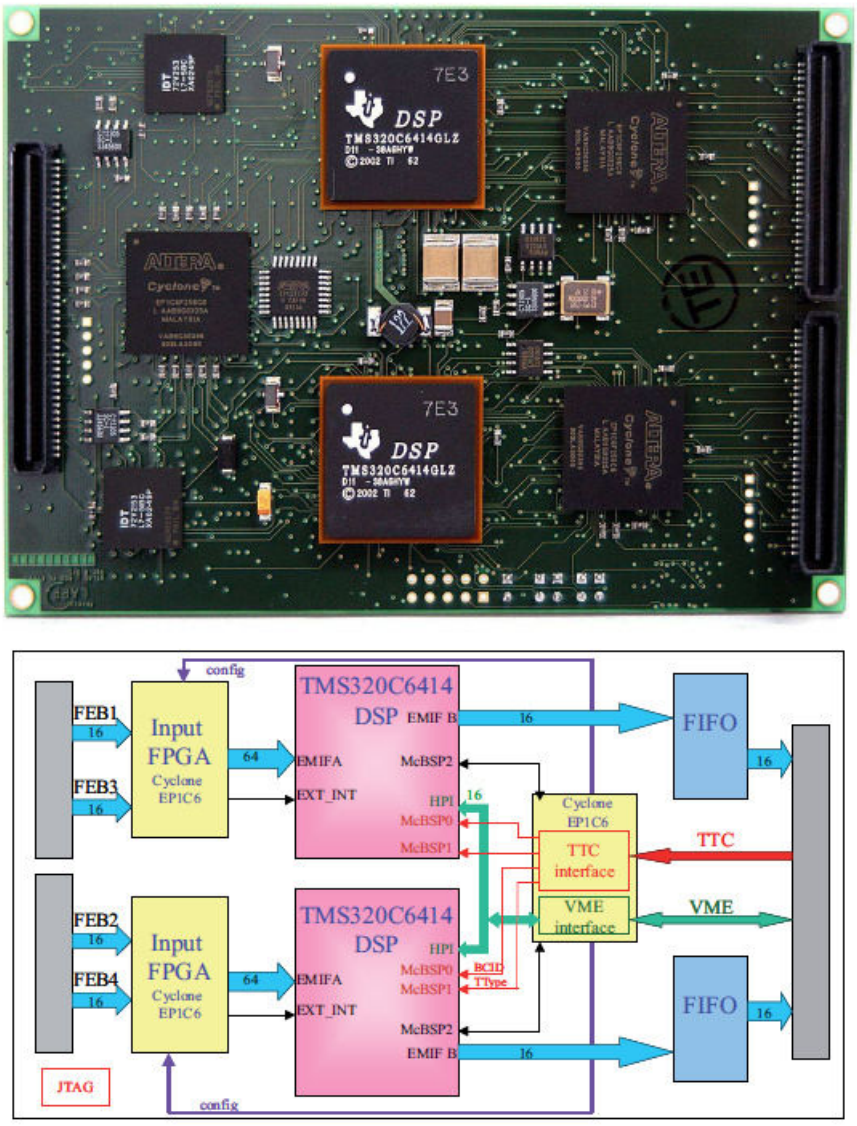

Figure 3.5: *Top:* photograph of the ROD PU with its two clearly visible DSPs. The PU measures 120 mm × 85 mm. *Bottom:* block diagram of the PU board with two TMS320C6414 Texas Instruments DSPs [39].

(typically $N_{samples} = 5$). (see Fig. 3.3) [42]. The Optimal Filtering method is a digital filtering technique which allows to compute the peak amplitude of the signal minimising the effect of the electronic and pile-up noise [44]. It requires the knowledge of the shape of the ionisation pulse. This shape is predicted from the information contained in the calibration pulses obtained in delay runs.

- R_0 and R_1 are coefficients linking the known injected amplitude (DAC) to the analog signals (ADC) measured in calibration runs ("ramps") (see Fig. 3.6).

- $F_{DAC\rightarrow\mu A}$ is a factor that converts the current measured in DAC units to μA, and accounts for the values of the local motherboard injection resistor.

- The factor $F_{\mu A\rightarrow MeV}$ converts the current to a raw estimate of the energy released in the active and passive part of the calorimeter cell using an average value of the sampling fraction.

- The factor $\frac{M_{phys}}{M_{cal}}$ corrects for the difference between the calibration and the ionisation pulse shape and is computed from the calibration pulse and from the properties of the readout cells.

- C_{HV} is a correction factor applied when the high voltage is not nominal.

When the energy is greater than a certain threshold (currently $5\sigma_{noise}$) then the time and the quality factor are computed for that cell. The **time** of signal with respect to the LHC clock is given by the following equation:

$$\tau = \frac{\sum_{i=0}^{N_{samples}-1} b_i(s_i - p)}{A_{ADC}} \tag{3.2}$$

where b_i are the timing OFCs.

A **quality factor** Q with a χ^2-like behaviour, ignoring the correlations between the sampling points, is computed to quantify the quality of the measurement:

$$Q = \sum_{i=0}^{N_{samples}-1} [(s_i - p) - A_{ADC}(g_i - g'_i\tau)]^2 \tag{3.3}$$

where g_i is the normalised predicted ionisation pulse shape (after shaping), calculated from calibration pulse shapes and g'_i its derivative.

3.3.2 DSP Constants and Computations

In order to get a good compromise among the computation time, memory consumption and precision of the computation, the constants are properly calculated, rounded and packed (as explained in Section 3.3.3) before being loaded on the DSP for each cell and electronic gain. The eq. 3.1

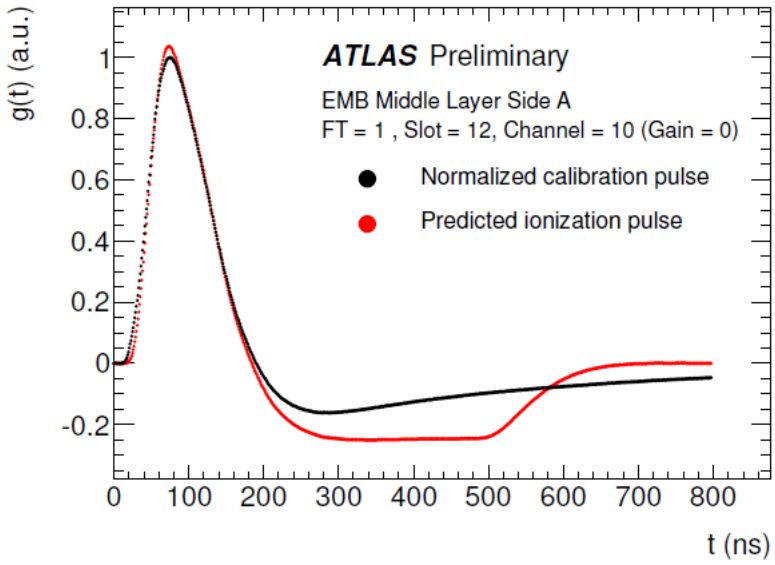

Figure 3.6: Comparison between the calibration (black) and physics pulse (red) for a middle cell in the EM barrel [42].

can be written as:

$$E = \sum_{i=0}^{N_{samples}-1} \underbrace{fR_1 a_i}_{\alpha_i} s_i - \sum_{i=0}^{N_{samples}-1} \underbrace{fR_1 a_i}_{\alpha_i} p + fR_0 \tag{3.4}$$

where f is the product of all the conversion and correction factors presented in eq. 3.1. In order to perform all possible calculations before the DSP, this equation is then arranged in the following way:

$$E = \sum_{i=0}^{N_{samples}-1} \alpha_i s_i - \underbrace{\underbrace{(p - \frac{fR_0}{\sum \alpha_i})}_{p'} \sum_{i=0}^{N_{samples}-1} \alpha_i}_{P_a} \Longrightarrow \boxed{E = \sum_{i=0}^{N_{samples}-1} \alpha_i s_i - P_a} \tag{3.5}$$

For the signal time computation the following expression is used:

$$E\tau = \sum_{i=0}^{N_{samples}-1} \underbrace{fb_i}_{\beta_i} s_i - \underbrace{\sum_{i=0}^{N_{samples}-1} fb_i p}_{P_b} \Longrightarrow \boxed{E\tau = \sum_{i=0}^{N_{samples}} \beta_i s_i - P_b} \tag{3.6}$$

Since it is not possible to perform a division on the DSP, a look-up table (LUT) containing inverse energies is loaded on the DSP and is used to calculate the time τ from the $E\tau$ product.

The quality factor is computed as

$$Q = \sum_{i=0}^{N_{samples}-1} [(s_i - p) - E(h_i - h'_i\tau)]^2 \tag{3.7}$$

where $h_i = g_i / fR_1$ and h'_i its derivative.

3.3.3 Packing of the Input

The calibration constants that are packed and loaded on the DSP are summarised on Table 3.2. The middle sample is read first meaning that the samples arrive into the ROD in an unnatural order: s_2, s_0, s_1, s_3, s_4. The samples sent to the DSP are 12-bit integers and are left-shifted by 2 (ie. multiplied by 2^2) in order to achieve the desired precision for the computations. On the DSP sums and subtractions are done on 32 bits while multiplications on 16 bits in order to have the results in 32 bits which are then further packed. For the quality factor case, the samples s_i and the pedestal P are 16-bit numbers and the result of the multiplication is packed in 16 bits leading to a 32 bit result when squared. The LUT contains 2048 entries of 12-bit inverse energies stored as 16-bit integers.

Typically the α_i OFC values at high gain for cells in the EM barrel are ~ 1. In order to make use of the available 16 bits and provide a good precision measurement, these quantities are rescaled and packed in a given way. Taking as an example the α_i OFCs and the P_a pedestal used for the energy computation, the following procedure is used to pack the constants. First, a scale n_α is found to transform the α_i coefficients into 16-bit integers such that $2^{14} \leq \alpha_j \cdot 2^{n_\alpha} < 2^{15}$ where α_j is the OFC with the highest value. Secondly, a scale n_p is found to transform the pedestal P_a into a 32-bit integer such that $2^{31} \leq P_a \cdot 2^2 \cdot 2^{n_p} < 2^{32}$. The 2^2 factor is due to the fact that the samples are left-shifted by 2. Finally, the OFCs and the pedestal are scaled by the smaller of the two constants $n_a = \min(n_\alpha, n_p)$ to avoid overflows. A similar procedure is used for the time and quality factor constants.

3.3.4 Packing of the Results

The LAr electronics have been designed taking into account that the energy recorded in a single cell of the LAr calorimeter covers a wide range from a few tens of MeV to a few TeV meaning that a simple packing of the energy as a 16-bit integer is not enough. On the other hand, packing the energy on 32 bits would have an impact on the DSPs performance and on the size of the information to be transmitted. Therefore, four energy ranges are defined each one with a different value for the lowest significant bit (LSB) (see Table 3.3). The LSB of the 13 bit word carrying the energy value defines the precision of each energy range. The precision of the DSP measurement matches the energy resolution.

range	sign	value
2 bits	1 bit	13 bits

The energy, as shown above, is thus packed as a 16-bit integer where the first two bits define

Constant	Formula	Number	Format
α_i	$a_i f' 2^{n_a}$	5	16 bits
n_a	-	1	16 bits
P_a	$2^2 \sum \alpha_i (p - \frac{fR_0}{\sum \alpha_i})$	1	32 bits
β_i	$b_i f' 2^{n_b}$	5	16 bits
n_b	-	1	16 bits
P_b	$2^2 p \sum \beta_i$	1	32 bits
h_i	$2^{n_h} g_i / f'$	5	16 bits
h'_i	$2^{n_h} g'_i / f'$	5	16 bits
n_h	-	1	16 bits
P	$2^2 p$	1	16 bits
R_0	$F_{DAC \to \mu A} F_{\mu A \to MeV} \frac{1}{\frac{M_{phys}}{M_{cal}}} C_{HV} R_0$	1	16 bits
Number of constants per channel and per gain		27	

Table 3.2: Packed constants that are loaded on the DSP ($f' = fR_1$). The energy, time and quality factor OFCs are scaled by 2^{n_a}, 2^{n_b} and 2^{n_h} respectively in order to have maximum precision when packed as 16-bit integers [41].

the four different ranges, one bit is used for the sign of the energy and the value is given in the last 13 bits. The value of the LSB in each energy range is $2^{3\times \text{range}}$ (range=0, 1, 2, 3) thus the energy values to be stored can vary within $|E| < 2^{13} \cdot 2^{3\times 3} = 2^{22}$ MeV$(\simeq 4$ TeV$)$.

Range	Energy value (MeV)	LSB
0	$\|E\| \leq 2^{13}$	1 MeV
1	$2^{13} < \|E\| \leq 2^{16}$	8 MeV
2	$2^{16} < \|E\| \leq 2^{19}$	64 MeV
3	$2^{19} < \|E\| \leq 2^{22}$	512 MeV

Table 3.3: Energy values and the precision for each energy range are presented [41].

The time value is packed as a 16-bit signed integer in units of 10 ps allowing unsaturated time measurements up to $\tau = 2^{15} \cdot 10$ ps $= 327680$ ps. The quality factor Q is stored as a 16-bit unsigned integer (see Table 3.4).

3.4 Role of the DSP computations

An important role of the DSP is to reduce the size of information to be transmitted and stored (event size). During collision runs, the DSP computation of the energy is performed for all cells but the samples are transmitted and stored only for the cells that have an absolute energy above a

given threshold. The threshold can vary from 2σ to 5σ of the noise depending on the luminosity. For cells below the threshold only the energy value is stored. For cells above the threshold the time and quality factor are computed and in addition the samples are stored. As a result, the event size is reduced by a factor of 2. Currently due to bandwidth limitations, the samples can be transmitted for a maximum of 10% of the LAr cells. This makes the precision of the DSP computations all the more important since it is not possible to recompute offline the energy, time and quality factor of the signals in at least 90% of the cells since the samples are not present.

It is worthwhile to notice that all cells, including those with a signal of less than 5σ, contribute to the reconstruction of clusters associated to physics objects like E_T^{miss}, jets, electrons, photons and muons. The quality factor computed by the DSP for cells above a given threshold is used in the L2 trigger in particular for jet cleaning and in the EF trigger for the E_T^{miss} cleaning. At least 20% of the L2 jet trigger rates is reduced thanks to the use of the quality factor. For these reasons, it is essential to monitor the correct behaviour of the DSP calculations during data-taking. There are two situations in which it is particularly important to check the DSP behaviour during data-taking: when the calibration constants are updated (in particular when new sets of OFCs are available) and when the algorithm performing the calculations is changed.

3.5 Validation of the DSP Computations

The aim of the validation of the DSP code and of the monitoring of the DSP results is therefore:

- to verify that the *code* loaded on the DSP is correct and that the computations are done in a proper way (reordering, operations, ...),
- to make sure that the limited *precision* of the constants used on the DSP does not bias the expected precision of the computation and
- to check that the constants loaded on the DSP are *updated*.

The validation and monitoring tasks can be done:

- by analysing directly the DSP results (“online results”),
- by comparing the DSP results with values computed offline using the complex ATLAS framework ATHENA (“offline results”) and
- by comparing the DSP results with values computed offline using a standalone program called DspTest (“offline test results”).

The offline results can be performed using full precision. While the verification that the calibration constants are properly updated can be done only “online”, the correct behaviour of the algorithm and the effect of the limited precision can be checked online and offline.

Quantity	Range	Precision
Energy [MeV]	$\|E\| \leq 2^{13} = 8192$ MeV	$\Delta E \leq 1$ MeV
	$2^{13} < \|E\| \leq 2^{16} = 65536$ MeV	$\Delta E \leq 8$ MeV
	$2^{16} < \|E\| \leq 2^{19} = 524288$ MeV	$\Delta E \leq 64$ MeV
	$2^{19} < \|E\| \leq 2^{22} = 4194304$ MeV	$\Delta E \leq 512$ MeV
Time [ps]	$\|\tau\| \leq 327680$ ps	$\Delta\tau \leq 10$ ps
Quality factor	$Q \leq 65536$	$\Delta Q/\sqrt{Q_{\text{offline}}} \leq 1$ (when no saturation has occurred)

Table 3.4: Ranges and online precision for energy, time and quality factor. ΔQ is defined as the difference between Q_{offline} and Q_{online}.

3.5.1 Offline Test Results

The DspTest code emulates the computations performed both on the DSP (limited precision) and offline (full precision) allowing to check the computation and the expected precision on the energy, time and quality factor. In addition, it can use a given set of samples to generate new pulses allowing to test changes in the code on a large scale.

The left plot in Fig. 3.7 shows the online cell energy E_{online} as calculated on the DSP as a function of the E_{offline} calculated with full precision by the DspTest code. The right plot shows the difference between the energy values E_{online} and E_{offline} as a function of the energy. The numerical precision for the energy computation is clearly visible and the three (out of four) energy ranges are seen at approximately 8 GeV and 64 GeV. As mentioned earlier, for each energy range the precision is different and is given by the value of the LSB.

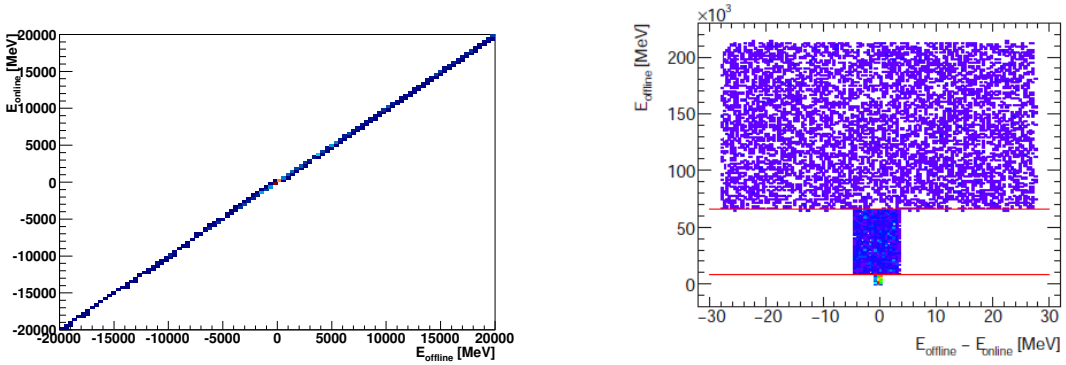

Figure 3.7: Example of validation plots from events generated by the DspTest code. E_{online} is the cell energy computed by emulating the DSP response and E_{offline} the energy computed with full precision.

The expected precision for the **time** computation is 10 ps (1 LSB). However, for large times or equivalently for small energies, time differences higher than 10 ps are observed due to the limited precision of the LUT (Fig. 3.8). It has been checked that this fact doesn't cause any

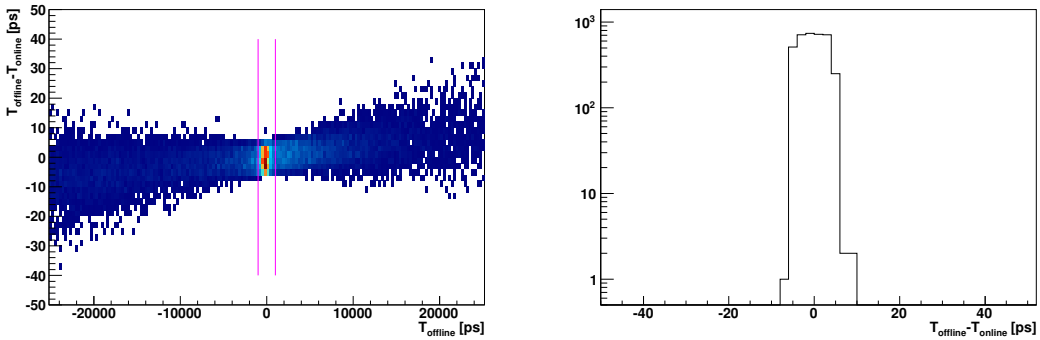

Figure 3.8: Example of validation plots from events generated by the DspTest code. T_{online} is the cell time computed by emulating the DSP calculation and T_{offline} the time computed using full precision. The distributions are within ± 10 ps apart from low energies and large times where the precision of the LUT dominates. A cut on the cell energy $E > 500$ MeV is applied. The *right* plot shows the difference between T_{offline} and T_{online} for the cases where T_{offline} is within ± 1 ns.

problems since the lack of precision affects very large times and during collisions the good signals are all aligned in time with less than 1 ns.

For the **quality factor** the quantity $(Q_{\text{offline}} - Q_{\text{online}})/\sqrt{Q_{\text{offline}}}$ is used to assess the precision of the computation. Originally the quality factor was computed using a simpler formula without taking into account the derivative of the pulse

$$Q = \sum_{i=0}^{4} [(s_i - p) - Eh_i]^2 \tag{3.8}$$

and in this case it was observed that the values of $(Q_{\text{offline}} - Q_{\text{online}})/\sqrt{Q_{\text{offline}}}$ were within ± 1 thus the quantity $\Delta Q/\sqrt{Q}$ was chosen to assess the precision. During the last year, an extra term $h'\tau$ has been added as shown in eq. 3.7. This extra term has been introduced to account for time shifts of the physics pulse with respect to the sampling time. Using the new formula there are cases where the online computation saturates causing a mismatch between the offline and online values and the limit of ± 1 in no longer respected. This mostly happens for small energies and large times. Since some of the variables responsible for the saturation are already stored on the DSP as 32-bit integers it is impossible to increase their accuracy to avoid this effect. Fig. 3.9 displays the precision of the quality factor computation for events generated with the DspTest code.

3.5.2 Validation during collision runs

During data-taking (cosmics, proton-proton collisions, heavy ion collisions) the DSP computations have to be constantly monitored. A number of plots are available in real time to monitor the computation and compare the offline and online results. In case of mismatch between these values additional plots are filled to inform the shifters. Depending on the nature of these mismatches, the

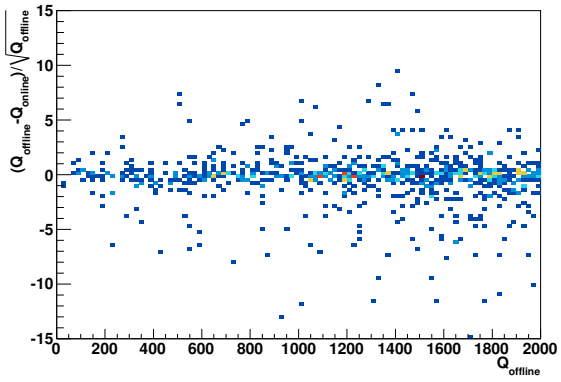

Figure 3.9: Distribution of $(Q_{\text{offline}} - Q_{\text{online}})/\sqrt{Q_{\text{offline}}}$ as a function of Q_{offline} obtained with the DspTest code. The values of this quantity are not within ± 1 due to saturation of certain quantities on the DSP (see paragraph 3.5.3).

Data Quality Monitoring Display (DQMD) will turn red for the specific partition triggering these errors. The data for the specific period during which DQMD is red will be flagged accordingly to inform the user of the problem. Immediate action has to be taken since as explained in Section 3.4 a malfunctioning of the DSP calculation would impact the energy reconstruction.

The plots presented in this section are from a 2011 proton-proton run. Fig. 3.10 shows the difference between the online and offline cell energies, Fig. 3.11 the difference between the online and offline cell timing and Fig. 3.12 the correlation between the Q_{online} and Q_{offline}.

A special attention has to be devoted when new constants are available. In particular, when the new OFC constants have quite different values from the previous ones, a test of the DSP code is necessary to ensure that the DSP computations and their precision are not affected. This usually happens when the new OFCs are computed for different pile-up conditions. In this case, the new constants are fed to the DspTest code and the energy, time and quality factor computations are performed for real and generated pulses. The results are then analysed looking at the overall behaviour and for strange features.

3.5.3 Specific examples of DSP code validation and improvements

In this section, two selected examples of subtle effects that have been found are given showing the work of the author of the thesis regarding the validation and improvement of the DSP code computations.

Correcting Time and Quality factor computations

As mentioned earlier (Section 3.4), the energy of the cell is computed first and if it is above a given threshold then the time and the quality factor of that cell are computed using the measured

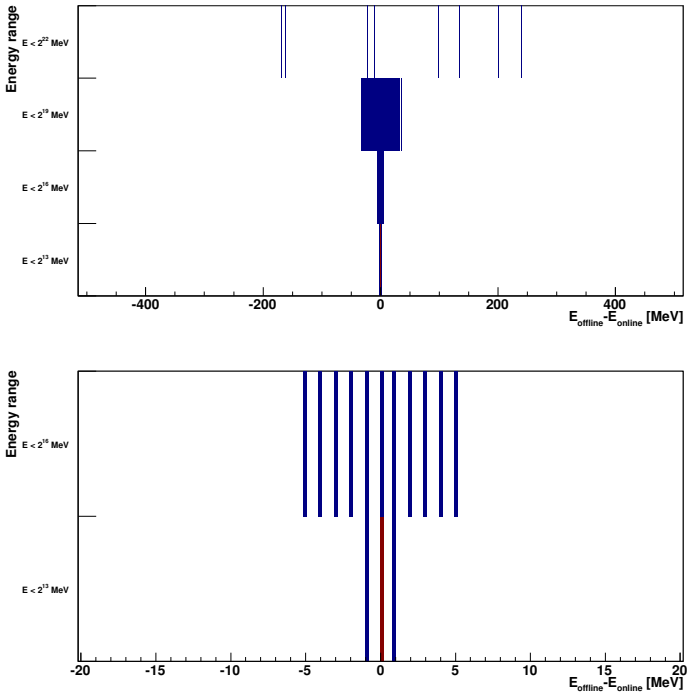

Figure 3.10: Online monitoring plots of the DSP behaviour showing the difference between the E_{online} and E_{offline} for the four different energy ranges. The second plot shows a detailed view of the first two energy ranges where one can see that the ΔE is within the expected precision (1 MeV for the first energy range and 8 MeV for the second one).

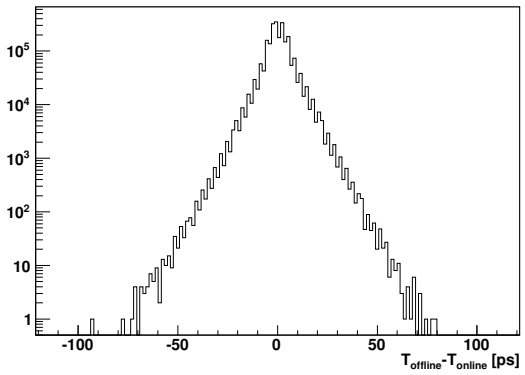

Figure 3.11: Online monitoring plots of the DSP behaviour showing the distribution for the difference of T_{offline} and T_{online}. The majority of the events are within ± 10 ps. Larger differences are also observed because of the usage of the LUT.

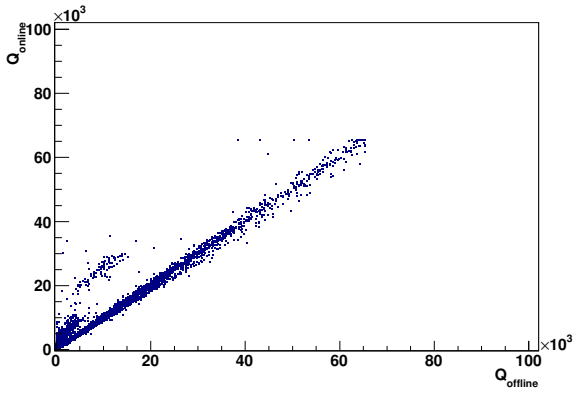

Figure 3.12: Plot produced online during data-taking showing the correlation between Q_{offline} and Q_{online}. For the points that are not on the $Q_{\text{online}} = Q_{\text{offline}}$ line, saturation has occurred on the DSP computation as explained in paragraph 3.5.3.

energy. Extensive and careful comparison between the results given online from the DSP, offline by ATHENA and the results from the DspTest code were performed. During this work, a mismatch between the time and quality factor was noticed after feeding the same constants and samples while the energy was the same in all cases. Careful comparison of all steps of the computation allowed to find out that this was the result of the following feature: for medium and low gain the ramp intercept is used for the energy calculation (eq. 3.1) and then this energy was used for the time and quality factor computation on the DSP. Since the constants need to be packed in a specific way, the online energy is computed directly while the offline calculation computes the amplitude first. This caused the following effect:

$$\begin{array}{cc} \text{offline} & \text{online} \\ A\tau = \sum_{i=0}^{4} b_i(s_i - p) & E\tau = \sum_{i=0}^{4} f \cdot R_1 \cdot b_i(s_i - p) \\ \tau = \dfrac{A\tau}{A} = \dfrac{\sum_{i=0}^{4} b_i(s_i - p)}{\sum_{i=0}^{4} a_i(s_i - p)} & \tau = \dfrac{E\tau}{E} = \dfrac{\sum_{i=0}^{4} f \cdot R_1 \cdot b_i(s_i - p)}{f \cdot R_0 + \sum_{i=0}^{4} f \cdot R_1 \cdot a_i(s_i - p)} \end{array}$$

and similarly for quality factor Q. The term fR_0 in the denominator causes a difference between the online and offline values. To fix the mismatch, this new term had to be loaded on the DSP and the additional computation $E - fR_0$ had to be performed on the DSP before the time and quality factor computation. In order to avoid memory problems and have backward compatibility, the pedestal variable for the quality factor computation P that was stored as a 32-bit variable but only the last 16-bits were used, was split in two 16-bit variables: one to store the term fR_0 and one for the pedestal P.

Improving the quality factor computation

As mentioned above, the quality factor was originally computed with the simpler formula shown in eq. 3.8. Later, it appeared clear that a more accurate measurement of the quality factor was needed since it had to be used at the L2 trigger to reduce the trigger rate. Therefore the quality factor computation was changed to include the derivative of the pulse shape in order to take into account possible shift of the physics pulse with respect to the sampling time (eq. 3.7). Several iterations and checks of this new algorithm were made.

First, the size of the memory where the constants per channel are stored had to be increased to store the new h'_i OFCs. To optimise the response of the DSP, in addition to these five constants, three more variables (dummy variables) were loaded on the DSP thus increasing the size of the memory occupied by the loaded constants by 128 bits per channel. After this change, the monitoring plots showed saturation for all cases when the quality factor was computed. This was solved by emulating the DSP computation using the DspTest code and checking closely every step of the computation. This problem was found to be due to the DSP selecting the wrong constants (dummy variables) from the memory.

Only after this correction it was possible to spot problems coming directly from the computation. The computation of the quality factor had changed significantly since five additional computations (one per sample) were now performed. The monitoring plots still showed cases of saturation and cases of mismatches between the online and offline Q computation. After checking again the computation step-by-step it was found that there were cases (mostly for high time values) where the Q computation would saturate only for one or two out of the five samples. This could result to either a saturated value or to a non-saturated value which was of course different from the expected one. To account for this problem, two variables had to be moved from 16 to 32 bits. Even though this reduced the saturation cases, it was still not enough and cases of saturation were still observed. Since the result of this computation was already stored as a 32-bit number it was impossible to further increase the number of bits using a single word.

All these changes on the DSP code along with the fact that the single loop for the time and quality factor computation was split (since now the time is used for the quality factor computation), reduced the optimisation of the DSP code and increased significantly the computation time. Currently, the algorithm for the τ and Q computation can only be performed for 10% of the FEB cells. In practice, today the fraction of cells treated is at the level of a few percent.

Chapter 4

Performance Studies

This chapter summarises the electron reconstruction and identification and the reconstruction of the missing transverse energy (E^T_{miss}) in the ATLAS experiment. These are crucial elements for the selection of events with a W boson decaying into an electron and neutrino.

The electrons from a collision event deposit their energy in many calorimeter cells. The raw cell energies are measured and then the cells are grouped into clusters using dedicated clustering algorithms. In ATLAS two main clustering algorithms are used: the "sliding-window" and the topological clustering algorithm. The cluster is then matched to a track in the Inner Detector to form an electron candidate. and then they are calibrated to reconstruct the particle energy. Finally in order to distinguish whether the cluster has been produced by an electron or by any other particle, a set of identification cuts are applied.

Neutrinos and any other hypothetical particles that interact very weakly with matter, escape detection in the experiment. The transverse missing energy, E_T^{miss}, in the final state is a signature of the presence of these particles. Events with large E_T^{miss} are also the key signature for new physics such as supersymmetry and extra dimensions. An important requirement on the way in which the analyses have to use the E_T^{miss} measurement is to minimise the impact of the limited detector coverage, finite detector resolution, presence of dead detector regions and different sources of noise that produce fake E_T^{miss}. A good measurement of the E_T^{miss} in terms of linearity and resolution is important for many physics analyses [48].

Another important element of the W boson analysis is the charge misidentification rate for electrons and positrons which will be presented in some detail in this chapter since the author of this thesis has worked on this topic.

4.1 Electromagnetic Cluster Reconstruction

4.1.1 Sliding-Window Clustering

Two kinds of sliding-window clusters are built by the ATLAS offline reconstruction program: *electromagnetic* clusters which are based on the information from the EM calorimeter only mainly and are used mainly for electron and photon detection, *combined* clusters that are used for jet and tau detection and combine the information from both the EM and hadronic calorimeter. Here we will only focus on the electromagnetic sliding-window clusters.

Tower Building

The first step of the sliding-window algorithm is to divide the EM calorimeter into a grid of 200×265 elements in $\eta - \varphi$ of size $\Delta\eta \times \Delta\varphi = 0.025 \times 0.025$ (as shown in Table 2.3, this is the size of the second layer cells of the EM calorimeter). Inside each of the grid elements, the energy of the cells from the three longitudinal calorimetric layers are summed to form the tower energy. The energies of cells shared between towers in the strips and in the back layer of the EM calorimeter are distributed according to the fractional area of the cells intersected by each tower.

Sliding-Window Precluster (Seed) Finding

A window of fixed size $\Delta\eta \times \Delta\varphi = 0.075 \times 0.125$ is moved across each element of the tower grid. If the transverse energy of the window is a local maximum and if it is above a threshold of 2.5 GeV, a precluster is formed.

The position of the precluster is computed as the energy weighted η and φ barycentres of all the cells within a window around the cell at the centre of the precluster. This window has a smaller size ($\Delta\eta \times \Delta\varphi = 0.075 \times 0.075$) in order to make the position calculation less sensitive to noise. When the barycentres of two preclusters are closer than $\Delta\eta \times \Delta\varphi = 0.050 \times 0.050$, only the precluster with the highest transverse energy is kept.

EM Cluster Formation

As a final step, an EM cluster is filled by taking all cells within a fixed-size rectangle. The size of this rectangle is $\Delta\eta \times \Delta\varphi = 0.075 \times 0.175$ (0.125×0.125) in the barrel (end-cap) for electrons and converted photons and $\Delta\eta \times \Delta\varphi = 0.075 \times 0.125$ (0.125×0.125) in the barrel (end-cap) for unconverted photons. In the end-cap, the cluster size is the same for both electrons and photons since the effect of the magnetic field is smaller. It is larger in η than in the barrel because of the smaller physical size of the cells.

The filling of the cluster is done in the following order: first the middle layer is filled using

the precluster barycentre as seed, then the strip layer is filled using the barycentre of the middle layer as the seed position and finally the presampler and the back layer cells are added using the barycentre of the strips and middle layer as seed position respectively [45].

4.2 Electron Reconstruction

The standard electron reconstruction in ATLAS (also referred to as "egamma") is based on clusters reconstructed in the EM calorimeter which are then associated with tracks reconstructed in the Inner Detector.

The tracks are matched to the clusters by extrapolating from the last measurement to the second sampling of the EM calorimeter taking into account the magnetic field and the material in between. An electron object is formed when the difference between the η and φ parameters of the extrapolated track and the η and φ of the cluster satisfy the following criteria: $\Delta\eta < 0.05$ and $-0.1 < q \cdot \Delta\varphi < 0.05$ where q is the sign of the lepton. In case of more than one tracks satisfying this requirement, tracks with silicon hits are given priority compared to TRT only tracks. If there is more than one track satisfying this criterion, the best matched one is considered to be the one that has the smallest distance $\Delta R = \sqrt{(\Delta\eta^2 + \Delta\varphi^2)}$ between the extrapolated track position and the cluster barycentre [48].

4.3 EM Cluster Energy Calibration

There are two calibration methods used in ATLAS in order to obtain the cluster energy: the longitudinal weight method and the calibration hits method. Here the calibration hits method which is used by default is briefly explained.

In order to compute the energy of the electron or photon energy and correct for energy losses described in Fig. 4.1, a calibration procedure using the energy deposition in the calorimeter is applied. The calibration hit method is based on Monte Carlo simulation and uses a parametrisation of four different contributions: the energy deposited in the material in front of the calorimeter (including the energy deposition in the presampler), the energy deposited in the EM calorimeter inside and outside the cluster and the energy deposited beyond the EM calorimeter (longitudinal leakage). The calibrated energy is reconstructed using the following formula:

$$E_e = \underbrace{a(E_{tot}^{Acc},\eta) + b(E_{tot}^{Acc},\eta)\cdot E_{ps}^{clLar} + c(E_{tot}^{Acc},\eta)\cdot (E_{ps}^{clLar})^2}_{\text{Energy in front}} + \underbrace{\frac{s_{cl}^{Acc}(X,\eta)}{f_{out}(X,\eta)}\cdot\left(\sum_{i=1}^{3} E_i^{clLar}\right)}_{\text{Energy in the accordion}}\cdot\underbrace{(1+f_{leak}(X,\eta))}_{\text{Longitudinal leakage}}\cdot\underbrace{F(\eta,\varphi)}_{\text{Energy modulation}} \quad . \tag{4.1}$$

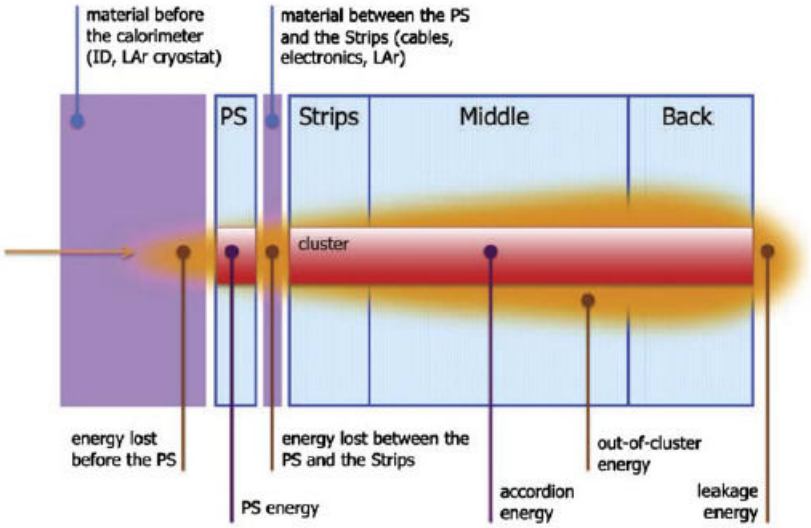

Figure 4.1: Schematic view of an electromagnetic shower developing in the ATLAS LAr calorimeter. The shower may start developing before it reaches the presampler loosing some energy in the material in front of the calorimeter. Some part of the shower energy is lost in the material between the presampler and the first calorimeter layer. The "out-of-cluster energy" corresponds to the energy which is lost when the size of the cluster is smaller than the shower lateral extension. The "leakage energy" is the energy lost if the shower is not contained by the calorimeter depth [46].

The terms of the equation are explained below.

- E_e is the electron or photon candidate energy.
- $a(E_{tot}^{Acc},\eta)$, $b(E_{tot}^{Acc},\eta)$ and $c(E_{tot}^{Acc},\eta)$ are parameters determined using Monte Carlo simulation as a function of the energy deposited in the accordion E_{tot}^{Acc} and $|\eta|$. The coefficients a and b are called offset and slope respectively. For the barrel pseudorapidity region ($|\eta| < 1.475$) the parametrisation is limited to the first two terms ($c = 0$).
- E_{ps}^{clLar} is the energy measured in the presampler corrected for the energy deposited in the passive material.
- X is the longitudinal barycentre of the shower (shower depth) defined as:

$$X = \frac{\sum_{i=0}^{3} E_i^{clLar} X_i}{\sum_{i=0}^{3} E_i^{clLar}}$$

  where: E_i^{clLar} are the energies deposited in the active medium of the presampler and the three calorimeter compartments and X_i is the depth of the longitudinal centre of each compartment as a function of $|\eta|$.

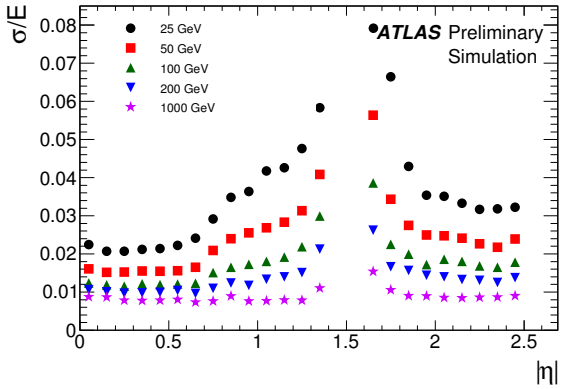

Figure 4.2: Expected fractional energy resolution of the EM calorimeter for electrons of different energies as a function of pseudorapidity [50].

- $s_{cl}^{Acc}(X,\eta)$ is a correction factor to account for the accordion sampling fraction.
- $f_{out}(X,\eta)$ is the correction for the energy deposited in the calorimeter outside the cluster (lateral leakage).
- $f_{leak}(X,\eta)$ is the longitudinal leakage correction.
- $F(\eta,\varphi)$ is the energy correction depending on the impact point inside a cell (energy modulation).

In the region $|\eta| > 1.8$ where the presampler is not present, the energy deposited in front of the calorimeter is parametrised as a function of the longitudinal shower barycentre computed with the information given by the compartments only [49]. Fig. 4.2 shows the expected energy resolution of electrons for a wide energy range. It has a maximum value close to the transition region.

4.4 In-situ Electron Calibration

The $Z \to ee$ decays and the well-known Z mass are used to further establish the electron energy scale and intercalibrate the different detector regions. In each calorimetric region i, the energy of the electron is parametrised as:

$$E^{meas} = E^{true}(1+\alpha_i)$$

where E^{true} is the true electron energy, E^{meas} the energy measured by the calorimeter after simulation based energy-scale correction, and α_i the residual miscalibration determined by a log-likelihood fit constraining the dilepton mass to the Z boson lineshape. The results obtained using the 2010 data are shown in Fig. 4.3.

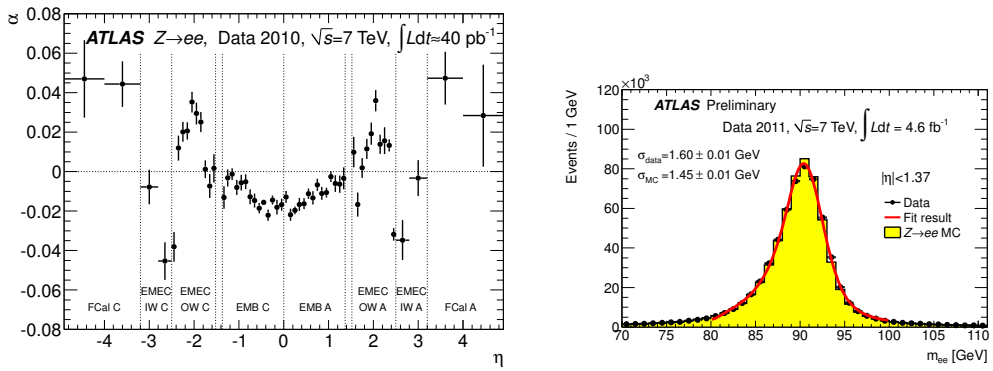

Figure 4.3: *Left*: The energy-scale correction factor α as a function of the pseudorapidity of the electron cluster derived from fits to $Z \to ee$ data [51]. *Right*: Reconstructed di-electron mass distributions for $Z \to ee$ decays when both electrons are in the barrel region after applying the baseline 2011 $Z \to ee$ calibration. The data are compared to the signal Monte Carlo expectation. The fits of a Breit-Wigner convolved with a Crystal Ball function are shown. The Gaussian width of the Crystal Ball function is given both for data and MC simulation [47].

4.5 Electron Identification

At LHC, the electron to jet ratio is expected to be $\sim 10^{-5}$, almost two orders of magnitude smaller than at TeVatron. It is thus essential to be able to identify signal isolated electrons while having a high rejection against jets and non-isolated electrons. For that purpose a number of identification cuts including calorimeter, tracking and cluster-track matching information are used. There are three reference sets of cuts defined in a p_T and η grid with increasing background rejection factors: "loose++", "medium++" and "tight++".

The **"loose++" identification** criterion has a lower background rejection and a higher signal efficiency than the other criteria. The cuts used in this case are mainly calorimetric cuts on the shower width and on the fraction of the energy leakage into the hadronic calorimeter. A few track quality cuts are also applied (see Table 4.1).

The **"medium++" identification** provides a higher background rejection compared to loose++. In addition to the loose++ requirements, medium++ includes cuts on variables defined in the first layer of the EM calorimeter, on track quality and on the hit multiplicity in the b-layer.

The **"tight++" identification** includes additional and more stringent requirements. It is used to provide a high background rejection. In particular, tight++ also includes a more stringent cluster-track matching in φ and TRT cuts [48].

Table 4.1 shows the cuts used for each level of electron identification. Fig. 4.4 and 4.5 show the medium the tight identification efficiencies as a function of the electron E_T and η respectively [1].

[1] 1The figure shows the results for the 2010 data since official ATLAS plots are not yet released. In this analysis, the updated identification values derived using the 2011 data are used.

Type	Description	Variable name
Loose++ cuts		
Acceptance of the detector	$\|\eta\| < 2.47$	
Hadronic leakage	Ratio of E_T in the first layer of the hadronic calorimeter to E_T of the EM cluster (used over the range $\|\eta\| < 0.8$ and $\|\eta\| > 1.37$)	R_{had1}
	Ratio of E_T in the hadronic calorimeter to E_T of the EM cluster (used over the range $\|\eta\| > 0.8$ and $\|\eta\| < 1.37$)	R_{had}
First layer of EM calorimeter	Total shower width	w_{stot}
Second layer of EM calorimeter	Ratio in η of cell energies in 3×7 versus 7×7 cells	R_η
	Lateral width of the shower	$w_{\eta 2}$
Track quality	Number of hits in the pixel detector (≥ 1)	N_{pix}
	Number of hits in the pixels and SCT (≥ 7)	N_{Si}
	$\Delta\eta$ between the cluster and the track (< 0.015)	$\Delta\eta_1$
Medium++ cuts (includes loose++ cuts)		
First layer of EM calorimeter	Ratio of energy difference associated with the largest and second largest energy deposit over the sum of these energies	ΔE_s
	Fraction of energy in 1st sampling	F_1
b-layer	Number of hits in the b-layer (≥ 1)	N_{blayer}
Track quality	Tighter $\Delta\eta$ between the cluster and the track (< 0.005)	$\Delta\eta_1$
	Transverse impact parameter (< 5 mm)	d_0
TRT	Ratio of the number of high-threshold hits to the total number of hits in the TRT	R_{TRT}
Tight++ cuts (includes medium++ cuts)		
Track quality	$\Delta\varphi$ between the cluster and the track	$\Delta\varphi_2$
	Ratio of the cluster energy to the track momentum	E/p
	Tighter transverse impact parameter (< 1 mm)	d_0
TRT	Total number of hits in the TRT	N_{TRT}

Table 4.1: Definition of the variables used for loose++, medium++ and tight++ electron identification cuts for the region $|\eta| < 2.47$ [48].

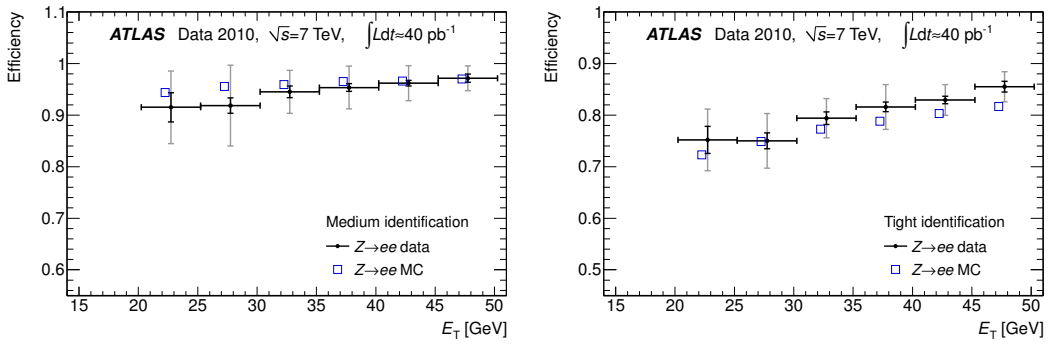

Figure 4.4: Efficiencies measured from $Z \to ee$ events and predicted by MC for the medium identification criteria *Left:* as a function of E_T (integrated over $|\eta| < 2.47$ excluding the transition region $1.37 < |\eta| < 1.52$) *Right:* as a function of η (integrated over $20 < E_T < 50$ GeV). The results for the data are shown with their statistical (inner error bars) and total (outer error bars) uncertainties. The statistical error on the MC efficiencies plotted as open squares is negligible. For clarity, the data and MC points are slightly displaced horizontally in opposite directions [51].

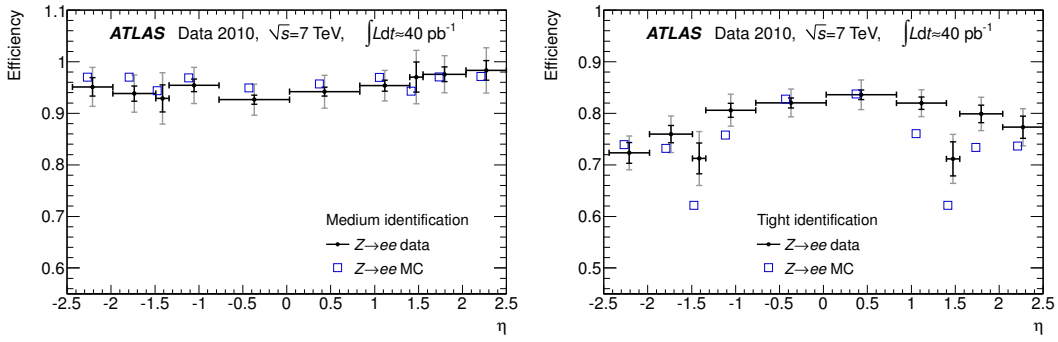

Figure 4.5: Efficiencies measured from $Z \to ee$ events and predicted by MC for the tight identification criteria as a function of E_T (integrated over $|\eta| < 2.47$ excluding the transition region $1.37 < |\eta| < 1.52$) (*left*) and of η (integrated over $20 < E_T < 50$ GeV) (*right*). Compared to the medium efficiencies, the efficiencies for tight electrons are lower. [51].

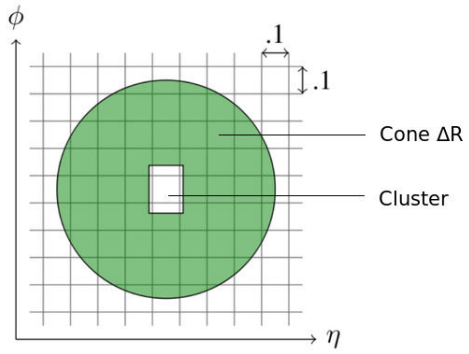

Figure 4.6: Schematic representation of the cone definition used for calorimetric isolation.

4.6 Electron Isolation

Many physics analyses and in particular W and Z decays produce a final state with isolated leptons. In this analysis, the background contamination can be reduced by applying isolation criteria on the candidate lepton. Isolation variables are defined using calorimetric information only or quantities computed using tracking detectors only. For the *calorimetric isolation* (Fig. 4.6), a cone of a given size ΔR is formed around the electron cluster axis (typically $\Delta R = 0.2$, 0.3 or 0.4). If the energy deposited in this cone (after the subtraction of the energy of the electron cluster) is below a given threshold, the electron is considered to be isolated. Calorimeter isolation variables are called E_T^{cone20}, E_T^{cone30}, E_T^{cone40} depending on the values of ΔR.

The *track isolation* variable is computed by summing the magnitudes of transverse momenta of all additional tracks inside a cone of size ΔR (typically 0.2, 0.3, 0.4) around the electron track. The calorimetric isolation variable is corrected for the energy deposited by the particles belonging to the underlying event. In addition, corrections for pile-up and E_T leakage outside the cluster are applied to evaluate the calorimetric isolation variable. The track isolation variable is computed by using only tracks that originate from the same vertex as the electron. Therefore it does not have a strong dependence on pile-up and on underlying event and is not corrected for such effects.

4.7 Charge Identification

4.7.1 Method and Analysis Selection

The charge assigned to an electron* [2] is defined from the curvature of its track. A mis-measurement of the charge can happen when a cluster produced in the EM calorimeter by an electron* is associated with a wrong track. For example this can happen if an electron interacts by bremsstrahlung early in the detector and the resulting photon converts into an electron-positrons pair. In this case,

[2]The star indicates when the term "electron*" is used as "electron or positron" candidate.

a mis-measurement of the charge happens if the cluster is associated with the track of the positron of the pair.

The charge identification rate represents how often an electron* is assigned the correct charge and is defined as the number of correctly assigned charges over all assignments $\varepsilon_{id} = \frac{N_{correct\ charge}}{N_{all}}$. In an equivalent way the charge misidentification rate represents how often an electron* is assigned the wrong charge and is defined as $\varepsilon_{misid} = \frac{N_{wrong\ charge}}{N_{all}}$.

For many studies, in particular for the measurement of the W^+ and W^- cross-sections, it is important to know how often an electron* is assigned the wrong charge. It has been found out that in most cases this is related to the electron* interacting before entering the calorimeter. Therefore the charge (mis)identification depends on the material in front of the EM calorimeter. For very high p_T electrons* the charge (mis)identification is mostly due to the fact that the tracks of high p_T particles have little curvature making it hard to measure the curvature and therefore to assign a charge.

In practice, the charge (mis)identification rate depends on the level of the electron* identification. This is due to the fact that electrons* satisfying more stringent track-cluster matching identification criteria are those that have suffered less of the interactions with detector material. Therefore in this study the measurement is performed at four different levels of electron identification namely: at "track quality" level for electron* candidates satisfying a number of pixel and silicon hits in the inner detector, at loose++, medium++ and tight++ level. Since the ATLAS analyses use those four identification criteria, it is important to measure the charge (mis)identification rate in all cases.

For this measurement the Tag&Probe method is used on $Z \to ee$ events. This method consists in selecting a very well reconstructed electron* candidate (tag electron*) and then looking if its partner has the correct charge assignment. The event selection criteria for this analysis require at least one vertex with at least three tracks reconstructed in the event and that an unprescaled single electron trigger is passed. Events with badly reconstructed jets are rejected and an E_T^{miss} cut (MET_RefFinal < 20 GeV) is used to remove electroweak background (in particular $W \to e\nu$ events). The tag electron* is required:

- to have p_T above 25 GeV,
- to satisfy tight++ identification level,
- to have triggered the event,
- to be isolated ($E_T^{cone30}/E_T < 0.15$) and
- to be in the barrel region in order to reduce the charge misidentification of the tag ($|\eta| < 1.37$).

The probe electron* is required:

- to have p_T above 25 GeV and $|\eta|$ below 2.47,
- to be outside the transition region $[1.37, 1.52]$ between the barrel and the end cap calorimeter and
- to satisfy a given identification level.

As will be explained later, the signal region for the Tag&Probe measurement is defined as $|M_{tag\&probe} - M_Z| < 10$ GeV, where $|M_{tag\&probe}|$ indicates the invariant mass computed using the tag and probe electron* and $M_Z = 91.19$ GeV

To reduce bias, all possible combinations of electron pairs in an event are taken into account. For a given charge of the tag, the same (SS) or opposite charge (OS) of the probe is looked at, as explained in the following. In this analysis, it is assumed that the charge of the tag electron* is correctly assigned since the criteria used to select the tag are very stringent. A small correction is applied in the analysis to account for the fact that the charge identification rate of the tag is not exactly 1.

There are two measurements performed: the charge identification rate and the charge misidentification rate. The former uses the OS sample, the latter relies upon the SS sample. Since the level of the background contamination differs in these two samples, both measurements will be performed independently. This will allow to cross-check possible bias induced from the background subtraction procedure. The measurement is performed for both electrons and positrons.

The **charge identification** rate is measured as the number of opposite sign pairs over all pairs $\varepsilon_{id} = \frac{Opposite\ Sign\ Pairs\ (OS)}{All}$ or more explicitly the probability of an electron being reconstructed as an electron is [3]:

$$\varepsilon_{id}^{-} = \frac{+_{tag} -_{probe}}{+_{tag} -_{probe} \,\&\, +_{tag} +_{probe}}$$

The **charge misidentification** is measured as the number of same sign pairs over all pairs $\varepsilon_{misid} = \frac{Same\ Sign\ Pairs\ (SS)}{All}$. The probability of an electron being reconstructed as a positron can be expressed as:

$$\varepsilon_{misid}^{-} = \frac{+_{tag} +_{probe}}{+_{tag} -_{probe} \,\&\, +_{tag} +_{probe}}$$

Similar relations hold for the charge identification (ε_{id}^{+}) and the charge misidentification (ε_{misid}^{+}) of positrons.

The results of these two methods may be different since they may depend on the level of background, if the background subtraction is not done properly. In this measurement the most prominent background is due to interactions where jets faking electrons are produced (QCD background). Therefore if the QCD background subtraction is done properly then the obtained results

[3] The symbol "&" indicates here a sum.

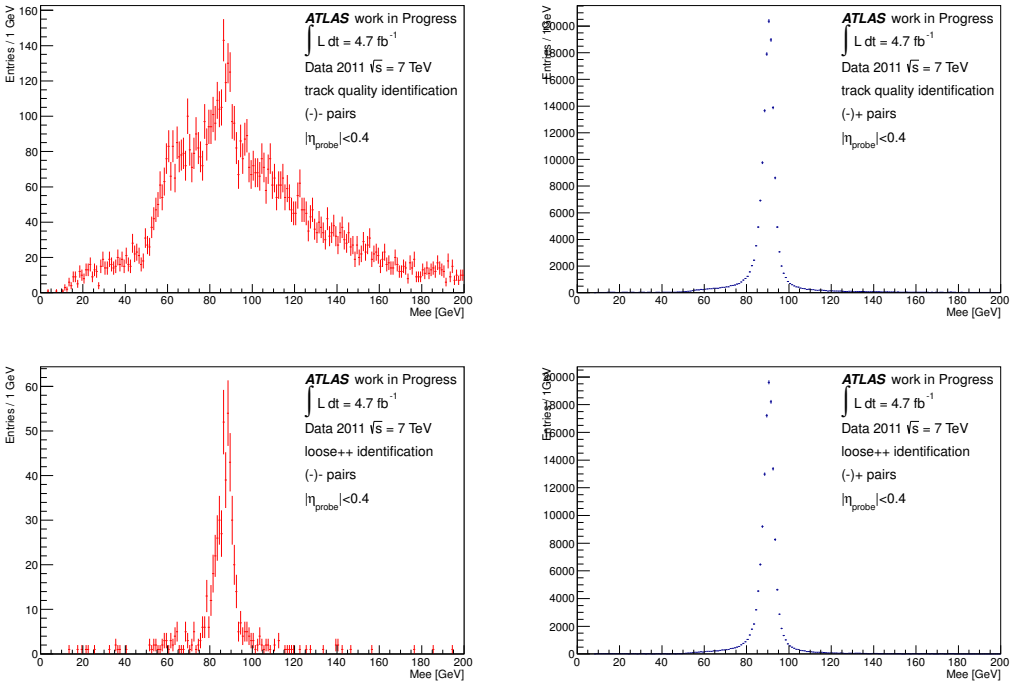

Figure 4.7: *Top row:* The distribution of the tag-probe mass for probe electrons* passing track quality identification level with $|\eta_{probe}| < 0.4$ is shown in the case of SS pairs (tag electron, probe electron) in the left plot and for OS pairs (tag electron, probe positron) in the right plot; *Bottom row:* Same distributions for the case where the probe electron* satisfies the loose++ identification requirements. The "shoulder" seen at around 60 GeV is due to the lepton kinematic cuts.

are expected to agree.

4.7.2 QCD Background Evaluation

In Fig. 4.7 and 4.8 the tag-probe mass distribution is shown for the four different identification levels of the probe electron*. It has been verified that in the first two cases (track quality and loose++) it is necessary to subtract the QCD background in order to extract the number of signal events. On the contrary the medium++ and tight++ probe identification requirements on the probe electron* give a very clean signal ($\ll 0.5\%$) as shown in Fig. 4.8. For this reason, a different approach will be followed to measure the charge (mis)identification depending on the identification level of the probe electron*.

To evaluate the number of signal events when the probe electrons* satisfy the track quality or loose++ criteria, a fit to the tag-probe mass distribution with a template method is used. In this case, the tag-probe mass distribution in data is fit to a weighted sum of the Monte Carlo signal ($Z \to ee$) distribution plus the QCD background distribution obtained with a data-driven method. The weights are the parameters of the fit. A fit with an analytical form was also tried but due to the high p_T lepton cuts (25 GeV), there was not enough level arm to obtain a satisfactory result.

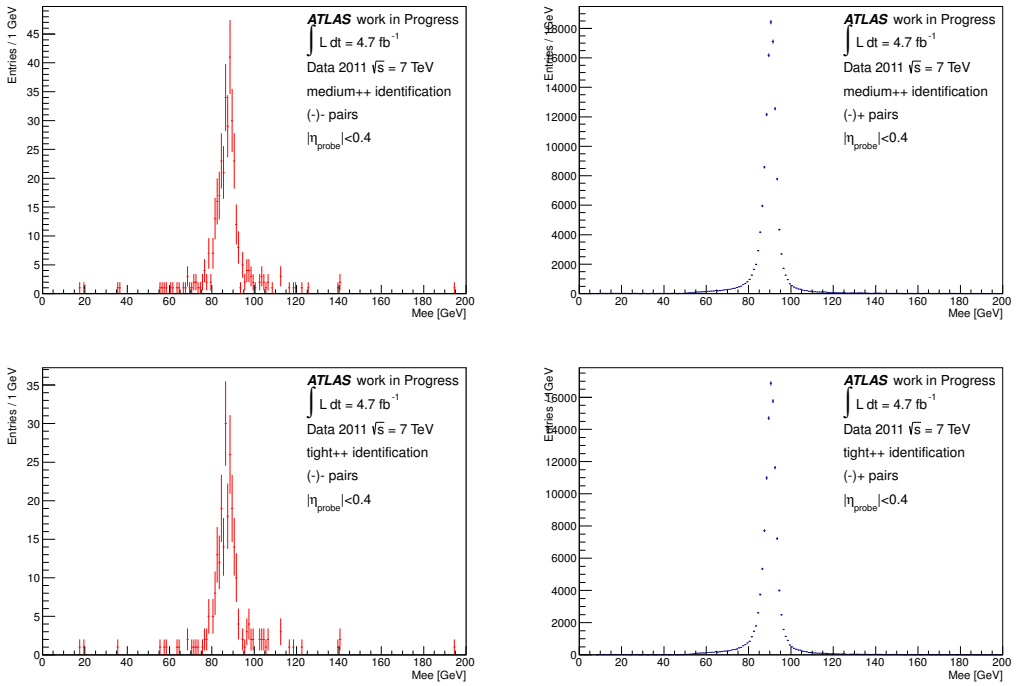

Figure 4.8: *Top row:* The tag-probe mass distribution for probe electrons* passing the medium++ identification level with $|\eta_{probe}| < 0.4$ is shown for SS pairs (tag electron, probe electron) in the left plot and for OS pairs (tag electron, probe positron) in the right plot; *Bottom row:* Same distributions for probe electrons* satisfying the tight++ identification requirements. The shoulder seen at ~ 60 GeV is caused by the kinematic cuts applied on the electron* selection.

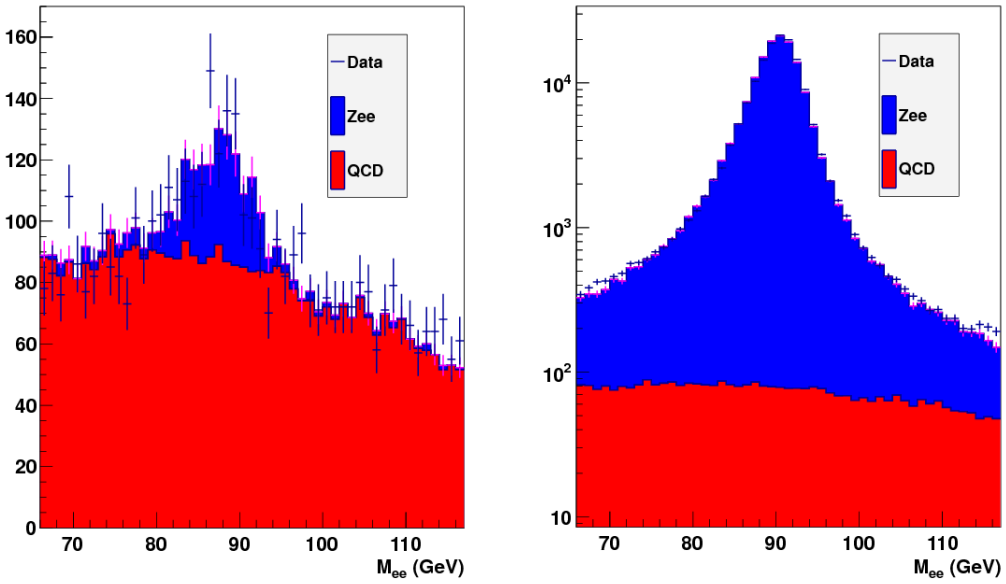

Figure 4.9: *Left plot:* Template fit results on the tag-probe mass distribution using $Z \to ee$ Monte Carlo and a data-driven QCD sample for SS pairs (tag electron, probe electron) for probes satisfying the track quality requirements and $|\eta_{probe}| < 0.4$. Dots represent the data points. The histograms are normalised to the fit results; *Right plot:* Same distribution for OS pairs (tag electron, probe positron).

The sample to extract the shape of the tag-probe mass distribution for the QCD background is taken from data using the exact same cuts as for the Tag&Probe selection with the difference that in this case the identification level of the electrons* is different: the tag is required to pass the medium identification (looser selection than the medium++) criteria and the probe is required to fail the loose identification (looser selection compared to the loose++).

In Fig. 4.9 the QCD and the signal Monte Carlo ($Z \to ee$) templates are shown in comparison to the data.

4.7.3 Charge (Mis)Identification Results

As mentioned above when the probe satisfies the track quality or loose++ identification criteria, the QCD background is subtracted using a template fit method in order to extract the number of signal events. The template fit is performed on the tag-probe mass distribution in the region $66 < M_{ee} < 116$ GeV and then the number of signal events in a narrower region $[80, 101]$ GeV is counted. A restricted region has been used since at the edge of the fit region the templates do not describe perfectly well the data.

If the probe electron* satisfies the medium++ or tight++ identification, no QCD background subtraction is performed since in this case the signal is very clean ($\ll 0.5\%$). Therefore, the number of events in the M_{ee} region $[80, 101]$ GeV is counted and used for further analysis.

Finally in order to compare the charge (mis)identification rate in data and in simulation, the same analysis is performed on signal Monte Carlo ($Z \to ee$). In this case, an additional constraint is applied to the tag and probe candidates to ensure that they are matched to an electron/positron (or photon) coming either directly or indirectly from the Z boson. A background subtraction is no longer needed in this case and the number of events in the region $80 < M_{ee} < 101$ GeV is simply counted. Two matching methods between reconstructed candidates and generated particles are used: a track based [4] and a cone based (with $\Delta R < 0.15$) algorithm. The difference between the results obtained with the two methods is below $3‰$.

For the evaluation of the systematic uncertainties on the (mis)identification efficiencies four different effects were studied:

- tighten the p_T of the tag from 25 GeV to 30 GeV,
- remove the cut applied on the E_T^{miss} (this increases the number of background events),
- relax the isolation of the tag electron to $E_T^{cone30}/E_T < 0.3$ (this also increases the number of background events) and
- change the M_{ee} region for the signal extraction to $[76, 101]$ GeV.

Track quality level results

The results for the case of "track quality" probes are presented here. The track quality criteria require that the probe has at least one hit in the pixel detector and at least seven hits in the silicon detectors. In Fig. 4.10 the comparison between charge (mis)identification in data for electrons and positrons is displayed [5]. In the barrel region the charge misidentification is quite low while it increases in the end-cap as a function of η. This is due to the fact that there is more material in this region making it more probable for electrons* to interact before reaching the calorimeter and being associated with the wrong track. It is important also to notice that no significant difference is observed between the results for electrons and positrons leading to the conclusion that the fraction of electrons wrongly identified as positrons in data is the same as the number of positrons wrongly identified as electrons ($\varepsilon^+ = \varepsilon^-$).

In Fig. 4.11 the comparison between the data (obtained with the template fit method) and the Monte Carlo results is shown. The agreement is quite good in the barrel region while in the end-cap region a discrepancy is observed. In the last η bin the difference between data and Monte Carlo is $\sim 3-4\%$ with the second showing higher charge misidentification rate. This effect could be due to higher amount of material in Monte Carlo than in data at high η. An indication that this explanation is pertinent is shown later in Fig. 4.21. One more point to mention is that even

[4] http://alxr.usatlas.bnl.gov/lxr-stb6/source/atlas/PhysicsAnalysis/MCTruthClassifier/MCTruthClassifier/MCTruthClassifierDefs.h

[5] Here "electrons" and "positrons" refers to electrons and positrons with correctly identified charge since the tag is selection with very stringent criteria (see Section 4.7.1.

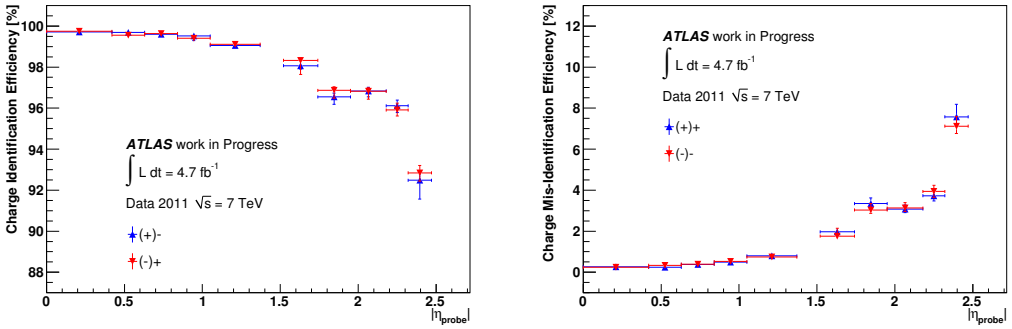

Figure 4.10: *Left plot:* Comparison between charge identification for (probe) electrons *(blue)* and (probe) positrons *(red)* passing the track quality requirements; *Right plot:* Charge misidentification for electrons and positrons at track quality level.

though there is no difference observed between the electron and positron charge (mis)identification in data, the Monte Carlo shows higher identification for positrons at high η. The maximum difference is in the last η bin amounts to $\sim 2\sigma$. This difference has not been investigated here and should be taken into account in charge related analyses if (mis)identification rates measured in Monte Carlo simulation are used.

Fig. 4.12 displays the comparison between the two methods: charge identification and charge misidentification for electrons (left plot) and for positrons (right plot) [6]. There is no significant difference observed between the two methods meaning that there is no bias introduced by the QCD background subtraction method. In principle, this comparison represents an additional way to control the systematic uncertainty on the background evaluation.

Loose++ identification

In this section the results for the charge (mis)identification in data for electrons and positrons passing the loose++ requirements are presented. Fig. 4.13 shows the agreement between the results obtained for electrons and positrons.

The data - Monte Carlo comparison for charge identification and misidentification is shown in Fig. 4.14. As in the previous case, a small discrepancy is observed at high $|\eta|$.

The comparison between the methods of charge identification and charge misidentification are shown in Fig. 4.15. The second plot shows the same results for positrons. The two methods give, as in the previous case (see Fig. 4.12) compatible results.

[6] Here "electrons" and "positrons" refers to electrons and positrons with correctly identified charge since the tag is selection with very stringent criteria (see Section 4.7.1.

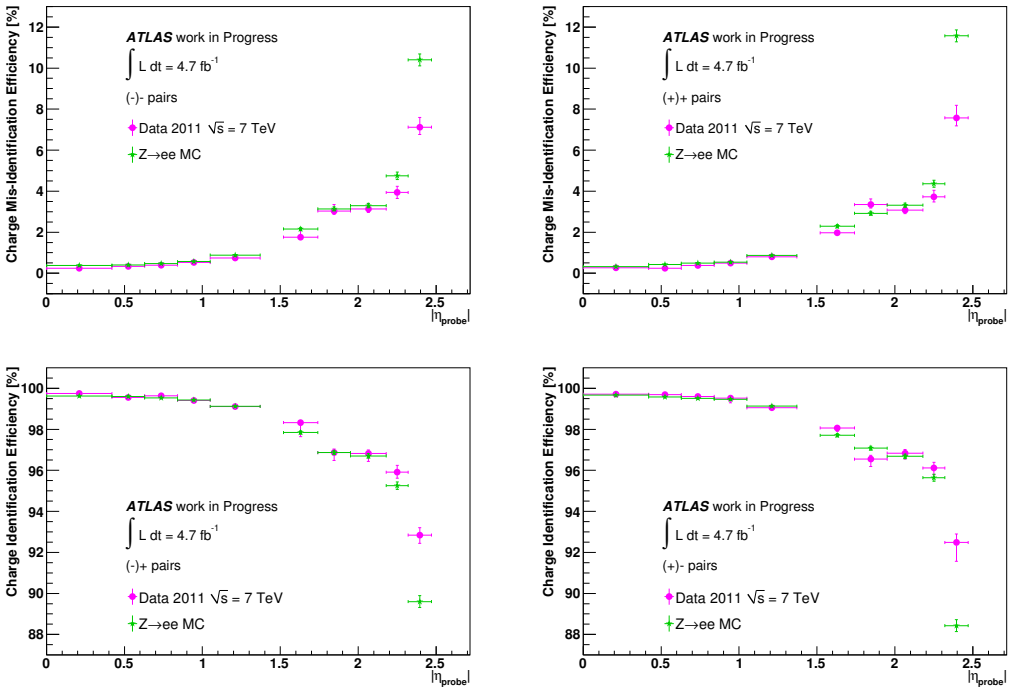

Figure 4.11: Plots showing the data - Monte Carlo comparison at track quality level for (a) charge misidentification using (-)- pairs [the brackets indicate the sign of the tag]; (b) charge misidentification using (+)+ pairs; (c) charge identification using (-)+ pairs; (d) charge identification using (+)- pairs.

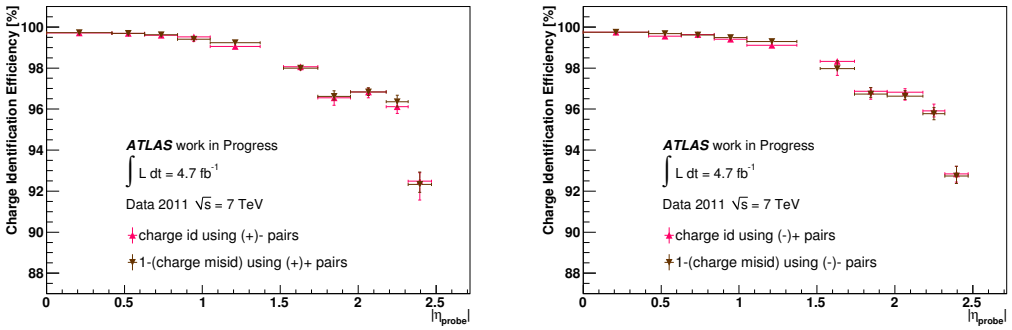

Figure 4.12: *Left plot:* Comparison between charge identification and charge misidentification for electrons satisfying the track quality requirements (on the graph the values 1-(charge misidentification) are plotted); *Right plot:* Comparison between charge identification and charge misidentification for track quality positrons.

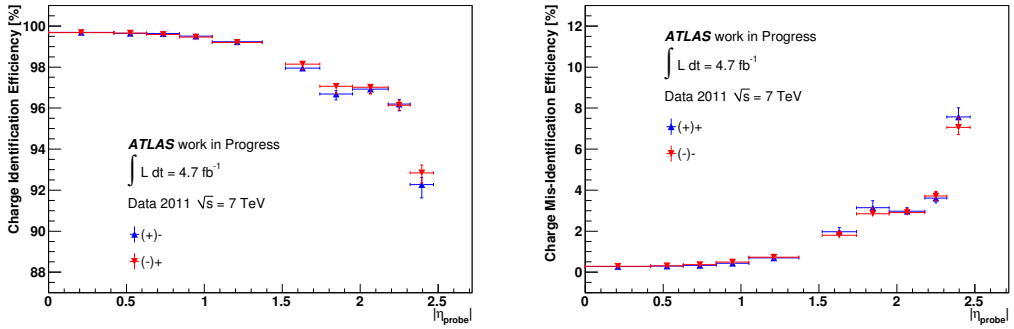

Figure 4.13: *Left plot:* Comparison between charge identification (OS measurement) for electrons (blue) and positrons (red) passing the loose++ identification; *Right plot:* Charge misidentification (SS measurement) for electrons and positrons at loose++ level.

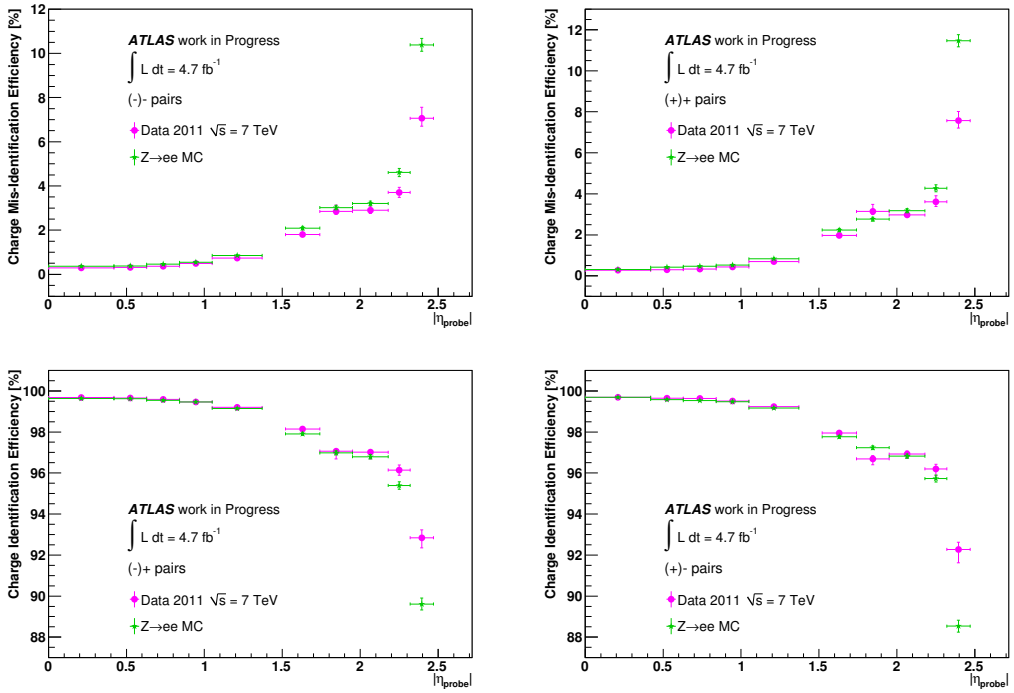

Figure 4.14: Plots showing the data - Monte Carlo comparison at loose++ level for (a) charge misidentification using (-)- pairs [the brackets indicate the sign of the tag]; (b) charge misidentification using (+)+ pairs; (c) charge identification using (-)+ pairs; (d) charge identification using (+)- pairs.

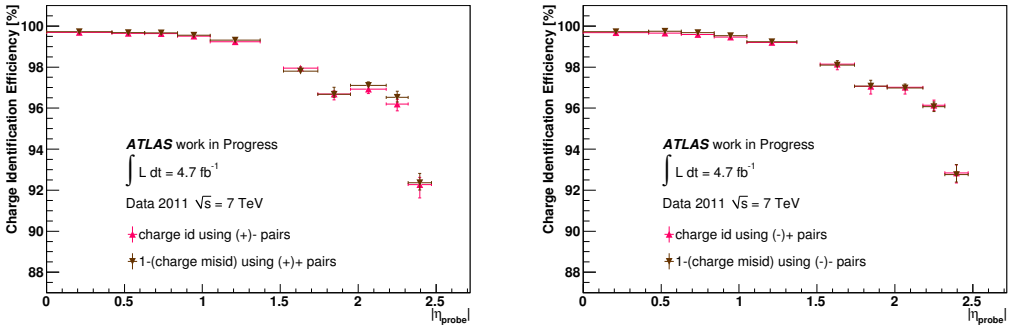

Figure 4.15: *Left plot:* Comparison between charge identification and charge misidentification for loose++ electrons (on the plot the values 1-(charge misidentification) are plotted; *Right plot:* Comparison between charge identification and charge misidentification for loose++ positrons.

Medium++ identification

Fig. 4.16 displays the comparison between electron and positron charge (mis)identification at medium++ identification level. Only the charge identification rate is shown in Fig. 4.16 since no background subtraction is performed and therefore the charge identification measurement is fully correlated with the charge misidentification one. As expected, the rate of correctly identified charges is higher compared to the loose++ level especially in the end-cap region. As before the charge identification rate in data for electrons is the same as for positrons.

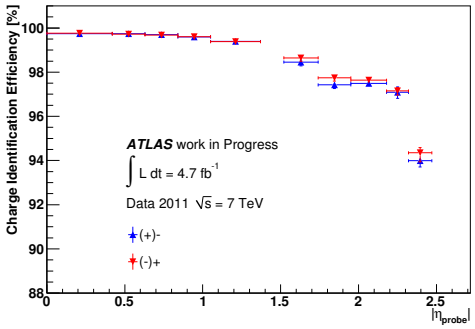

Figure 4.16: Comparison between charge identification rates for electrons (blue) and positrons (red) passing the medium++ identification.

In Fig. 4.17 the data and Monte Carlo comparison for electrons and positrons charge identification satisfying the medium++ identification requirements is shown. In Monte Carlo the agreement between the charge identification rate for electrons and positrons is within 1σ.

The trigger used for many analyses is a single electron trigger where the electron needs to satisfy medium++ identification criteria. For analyses where the charge misidentification plays an important role, it is necessary to know whether the trigger requirement affects the charge identifi-

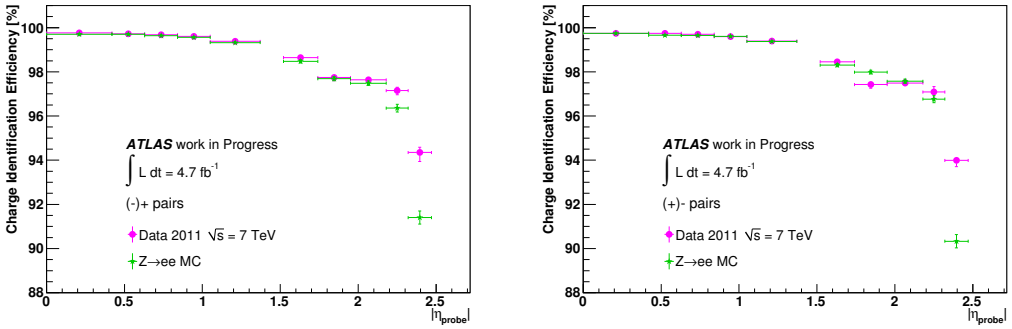

Figure 4.17: Plots showing the data - Monte Carlo comparison at medium++ level for (a) charge identification using (-)+ pairs [the brackets indicate the sign of the tag]; (b) charge identification using (+)- pairs.

cation. Therefore, for the cases of medium++ and tight++ probes we add an additional requirement to the probe namely the requirement that the probe is matched to the object that fired the single electron medium++ trigger. The results showing the comparison between medium++ probes and medium++ probes that triggered the event are presented in Fig. 4.18. For the case of triggered matched probes the charge identification is slightly higher in the end-cap region. The difference is at the level of $\sim 1\%$ for the last η bin (corresponds to $\sim 1.5\sigma$). This effect indicates a small correlation between the charge identification and the quality of the triggered object.

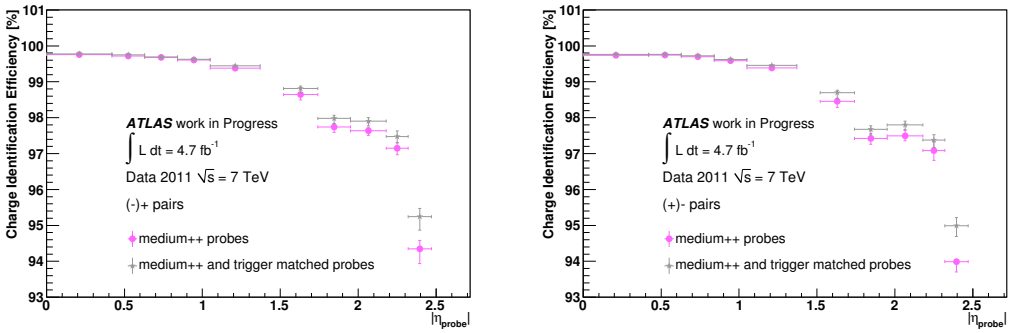

Figure 4.18: Comparison between medium++ probes and medium++ probes that have triggered the event (a) charge identification using (-)+ pairs [the brackets indicate the sign of the tag]; (b) charge identification using (+)- pairs.

Tight++ identification

In this section the charge identification rates for electrons and positrons satisfying the tight++ identification criteria are presented. Fig. 4.19 shows the agreement in data between the charge identification rates for electrons and positrons. As expected, at this level the charge identification is significantly higher compared to the previous identification levels. As in the previous case, the

charge identification is almost flat within the barrel region while it decreases in the end-cap region.

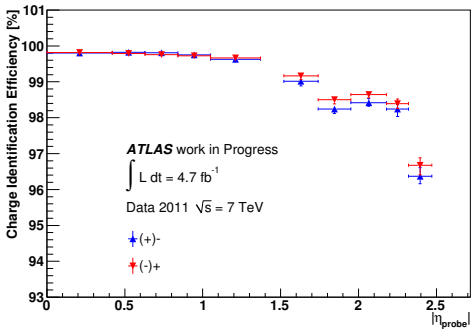

Figure 4.19: Comparison between charge identification for electrons (blue) and positrons (red) passing the tight++ identification.

In Fig. 4.20 the comparison between data and Monte Carlo charge identification rates are shown. Again a discrepancy is observed at high η. To investigate this discrepancy, the E/p distribution for data and Monte Carlo (where E is the energy of the electron cluster and p is the momentum of the track) is displayed in Fig. 4.21. This distribution is sensitive to the amount of material in front of the calorimeter. For the case of the last bin $2.32 < |\eta_{probe}| < 2.47$, the difference is larger. The fact that the Monte Carlo distribution is shifted to higher values indicates that there is more material upstream in the Monte Carlo description than on data.

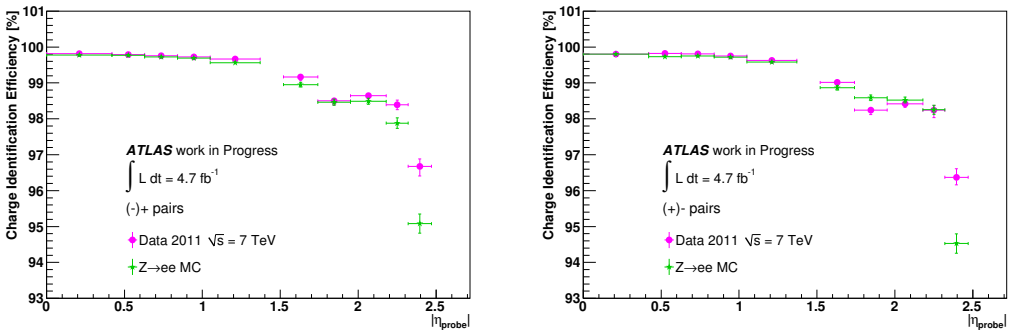

Figure 4.20: Plots showing the data - Monte Carlo comparison at tight++ level for (a) charge identification using (-)+ pairs [the brackets indicate the sign of the tag]; (b) charge identification using (+)- pairs.

The comparison between the charge identification for the tight++ level when the probe is required or not required to have triggered the event is displayed in Fig. 4.22. The difference is smaller than for the medium++ case but it still appears to be a trend for lower charge misidentification when the probe is required to be matched to the trigger.

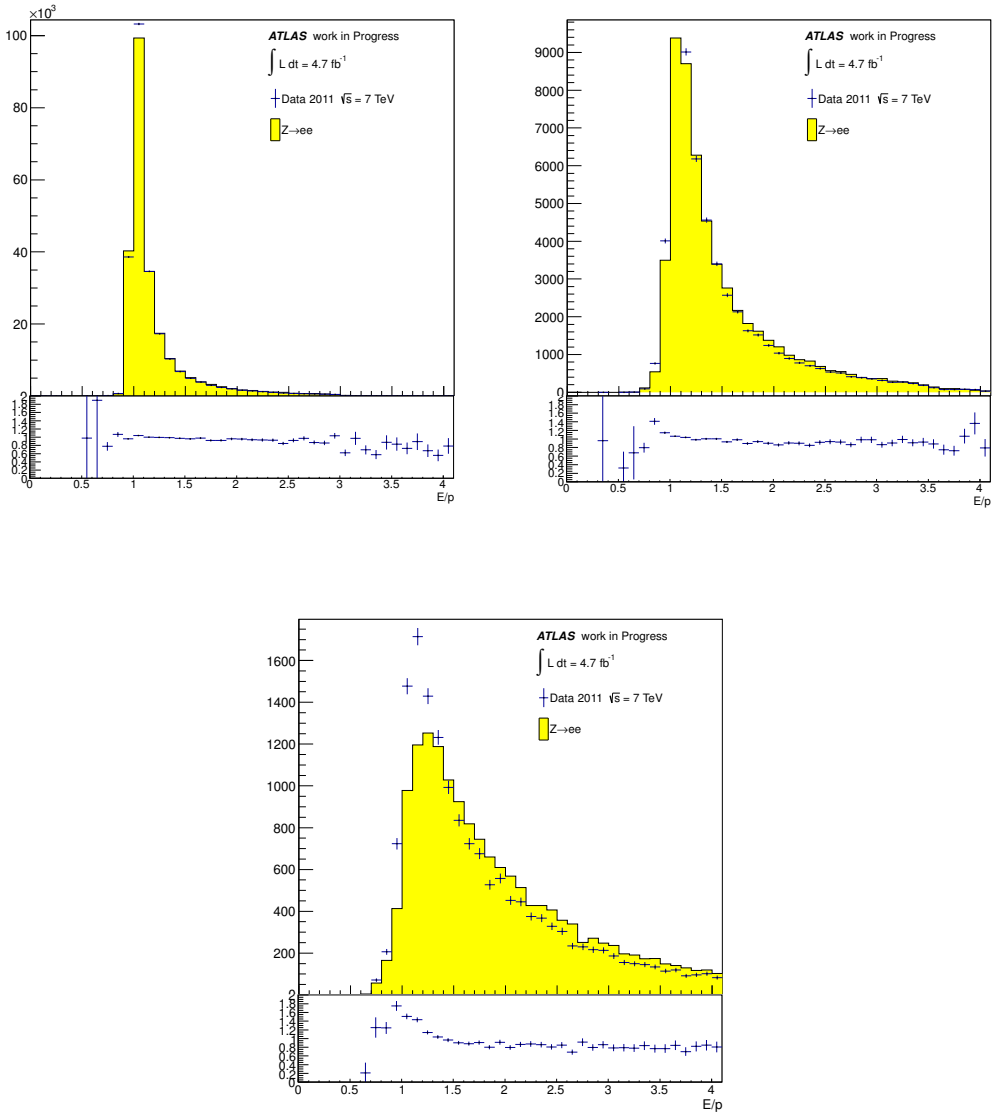

Figure 4.21: E/p distribution comparison between data and Monte Carlo for all tight++ probes in the pseudorapidity region (a) $|\eta_{probe}| < 0.42$ (b) $1.52 < |\eta_{probe}| < 1.74$ (first bin after crack) and (b) $2.32 < |\eta_{probe}| < 2.47$ (last η bin).

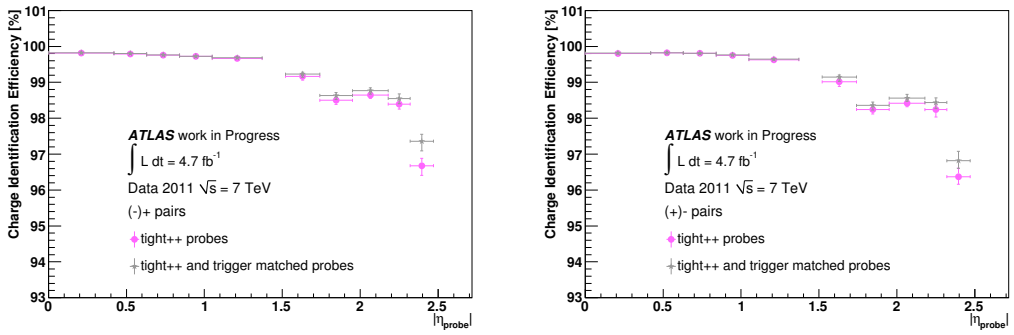

Figure 4.22: Comparison between tight++ probes and tight++ probes that have triggered the event (a) charge identification using (-)+ pairs [the brackets indicate the sign of the tag]; (b) charge identification using (+)- pairs.

4.8 E_T^{miss} Reconstruction

In ATLAS, several algorithms are used to compute the missing transverse energy, E_T^{miss}. Here the algorithm which is used in the W analysis is shortly described. In this case, the reconstruction and calibration of the E_T^{miss} variable makes use of a refined calibration based on reconstructed physics objects. This quantity is called E_T^{miss} RefFinal. The reconstruction includes contributions from the transverse energy deposits in the calorimeters and from the muons reconstructed in the muon spectrometer. The values of the E_T^{miss} and its azimuthal angle are calculated as:

$$E_T^{miss} = \sqrt{(E_x^{miss})^2 + (E_y^{miss})^2}\ ,\ \varphi_{miss} = \arctan(E_y^{miss}/E_x^{miss})$$

where:

$$E_{x(y)}^{miss} = E_{x(y)}^{miss,calo} + E_{x(y)}^{miss,\mu}. \tag{4.2}$$

4.8.1 Calculation and Calibration of the E_T^{miss} calorimeter term

The calorimeter terms $E_x^{miss,calo}$ and $E_y^{miss,calo}$ are defined as:

$$E_x^{miss,calo} = -\sum_{i=1}^{N_{cell}} E_i \sin\theta_i \cos\varphi_i\ ,\ E_y^{miss,calo} = -\sum_{i=1}^{N_{cell}} E_i \sin\theta_i \sin\varphi_i$$

where E_i, θ_i and φ_i are respectively the energy, polar angle and azimuthal angle of the cells over the pseudorapidity range $|\eta| < 4.5$.

In order to suppress the noise contribution, instead of using all cells only the cells that belong to topological clusters are used. These topological clusters are seeded by a cell with a deposited energy $|E_i| > 4\sigma_{noise}$. Then neighbouring cells with $|E_i| > 2\sigma_{noise}$ are added iteratively and finally all neighbours of the accumulated cells are added to build the topological cluster.

To account for effects from the detector response and inactive material in front of the calorimeter, a given calibration procedure is used. The calorimeter cells are calibrated on the basis of the reconstructed physics object to which they belong in the following order: electrons, photons, hadronically decaying τ, jets and muons (originating from energy lost by the muons in the calorimeter). Cells that belong to topological clusters but are not associated with any physics object are also taken into account. Once the cells are associated with a category of object as described above and calibrated accordingly, the contribution to the E_T^{miss} resulting from the transverse energy deposit in the calorimeter is calculated as:

$$E_{x(y)}^{miss,calo} = E_{x(y)}^{miss,e} + E_{x(y)}^{miss,\gamma} + E_{x(y)}^{miss,\tau} + E_{x(y)}^{miss,jets} + E_{x(y)}^{miss,softjets} + E_{x(y)}^{miss,calo,\mu} + E_{x(y)}^{miss,CellOut}$$

where each term is calculated as the negative sum of calibrated cell energies inside the corresponding objects. The different terms are listed below.

- $E_{x(y)}^{miss,e}$, $E_{x(y)}^{miss,\gamma}$ and $E_{x(y)}^{miss,\tau}$ are reconstructed from cells in electrons, photons and taus respectively. The electron contribution is calculated from reconstructed candidate electrons with $p_T > 10$ GeV satisfying the medium identification requirements and calibrated using the electron calibration. The contribution from photons is calculated from calibrated photons with $p_T > 10$ GeV satisfying tight photon identification requirements. The contribution from taus is calculated from "tight" taus with $p_T > 10$ GeV calibrated using a local hadronic calibration (LCW) which will be explained below.

- $E_{x(y)}^{miss,jets}$ is reconstructed from cells in jets with $p_T > 20$ GeV and calibrated with LCW first and then using the jet energy scale factor.

- $E_{x(y)}^{miss,softjets}$ is reconstructed from cells in jets with 7 GeV$< p_T < 20$ GeV and calibrated with LCW calibration.

- $E_{x(y)}^{miss,calo,\mu}$ is the contribution originating from the energy lost by muons in the calorimeter which will be discussed further in the E_T^{miss} muon term.

- $E_{x(y)}^{miss,CellOut}$ is calculated from the cells in topoclusters which are not included in the reconstructed objects. It is calibrated with LCW calibration and uses the reconstructed tracks to recover low p_T particles that do not reach the calorimeter.

With the addition of the muon term, the E_T^{miss} variable is computed [52].

4.8.2 Calculation of the E_T^{miss} muon term

The E_T^{miss} muon term is calculated from the momenta of muon candidate tracks within $|\eta| < 2.7$ as:

$$E_{x(y)}^{miss,\mu} = -\sum_{selected\ muons} p_{x(y)}^{\mu}$$

For muons in the region $2.5 < |\eta| < 2.7$ (outside the fiducial region of the inner detector), the p_T from the muon spectrometer is used. For the η region below 2.5, the p_T of the muon candidate is determined from the combined measurement of the inner detector and the muon spectrometer or from the measurement of the muon spectrometer only depending on whether the muon is isolated or not. Isolated and non-isolated muons are treated differently in order to avoid a double count of the muon contribution in the muon term and in the calorimetric muon term. Non-isolated muons are defined as those muons with a distance $\Delta R < 0.3$ from a jet.

More specifically, the p_T of an isolated muon is determined from the combined measurement of the inner detector and muon spectrometer. In this case, the energy lost by the muon in the calorimeter $E_{x(y)}^{miss,calo\mu}$ is not added to avoid double counting. For non-isolated muons, the energy lost in the calorimeter cannot be separated from the nearby jet energy. In this case and unless there is significant mismatch between the spectrometer and combined measurement, the p_T of the muon in the muon spectrometer after the energy loss in the calorimeter is used.

4.8.3 E_T^{miss} resolution

The E_T^{miss} performance is evaluated by studying the (E_x^{miss} , E_y^{miss}) resolutions as a function of the total transverse energy $\sum E_T$ reconstructed from the calorimeters defined as:

$$\sum E_T = \sum_{i=1}^{N_{cell}} E_i \sin\theta_i$$

where E_i and θ_i are the energy and polar angle respectively of cells associated with topological clusters within $|\eta| < 4.5$. This is evaluated in events with no real E_T^{miss} ($Z \to ll$) and on events with real E_T^{miss} ($W \to l\nu$). In Z events where no E_T^{miss} is expected, the resolution is estimated in data from the width of the two E_T^{miss} component distributions (E_x^{miss}; E_y^{miss}). In W events, the E_x^{miss} and E_y^{miss} resolutions are estimated from simulated events as the width of the distributions $E_x^{miss} - E_x^{miss,True}$ and $E_y^{miss} - E_y^{miss,True}$ respectively. The E_T^{miss} distribution and resolution are shown in Fig. 4.23 and 4.24 for $Z \to ee$ events (data) and $W \to e\nu$ events (simulation) respectively [52].

4.8.4 E_T^{miss} Linearity in $W \to e\nu$ Events

In this subsection, the work of the author of the thesis on the study of the E_T^{miss} linearity and resolution is presented. This study is used to understand the E_T^{miss} response in W analysis. The E_T^{miss} linearity curve is obtained calculating the variable

$$\frac{< E_T^{miss} - p_T^{\nu} >}{p_T^{\nu}} \tag{4.3}$$

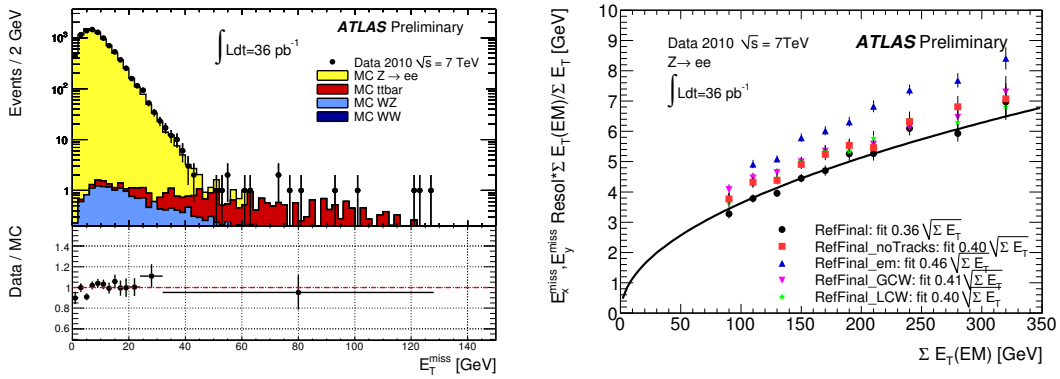

Figure 4.23: *Left plot:* distribution of E_T^{miss} as measured in a data sample of $Z \to ee$ candidates. The expectation from Monte Carlo simulation is superimposed and normalised to data, after each MC sample is weighted with its corresponding cross-section. The ratio of the data and the MC distribution is shown below the plot. *Right plot:* E_x^{miss} and E_y^{miss} resolution as a function of the total transverse energy in calorimeters for $Z \to ee$ events in data. The $\sum E_T$ is at the EM scale and E_x^{miss}, E_y^{miss} are scaled by the ratio $\sum E_T(EM)/\sum E_T$. Different calibration procedures of E_T^{miss} are compared. The curve is the fit to the resolution of RefFinal E_T^{miss}, and fit values are indicated for all E_T^{miss} calibration schemes used [52].

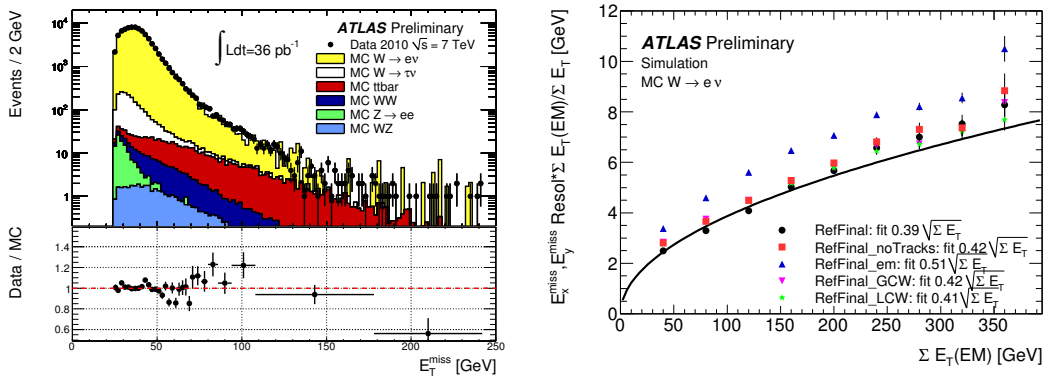

Figure 4.24: Same plot as Fig. 4.23 for W candidate events. *Left plot:* Distribution of E_T^{miss} as measured in a data sample of $W \to e/nu$ candidates. *Right plot:* E_x^{miss} and E_y^{miss} resolution as a function of the total transverse energy in calorimeters for $W \to e/nu$ events in data. Different calibrations of E_T^{miss} are compared. The curve is the fit to the resolution of RefFinal E_T^{miss}, and fit values are indicated for all E_T^{miss} calibration schemes used [52].

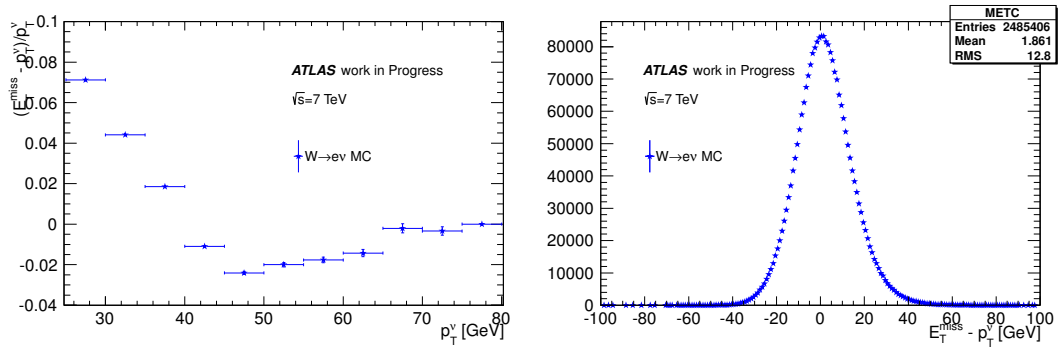

Figure 4.25: E_T^{miss} linearity and resolution as measured on simulated events. The Monte Carlo conditions correspond to the full 2011 data-taking. The selection includes only lepton requirements.

as a function of p_T^ν, where E_T^{miss} is the reconstructed missing transverse energy in Monte Carlo $W \to e\nu$ events and p_T^ν is the transverse momentum of the generated neutrino.

The selection requirements for this analysis include a high p_T and well reconstructed electron that satisfies the following criteria: p_T above 25 GeV and $|\eta| < 2.47$ excluding the calorimeter transition region. In addition, the electron is required to pass the tight++ identification criteria and to be isolated ($E_T^{cone30} < 5$ GeV).

The mean value of the linearity is expected to be zero if the reconstructed E_T^{miss} has the correct scale. In Fig. 4.25 the E_T^{miss} linearity curve is shown as a function of the p_T^ν value as obtained using Monte Carlo simulation corresponding to the 2011 data-taking conditions. A displacement from zero can be seen in the plot. The second plot shows the resolution distribution of the E_T^{miss} which is at the level of ~ 12 GeV when the same selection requirements are applied.

The E_T^{miss} reconstruction is highly affected by the pile-up conditions. This is shown in Fig. 4.26 where the E_T^{miss} linearity curve is shown for two periods with different pile-up conditions. The first plot simulates the data-taking conditions for the first 1.13 fb^{-1} of 2011 data-taking with low pile-up conditions (~ 5 interactions per bunch crossing in average) while the second plot shows the linearity of E_T^{miss} for high pile-up conditions (~ 12 interactions per bunch crossing in average) and corresponds to the conditions of the last 2.43 fb^{-1} of data-taking. For higher pile-up conditions the reconstructed E_T^{miss} has higher values.

Adding new requirements to the selection of the W events on the E_T^{miss} and the W transverse mass, as for all W physics analyses, changes significantly the E_T^{miss} linearity curve due to the high E_T^{miss} resolution. Fig. 4.27 shows the E_T^{miss} linearity and resolution when a E_T^{miss} requirement above 25 GeV and a W transverse mass requirement above 40 GeV are applied. The W transverse mass is defined as $m_T^W = \sqrt{2 \cdot p_T^l \cdot E_T^{miss} \cdot (1 - \cos(\varphi_{l,\nu}))}$ where $\varphi_{l,\nu}$ is the angle between the electron and the E_T^{miss} (neutrino) in the transverse plane.

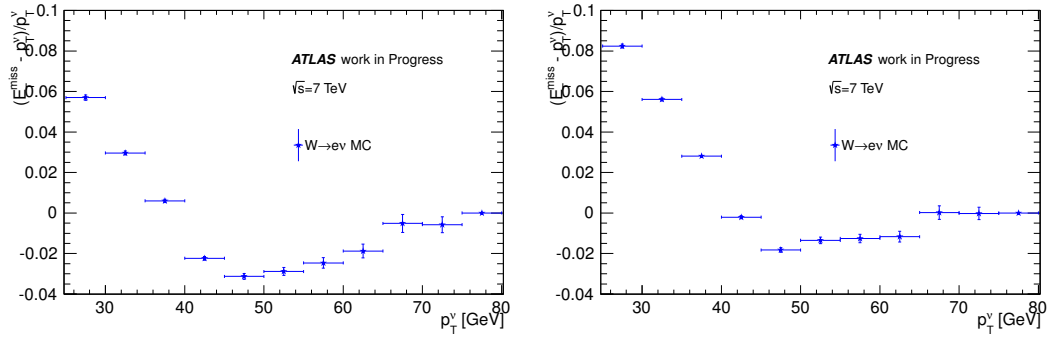

Figure 4.26: E_T^{miss} linearity as a function of p_T^{ν} measured on $W \to e\nu$ events. The left plot represents low pile-up conditions while the right plot high pile-up conditions. The linearity of E_T^{miss} is shifted to higher values for high pile-up conditions.

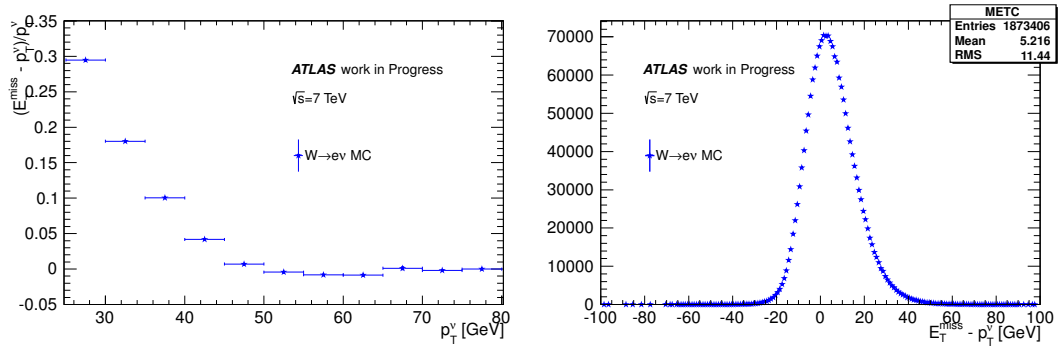

Figure 4.27: E_T^{miss} linearity (left) and resolution (right) after a selection including electron, E_T^{miss} and m_T^W requirements. Compared to Fig. 4.25 it is evident that the E_T^{miss} linearity is highly affected by the additional selection criteria. This is also seen in the right plot where the mean of the distribution is also shifted. The resolution of the E_T^{miss} is not significantly affected.

4.9 Conclusion

In summary, a coherent picture emerges from the analyses of the charge (mis)identification rates for electrons and positrons at different levels of identification criteria. The charge (mis)identification in data is the same for electrons and positrons. The data and the Monte Carlo results agree with the exception of very few bins at high η. This is probably due to a small misdescription of the detector material. As expected, the charge misidentification rate depends on the level of the electron identification and is lower for more stringent identification criteria.

Finally, a study of the E_T^{miss} linearity in $W \to e\nu$ events has also been presented showing its dependence on different pile-up conditions corresponding to the 2011 data-taking.

Chapter 5

W $\rightarrow$ eν Analysis

The reconstruction of $W \rightarrow e\nu$ decays relies on the detection of a high momentum electron and a large missing transverse energy. The main sources of background events to this process result from the production of the W, Z and $t\bar{t}$ pairs decaying in final states with at least one lepton and from events produced by the strong interactions between the initial protons which will be called "QCD events" in the following.

In this chapter, the selection criteria for $W \rightarrow e\nu$ events are described as well as the main sources of backgrounds to this process. The analysed data were collected by the ATLAS detector during the 2011 data-taking periods and correspond to a total integrated luminosity of 5.39 fb^{-1}.

5.1 Event Selection

A number of selection criteria are used to ensure a high signal efficiency and a low background contamination. In addition to the requirements of a high-p_T electron and a large missing transverse energy E_T^{miss}, several criteria must be satisfied in order to ensure the quality of the selected events. The full set of cuts is explained in the following subsections.

5.1.1 Event Preselection Requirements

The first step of the selection is to exclude events with major detector problems that could affect the measured quantities in the W analysis; for example events in which part of a subdetector was not operational. An analysis dependent Good Run List (GRL) is generated containing a list of events that can be safely used for the analysis. There are however events with sporadic noise bursts in the electromagnetic calorimeter or data corruption that are not accounted for in the GRL. These events are also excluded. This selection reduces by 3% the amount of data used. For the W and Z analyses, the selected sample corresponds to a luminosity of 4.71 fb^{-1}.

The data sample is selected by requiring that the single electron trigger is fired when run-

ning over a data stream gathering calorimeter based triggers ("EGamma stream"). Given that the instantaneous luminosity increased throughout the 2011 data-taking, the ATLAS trigger menu had to be modified to keep the event rate at a tolerable level. Therefore three different single electron triggers are used for this analysis depending on the data-taking period as shown on Table 5.1. They require an electron candidate of 20 (22) GeV that satisfy medium or medium1 identification requirements. The medium1 selection corresponds to the medium++ identification which is tighter than the medium identification requirements. During the second half of the data taking, an additional trigger (EF_e45_medium1) is also used to account for inefficiencies in very high E_T electrons. In this analysis, the effect of this trigger is insignificant. Fig. 5.1 shows the efficiency of the three main triggers which are used for this analysis.

Trigger	Luminosity $[fb^{-1}]$
EF_e20_medium	1.69
EF_e22_medium	0.59
EF_e22vh_medium1 OR EF_e45_medium1	2.43

Table 5.1: Triggers used for the $W \to e\nu$ analysis and the corresponding luminosity. The "vh" characters in the trigger name indicate that a requirement on the hadronic leakage was used to ensure a lower trigger rate while keeping a very high efficiency of the electron trigger.

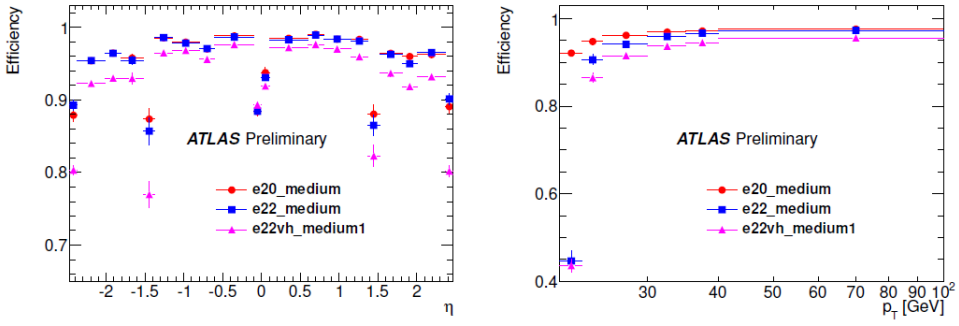

Figure 5.1: Efficiencies for the EF_e20_medium *circles*, EF_e22_medium *squares* and EF_e22vh_medium1 *triangles* triggers as a function of η_e and $p_{T,e}$ as measured on 2011 data. The error bars represent both statistical and systematic uncertainties [53].

Finally, the vertex having the largest scalar sum of transverse momenta of associated tracks is selected as the primary vertex of the hard collision. Only events where the primary vertex has at least three tracks associated are considered.

5.1.2 $W \to e\nu$ Selection

The requirements that the electron candidate and the E_T^{miss} in a given event need to satisfy in order to consider the event as a W candidate event are listed and motivated below.

The electron candidate is required to have p_T above 25 GeV. The p_T spectrum of the electron from a W decay is a jacobian peak centred around ~ 40 GeV (about half of the W mass). Cutting at $p_T > 25$ GeV has little impact on the signal while it reduces the background resulting from electroweak processes like the $W \to \tau\nu$ events and the QCD background that is expected to decrease monotonically with p_T. The electron candidate is also required to be in the pseudorapidity region $|\eta| < 2.47$ excluding the calorimeter transition region ($1.37 < |\eta| < 1.52$). The cuts described above define the "electron fiducial region". The transition region is excluded since the electron reconstruction is significantly lower in this region. In addition, the electron is required to be out of known small problematic calorimeter regions.

The electron candidate is further required:

- to have triggered the event,
- to satisfy the tight++ identification requirements (as mentioned in Section 4.5 the efficiency satisfying the tight++ criteria is $\sim 65\%$ while the background rejection is high $\sim O(10^{-4})$) and
- to satisfy a calorimetric isolation cut. The isolation variable used here, E_T^{cone30}, has been corrected for pile-up and E_T-leakage effects. Requiring that the candidate electron is isolated ($E_T^{cone30} < 5$ GeV) has little impact on the signal ($\sim 98\%$ efficiency) and at the same time rejects a large fraction of QCD background events ($\sim 65\%$ of the background).

It is worth noticing that it is not only required that the event passes one of the single electron triggers mentioned in Section 5.1.1 but also that the selected electron was the one that triggered the event. This requirement is applied in order to facilitate the use of trigger and identification corrections. To further reduce the background resulting mainly from $t\bar{t}$ and $Z \to ee$ processes, events that have a second electron in the electron fiducial region satisfying the medium++ identification requirement are rejected.

The E_T^{miss} is required to be larger than 25 GeV. This selection keeps $\sim 79\%$ of the signal events while it reduces the background contamination resulting from QCD and $Z \to ee$ processes. Furthermore, events that have badly reconstructed jets are excluded from the analysis since they affect the E_T^{miss} measurement (jet cleaning).

Finally, a cut on the transverse mass $m_T^W > 40$ GeV is applied. The transverse mass is defined as:

$$m_T^W = \sqrt{2 \cdot p_T^l \cdot E_T^{miss} \cdot (1 - \cos(\varphi_{l,\nu}))} \tag{5.1}$$

where $\varphi_{l,\nu}$ is the angle between the electron and the E_T^{miss} (neutrino) in the transverse plane.

The last row in Table 5.4 presents the number of data events as well as the expected number of $W \to e\nu$ signal and background events after all selection cuts described in this Section. In the following sections it will be explained how these results are obtained.

5.2 Electroweak Background Estimation

The signature of the $W \to e\nu$ decay can be reproduced by a number of other processes either because the final state is similar or because one or more particles are wrongly measured. Such processes constitute the background of the $W \to e\nu$ analysis. In this section we will describe the evaluation of the background events resulting from processes where decays mediated by electroweak processes are present ("electroweak background"). These are events with $W \to \tau\nu$, $Z \to ee$, $Z \to \tau\tau$, $t\bar{t}$ and with dibosons WW, WZ and ZZ. To study these backgrounds, Monte Carlo simulation is used since their contribution is small and quite well known.

The process $W \to \tau\nu$ is an almost irreducible background to $W \to e\nu$ since the neutrino results in E_T^{miss} and the τ lepton decays in $\sim 18\%$ of the cases in $e\nu_e\nu_\tau$. The energy spectrum of the electron from the τ decay is softer and its track has non-zero impact parameters. However, this last feature is not used since it has been shown that a cut on the impact parameter doesn't improve the analysis.

The process $Z \to ee$ contributes to the $W \to e\nu$ background when one of the two electrons is badly reconstructed or is outside the detector acceptance. The $Z \to ee$ cross-section is about a factor of 10 smaller than the $W \to e\nu$ cross-section.

The process $Z \to \tau\tau$ contributes to the background for essentially the same reason explained in the case of $W \to \tau\nu$ decays.

The $t\bar{t}$ pair production is a background to the $W \to e\nu$ process since one of the top quarks can decay semileptonically resulting in an electron and E_T^{miss}.

The contributions from the diboson production WW, WZ and ZZ is also considered. In the WW and WZ events the W can decay in the electron channel. The ZZ events constitute a background for the same reason as the Z events.

Table 5.2 shows the Monte Carlo samples that are used for this analysis (including signal Monte Carlo as well). The production cross-section of W decaying leptonically into one lepton flavour is calculated to be 10.46 ± 0.52 nb at NNLO. The Z cross-section is about a factor 10 lower. The relative uncertainties on the W and Z production in the leptonic channels are at the level of $\sim 5\%$. The production cross-section for $t\bar{t}$ pairs is 0.165 nb calculated at approximately NNLO with an uncertainty of $\sim 10\%$. The production cross-sections for the dibosons is even lower (about a factor of 10^3). They are calculated at NLO with a relative uncertainty of $\sim 5\%$

To estimate the contamination from these sources in the signal sample, the $W \to e\nu$ selection is run on the corresponding Monte Carlo samples. The number of events after all cuts are normalised to the same luminosity of the data sample using the cross-sections shown on Table 5.2. Table 5.3 summarises the fraction of events for each of the processes described in this Section which are expected in the data sample after the full signal selection.

Physics process	$\sigma \cdot$ BR [nb]	Generator	Normalisation	Luminosity [fb^{-1}]
$W \to e\nu$	10.46 ± 0.52	PYTHIA	NNLO	0.76
$W^+ \to e^+\nu$	6.16 ± 0.31	MC@NLO	NNLO	0.65
$W^- \to e^-\bar{\nu}$	4.30 ± 0.21	MC@NLO	NNLO	0.70
$W \to \tau\nu$	10.46 ± 0.52	MC@NLO	NNLO	0.16
$Z \to ee$	0.99 ± 0.05	PYTHIA	NNLO	9.5
$Z \to \tau\tau$	0.99 ± 0.05	PYTHIA	NNLO	1.0
$t\bar{t}$	$0.165^{+0.011}_{-0.016}$	MC@NLO	NLO+NNLL	165
WW	0.045 ± 0.003	HERWIG	NLO	140
WZ	0.0185 ± 0.0009	HERWIG	NLO	174
ZZ	0.0060 ± 0.0003	HERWIG	NLO	196

Table 5.2: Signal and background Monte Carlo samples as well as the generators used in the simulation. For each sample, the production cross-section multiplied by the branching ratio (BR), used for normalisation, is given. The electroweak W and Z cross-sections are calculated at NNLO, $t\bar{t}$ at approximate NNLO and the diboson cross-sections at NLO. The available luminosity of each sample is also given [54].

Physics process	Fraction of events [%]
$W \to \tau\nu$	1.78 ± 0.02
$Z \to ee$	1.050 ± 0.002
$t\bar{t}$	0.3908 ± 0.0003
$Z \to \tau\tau$	0.151 ± 0.002
Dibosons	0.10382 ± 0.00004

Table 5.3: Fraction of the electroweak background contributions expected in data and their statistical uncertainty computed using MC samples after the selection cuts described in Section 5.1.

5.3 QCD background estimation for the $W \to e\nu$ selection

The cross-section of QCD events is very high (of the order of hundreds of mb) therefore a Monte Carlo evaluation of this source of background would require a huge amount of simulated events which is impossible to realise. Moreover this cross-section is less precisely known than the cross-section of the electroweak processes described earlier. For these reasons, data-driven methods are used to estimate the amount of this source of background. In this analysis, the data-driven method used is the so-called "matrix method". This choice has been made to explore an alternative method with respect to the one used commonly in the ATLAS W inclusive analysis which is based on template fits where the signal shape is taken from simulation. In principle, the matrix method is less dependent on shapes and uses data-driven quantities (except for the electroweak background evaluation).

After the subtraction of the electroweak (EW) background, the number of events passing the selection requirements is the sum of the number of W and QCD events:

$$N_{data} = N_W + N_{QCD} \tag{5.2}$$

Applying an additional cut, a new equation can be written:

$$N_{data}^{cut} = \varepsilon_{sig} \cdot N_W + \varepsilon_{QCD} \cdot N_{QCD} \tag{5.3}$$

where N_{data}^{cut} is the number of events after this additional cut and after the subtraction of the EW background. The additional cut in this analysis is the electron calorimetric isolation and therefore ε_{sig} is the signal isolation efficiency and ε_{QCD} the QCD background isolation efficiency in the selected sample. The eq. 5.2 and 5.3 can be used to extract the number of W events and the number of QCD events:

$$N_W = \frac{N_{data}^{cut} - \varepsilon_{QCD} \cdot N_{data}}{\varepsilon_{sig} - \varepsilon_{QCD}} \text{ and } N_{QCD} = \frac{\varepsilon_{sig} \cdot N_{data} - N_{data}^{cut}}{\varepsilon_{sig} - \varepsilon_{QCD}} \tag{5.4}$$

Therefore the necessary quantities to estimate the number of W candidate events (or equivalently the number of QCD background events) are:

- N_{data}, N_{data}^{cut}, namely the number of data events passing the W selection cuts after the subtraction of the EW background ($N_{measured} - N_{MC,EW}$) before and after the isolation cut respectively,
- the signal isolation efficiency ε_{sig}, which will be measured on data using the Tag&Probe method on $Z \to ee$ events and
- the fraction of QCD background events ε_{QCD}, which will be measured on data using a specially selected sample enriched in QCD events. This sample will be referred to as "QCD

sample" from now on while the sample obtained after the selection described in Section 5.1 and after the electroweak background subtraction will be called "signal sample".

For the purpose of the analysis, the estimation of N_{QCD} from eq. 5.4 will be performed in 10 $|\eta|$ bins and separately for positrons and electrons.

5.3.1 Selection of the QCD sample

The goal is to select a sample of QCD background events that satisfies the W selection criteria. Therefore the selection requirements for this sample must be as similar as possible to the W selection. To select the QCD sample, the same selection criteria as for the W analysis are applied with the following differences:

- a different trigger is used with looser identification requirements as motivated below,
- the electron is required to pass the loose identification criteria and a set of track quality cuts instead of the tight++ identification,
- the electron is required to fail any of the remaining medium identification requirements and
- only events that have at least one reconstructed jet with $p_T > 20$ GeV and $|\eta| < 2.8$ are accepted.

With respect to the trigger used in the W analysis, the QCD sample is selected using trigger items that rely on looser identification criteria to match the looser offline identification requirements described above. The looser trigger items are EF_e20_loose, EF_e20_loose1, EF_e20_looseTrk and EF_g20_loose. Depending on the data-taking period the p_T cut varies from 20 GeV to 22 GeV. The main issue here is that all these triggers are highly prescaled and only correspond to a luminosity of 132 pb^{-1}. The possible bias that may result from the fact that the selection criteria for the QCD sample are not exactly the same as for the signal sample is taken into account in the systematic uncertainty.

The distribution of the isolation variable E_T^{cone30} for the signal sample, for the W Monte Carlo and for the QCD sample is shown in Fig. 5.2. A shift between the data and the signal Monte Carlo sample of ~ 300 MeV is observed. while the QCD isolation distribution obtained using the selected QCD sample describes well the tail of the data distribution. The observed shift has been seen in other analyses as well and will be taken into account here in the systematic uncertainty.

Measuring the QCD isolation efficiency ε_{QCD}

The selected QCD sample is used to measure the term ε_{QCD} which describes the isolation efficiency in the QCD events which are background to the $W \to e\nu$ events. This efficiency is estimated by checking the fraction of electrons and positrons in the QCD sample that also satisfy the

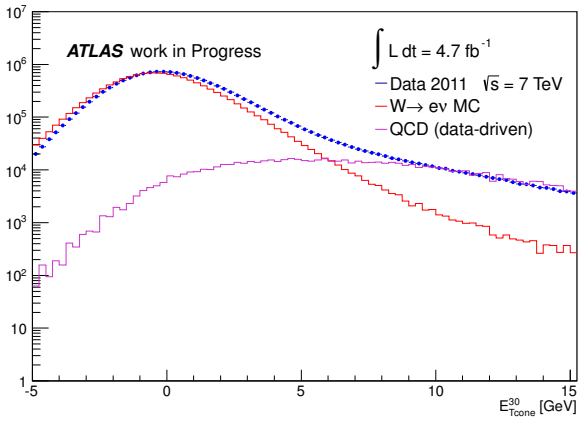

Figure 5.2: Distribution of the isolation variable $E_T^{cone}30$ for data, signal MC and QCD samples using the selected QCD sample.

isolation cut $E_T^{cone30} < 5$ GeV. For the purpose of this analysis the efficiency ε_{QCD} is measured in 10 $|\eta_e|$ bins and separately for electrons and positrons. Due to the limited statistics the statistical uncertainty per bin is $\sim 1.5\%$.

To evaluate the systematic uncertainties of this measurement, two additional methods of selecting the QCD sample are used. The first method requires that the electron candidate fails any of the remaining medium or tight identification requirements and the second one that the electron fails at least one of the remaining medium criteria and at least one of the remaining tight identification criteria.

Fig. 5.3 shows the QCD background isolation efficiencies ε_{QCD} for electrons and positrons as a function of $|\eta_e|$. The efficiencies at different $|\eta|$ are compatible within their uncertainties. The uncertainties shown on the plot include the systematic errors coming from the different selection methods used for defining the QCD sample. The total QCD background efficiency is $(35.4^{+18.4}_{-3.3})\%$.

5.3.2 Measuring the signal isolation efficiencies ε_{sig}

The signal isolation efficiencies are measured on data using the Tag&Probe method on $Z \to ee$ events (see Section 4.7.1). The selection of Z events requires that the event satisfies cleaning cuts. A very well reconstructed tag electron is required with $p_T > 25$ GeV, $|\eta| < 2.47$, outside the transition region, satisfying the tight++ requirements, having triggered the event. The probe electron is required to satisfy the following criteria: $p_T > 25$ GeV, $|\eta| < 2.47$, to be outside the calorimeter transition region and to be tight++ identified. In addition, the probe electron is also required to have triggered the event since the efficiencies will be used on W electrons that have triggered the event. It has been verified that the Tag&Probe signal sample is very clean (QCD

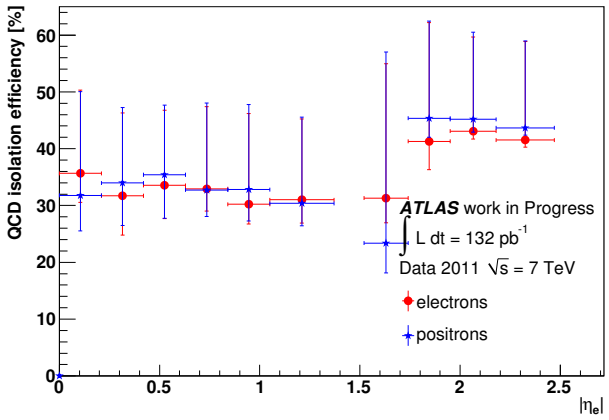

Figure 5.3: Isolation efficiencies ε_{QCD} for electrons *(red)* and positrons *(blue)* as measured using a specially selected QCD sample.

background $\ll 0.5\%$) and therefore no background subtraction is needed. The signal isolation efficiency ε_{sig} is obtained as the fraction of the events in the tag-probe mass region between 80 and 101 GeV in which the probe electron satisfies the isolation requirement $E_T^{cone30} < 5$ GeV.

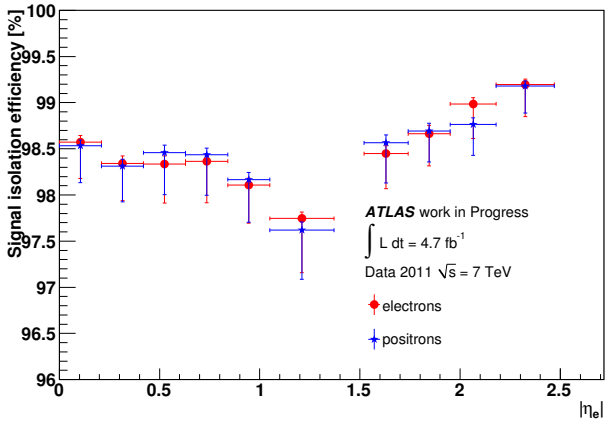

Figure 5.4: Isolation efficiencies ε_{sig} for electrons *(red)* and positrons *(blue)* as measured on $Z \to ee$ data using a Tag&Probe method. The total uncertainty (statistical and systematic) is shown.

The signal isolation efficiencies are shown in Fig. 5.4 for electrons and positrons as a function of $|\eta_e|$. The systematic uncertainties on ε_{sig} are estimated by varying the selection thresholds on the p_T of the tag electron, removing the isolation of the tag electron and the E_T^{miss} requirement. The p_T threshold is moved from 25 GeV to 30 GeV. The di-electron mass region is widened to [76,101] GeV. The variations of the results after each of the above mentioned changes is at most at the level of $\sim 2‰$.

5.3.3 Measuring the number of candidate events

The numbers of events before and after the isolation cut N_{data} and N_{data}^{cut} respectively are measured in 10 bins of $|\eta_e|$ and separately for electrons and positrons. For this measurement, the analysis is run on data and on the EW Monte Carlo samples used for this analysis ($Z \to ee$, $Z \to \tau\tau$ $W \to \tau\nu$, WW, WZ, ZZ and $t\bar{t}$). Then the number of EW background events is scaled to the luminosity and is subtracted in bins of $|\eta|$ from the number of measured events on data to get N_{data} and N_{data}^{cut}. The percentage of the EW background is $\sim 3-4\%$ per channel (W^-, W^+)per bin. To evaluate the systematic uncertainty on the number of EW background events, the theoretical uncertainty on the cross-section for each of the EW processes is taken into account (see Table 5.2). when computing the number of EW background events, a shift of the isolation distribution by 300 MeV is applied to compute an additional term to the systematic uncertainty (see Fig. 5.2).

5.3.4 Results of the QCD background estimation

From eq. 5.4 the number of QCD background events N_{QCD} or directly the number of W candidate events N_W can be computed. Fig. 5.5 shows the number of QCD events before and after the isolation cut ($\varepsilon_{QCD} \cdot N_{QCD}$) for electrons and positrons in bins of $|\eta_e|$. The fraction of QCD events varies from $\sim 1.5\%$ to $\sim 4\%$ depending on the bin. The QCD background for the electron and positron final state agrees within the uncertainty.

From eq. 5.4 the number of W candidate events N_W can also be expressed as:

$$N_W = \frac{N_{data} \cdot (R - \varepsilon_{QCD})}{\varepsilon_{sig} - \varepsilon_{QCD}}, \text{ where } R = N_{data}^{cut}/N_{data}. \tag{5.5}$$

The uncertainties are evaluated through error propagation and there are four contributions:

- $\dfrac{\Delta R}{R - \varepsilon_{QCD}}$
- $\dfrac{\Delta \varepsilon_{sig}}{\varepsilon_{sig} - \varepsilon_{QCD}}$
- $\dfrac{R - \varepsilon_{sig}}{(R - \varepsilon_{QCD})(\varepsilon_{sig} - \varepsilon_{QCD})} \Delta \varepsilon_{QCD}$
- $\dfrac{\Delta N_{data}}{N_{data}}$.

The total uncertainty (statistical and systematic) on the number of W candidate events after the isolation cut ($\varepsilon_{sig} \cdot N_W$) is at the level of $\sim 1.2-3.2\%$ depending on the bin and the main contributions are the uncertainty on the signal and background isolation efficiencies.

Table 5.4 summarises the number of events in the data sample, the measured number of QCD background events and the electroweak background events estimation from Monte Carlo.

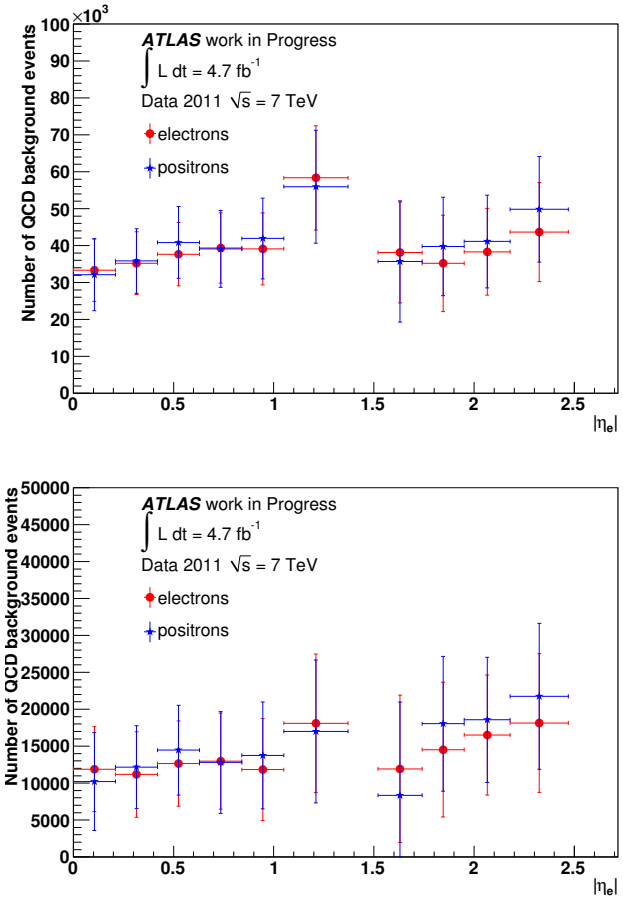

Figure 5.5: Number of QCD background events for electrons *(red)* and positrons *(blue)* before *top plot* and after *bottom plot* the isolation cut as computed using the described matrix method. The uncertainties shown are both statistical and systematic contributions from the error propagation of each term in eq. 5.4.

Fig. 5.6 shows the electron pseudorapidity distribution and the E_T^{miss} distribution after the selection requirements where the data sample, the shape from the QCD sample and the Monte Carlo simulation are superimposed.

	Data	$W \to e\nu$	QCD	$W \to \tau\nu$	$Z \to ee$	$t\bar{t}$	$Z \to \tau\tau$	$WW/WZ/WW$
before	14041.7	12423.	800.6	244.2	144.11	55.919	20.42	14.335
isolation	$\pm$ 3.7	$\pm$ 10.	$\pm$ 4.8	$\pm$ 2.7	$\pm$ 0.27	$\pm$ 0.040	$\pm$ 0.31	$\pm$ 0.025
after	13300.2	12223.	283.1	236.9	139.70	51.980	20.04	13.808
isolation	$\pm$ 3.6	$\pm$ 10.	$\pm$ 2.9	$\pm$ 2.6	$\pm$ 0.26	$\pm$ 0.039	$\pm$ 0.31	$\pm$ 0.024

Table 5.4: Number of events before and after the final isolation cut given in units of 10^3. For the signal and the electroweak background contributions the numbers are extracted from simulation. The QCD events are obtained with the described data-driven technique. The errors shown are only statistical.

	Data	Total MC & QCD
before isolation	14041.7 $\pm$ 3.7	13703. $\pm$ 12.
after isolation	13300.2 $\pm$ 3.6	12969. $\pm$ 11.

Table 5.5: Number of events before and after the final isolation cut. The last column represents the sum of the signal Monte Carlo, the electroweak background Monte Carlo and the QCD background. The errors shown are only statistical.

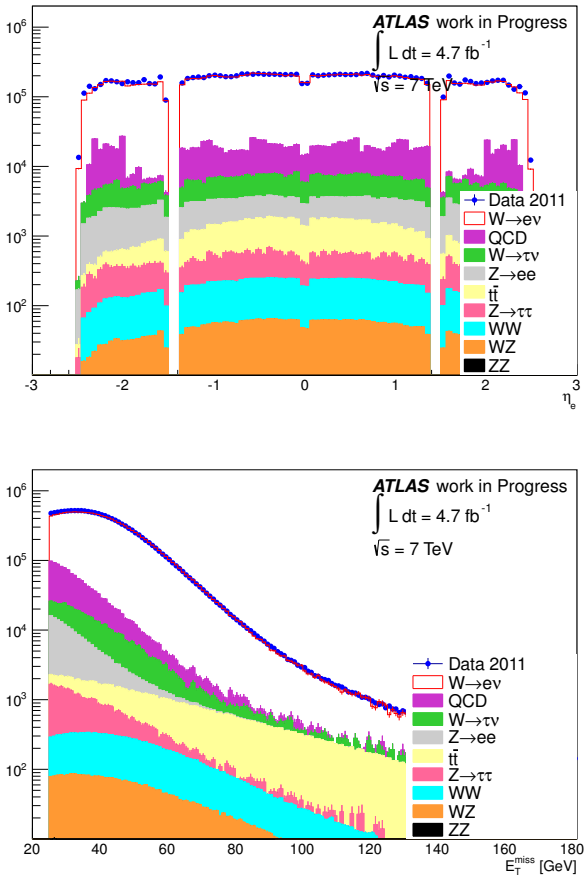

Figure 5.6: Distribution of the electron pseudorapidity (*top*) and E_T^{miss} (*bottom*) in the selected $W \to e\nu$ sample. The simulation is normalised to the data luminosity. The QCD background shapes are taken from background control samples with relaxed electron identification criteria (bottom) and are normalised to the total number of QCD events expected, as described in the text.

Chapter 6

W cross-section Measurement and Charge Asymmetry

The measurement of the production cross-section of W^+ and W^- bosons and of the W charge asymmetry in hadron colliders can be used to constrain the Parton Distribution Functions (PDFs). These measurements have been performed at the TeVatron experiments and the results were included in PDF global fits. They have also been performed by the LHC experiments with the 2010 data. At LHC a new kinematic region is available allowing to further constrain the PDFs.

The W charge asymmetry is defined as:

$$A = \frac{\sigma_{W^+} - \sigma_{W^-}}{\sigma_{W^+} + \sigma_{W^-}} \tag{6.1}$$

The advantage of introducing this variable is that in the ratio, the effects of some of the uncertainties cancel out, in particular the uncertainty due to the luminosity.

In this chapter, the measurement performed by the author of the thesis of the W^+ and W^- cross-sections (times the leptonic branching ratio) and as a function of the pseudorapidity of the charged lepton from the W decay with the 2011 ATLAS data is described. In the analysis, the electronic channel $W \to e\nu$ has been used. The charge asymmetry measurement as a function of the pseudorapidity of the decay electron (positron) is also presented.

6.1 W cross-section Measurement

6.1.1 Method

After the $W \to e\nu$ event selection, the total inclusive cross-section, σ^W_{tot}, of the W production times the branching ratio of the W to an electron and a neutrino can be calculated using the

following relation:

$$\sigma_{tot}^{W} \cdot BR(W \to e\nu) = \frac{N_{data} - N_{bkg}}{A \cdot L \cdot \varepsilon_1 \cdot ... \cdot \varepsilon_n} \tag{6.2}$$

where N_{data} and N_{bkg} are the numbers of data and background events respectively after all selection requirements, A is the fraction of events that fall within the detector acceptance, L is the machine luminosity and ε_1,...,ε_n are the efficiencies of each selection cut. The factor A allows to extrapolate from the fiducial region to the full phase space. It is obtained using Monte Carlo simulation and is defined as the ratio between the number of events in the fiducial region divided by the total number of generated events in the full phase space.

In this analysis, the selection efficiencies of each cut are not used directly. Instead the Monte Carlo simulation is corrected to reproduce the detector resolutions and efficiencies in data and the total inclusive cross-section of the W production multiplied by the branching ratio of the W decaying into an electron and a neutrino is obtained using the following expression:

$$\sigma_{tot}^{W} \cdot BR(W \to e\nu) = \frac{N_{data} - N_{bkg}}{A \cdot C_W \cdot L} \tag{6.3}$$

In this expression C_W is obtained from the corrected Monte Carlo simulation and is defined as the ratio of the number of reconstructed events after all selection cuts divided by the number of generated events inside the detector fiducial region. For this analysis, the fiducial region is defined by the following cuts:

- $p_T^e > 25$ GeV, $|\eta_e| < 2.47$ and outside the transition region (these are referred to as "electron fiducial cuts"),
- $p_T^\nu > 25$ GeV and
- $m_T^W > 40$ GeV.

When computing the number of generated events inside the fiducial region, the electron momentum and pseudorapidity is taken after the final state QED radiation.

The fiducial cross-section is:

$$\sigma_{fid}^{W} \cdot BR(W \to e\nu) = \frac{N_{data} - N_{bkg}}{C_W \cdot L}. \tag{6.4}$$

The use of the fiducial cross-section reduces the dependence on theory and facilitates the comparison between experimental results and theoretical calculations.

6.1.2 C_W Correction Factors

As anticipated above, the C_W factors are defined as the number of simulated W events that satisfy all the selection requirements, over the number of generated events in the fiducial region:

$$C_W = \frac{N^{fid}_{MC,reco}}{N^{fid}_{MC,gen}}. \tag{6.5}$$

Since the aim of this work is to measure the integrated cross-section and the differential cross-section as a function of the pseudorapidity of the lepton, C_W factors per $|\eta|$ bin, $(C_W)_i$, are also defined and are used to unfold the η dependent distribution:

$$(C_W)_i = (\frac{N^{fid}_{MC,reco}}{N^{fid}_{MC,gen}})_i.$$

The C_W and $(C_W)_i$ factors are computed for W^+ and W^- events. The following bins of η have been used:

$$|\eta_e| = [0,\ 0.21,\ 0.42,\ 0.63,\ 0.84,\ 1.05,\ 1.37,\ 1.52,\ 1.74,\ 1.95,\ 2.18,\ 2.47].$$

Here the η variable refers to the η of the electron track at the point of minimal distance with respect to the primary vertex as measured by the tracking detectors. The choice of the bin size results from an optimisation procedure which takes into account the expected statistical and systematic error for a given bin. It has been verified that the purity in each bin is above 98% (see Fig. 6.1). The purity is defined as the ratio between the number of events reconstructed and generated in a given η bin divided by the number of events reconstructed in that bin. The purity accounts for migration effects among bins due to the resolution in η. Since the resolution with which η is reconstructed is very good, the purity is almost one and sophisticated unfolding procedures are not necessary.

When measuring the C_{W^+} and C_{W^-} factors, in order to treat separately the charge misidentification effect, reconstructed positrons (electrons) that are generated as positrons (electrons) are considered.

In order to use the C_W factors to obtain the cross-section, the Monte Carlo simulation needs to describe the data in the best possible way. For this reason, a number of small corrections (scale factors) are applied to account for differences between the Monte Carlo simulation and the data. More specifically, corrections for the electron trigger efficiencies, reconstruction efficiencies and tight++ identification efficiencies are applied according to the recommendation of the ATLAS performance group which is in charge of providing the parameters describing the response of the detector to electrons and photons (ATLAS EGamma combined performance group). These set of corrections are obtained by dedicated measurements using the Tag&Probe method [51]. Additional corrections include an electron energy scale correction and a smearing of the electron energy resolution obtained by an in-situ calibration of the Z peak. In Fig. 6.2, the C_W correction factors

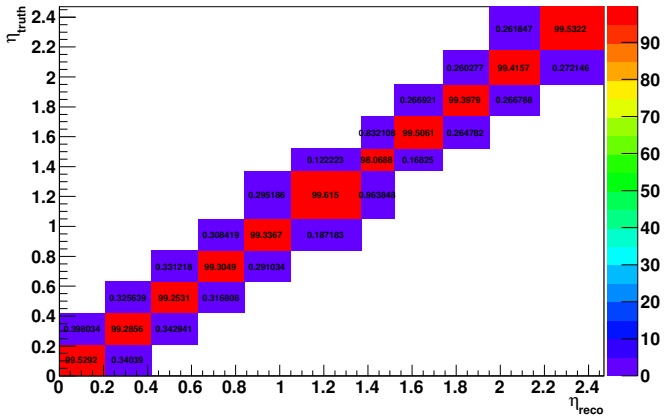

Figure 6.1: Purity of the signal sample in the pseudorapidity region used for the analysis. The purity is measured as the ratio of the number of generated and reconstructed events in a given bin divided by the number of reconstructed events in that bin. For illustration purposes only bins with purity greater than 0.1% are shown on the plot.

with their statistical and systematic uncertainty are shown as a function of the pseudorapidity of the candidate electron (positron). The values of C_W factors for the inclusive W cross-section measurements are: $C_W^- = 0.579 \pm 0.010$ and $C_W^+ = 0.565 \pm 0.012$ (the errors include both statistical and systematic uncertainties). The $\sim 1\sigma$ difference between the C_W^+ and C_W^- factors is due to the fact that the electron E_T spectrum is harder than the positron one and the electron (and positron) identification efficiency is higher at higher E_T.

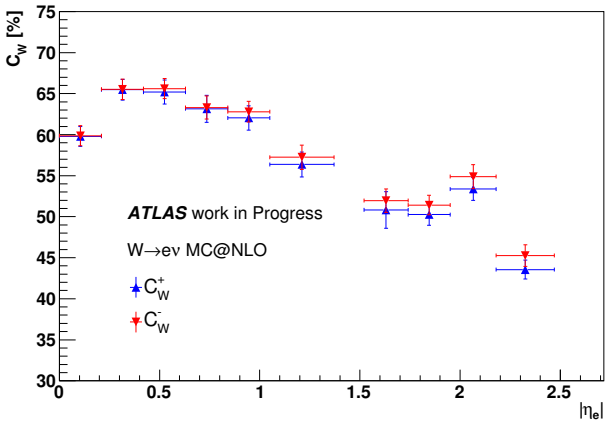

Figure 6.2: C_W correction factors for electrons (*red*) and positrons (*blue*). The error bars represent both statistical and systematic uncertainties.

6.1.3 C_W Systematic Uncertainties

Systematic uncertainties arise from a number of effects that are addressed in this section. They are evaluated by varying separately each pertinent parameter and recalculating the C_W factors. as described in the following. Table 6.1 summarises the impact of each of these effects on the inclusive C_W correction factors. No theoretical uncertainty on the inclusive C_W factors, which can be evaluated by reweighting to different PDF sets, has been considered since the effect is small.

The η dependent C_W uncertainties are shown in Tables 6.2 and 6.3. No systematic uncertainty on C_W arising from the shape of the theoretical cross-section as a function of $|\eta|$ in Monte Carlo has been included. This contribution which can be evaluated by reweighting the underlying shape with different PDF sets, has been found negligible since the purity is practically 1.

	δC_W^- [%]	δC_W^+ [%]
Pile-up modeling	< 0.1	< 0.1
Vertex position	0.2	0.2
Electron energy resolution	0.2	0.2
Electron reconstruction	0.8	0.8
Electron identification	1.0	1.1
Trigger	0.6	0.6
E_T^{miss} scale and resolution	1.0	1.6
Total	1.7	2.2

Table 6.1: Table summarising the systematic uncertainties considered for the inclusive C_W^- and C_W^+ correction factors.

Pile-Up Uncertainty

In the Monte Carlo samples used, the effect of the pile-up is well modelled. Residual differences in the pile-up description between data and Monte Carlo simulation have been corrected by reweighting the Monte Carlo events to reproduce the average number of interactions per bunch-crossing. In order to estimate the systematic uncertainty from the pile-up modelling, the reweighting procedure is removed from the analysis. The effect is small $O(10^{-4})$.

η_e	[0, 0.21]	[0.21, 0.42]	[0.42, 0.63]	[0.63, 0.84]	[0.84, 1.05]	[1.05, 1.37]	[1.52, 1.74]	[1.74, 1.95]	[1.95, 2.18]	[2.18, 2.47]
Electron reconstruction [%]	1.1	1.1	1.1	1.0	0.6	0.6	0.6	0.6	0.6	0.7
Electron identification [%]	0.9	0.8	0.8	0.8	0.8	0.8	1.5	1.5	1.5	1.5
Trigger [%]	0.6	0.6	0.6	0.6	0.6	0.6	0.6	0.6	0.6	0.8
E_T^{miss} scale and resolution [%]	1.4	1.2	1.1	1.7	1.6	2.2	2.1	1.5	2.0	2.3

Table 6.2: Table summarising the main systematic uncertainties considered for the C_W^- correction factors for the differential measurement in bins of the electron pseudorapidity

η_e	[0, 0.21]	[0.21, 0.42]	[0.42, 0.63]	[0.63, 0.84]	[0.84, 1.05]	[1.05, 1.37]	[1.52, 1.74]	[1.74, 1.95]	[1.95, 2.18]	[2.18, 2.47]
Electron reconstruction [%]	1.1	1.1	1.1	1.0	0.6	0.6	0.6	0.6	0.6	0.8
Electron identification [%]	0.9	0.9	0.9	0.8	0.8	0.8	1.5	1.5	1.5	1.5
Trigger [%]	0.6	0.6	0.6	0.6	0.6	0.6	0.6	0.6	0.6	0.8
E_T^{miss} scale and resolution [%]	1.3	1.2	1.7	2.2	2.1	2.4	4.0	1.9	1.9	1.9

Table 6.3: Table summarising the main systematic uncertainties considered for the C_W^+ correction factors for the differential measurement in bins of the electron pseudorapidity

Primary Vertex Position along the z-axis

The distribution of the z coordinate of the primary vertex differs between the data and the Monte Carlo (see Fig. 6.3). For this reason, a reweighting procedure is applied to the simulation in order to match the data distribution. The effect on the C_W factors is small ($\sim 2‰$).

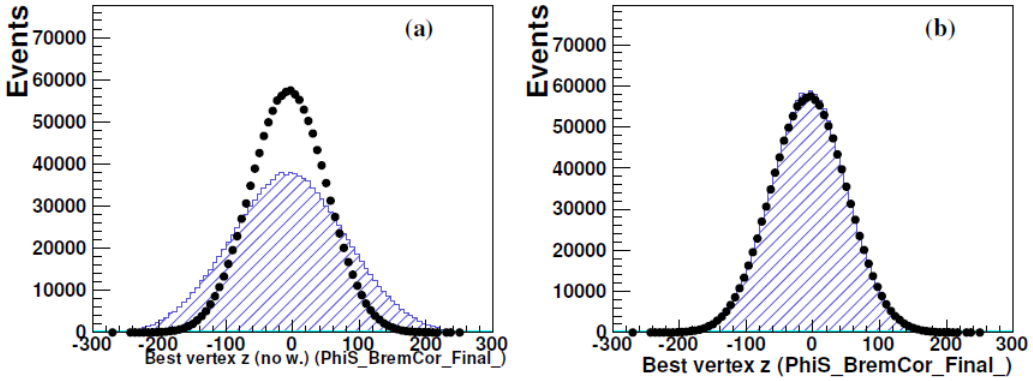

Figure 6.3: Distributions of the z position of the reconstructed primary vertex for the Monte Carlo production used for 2011 analyses. Data (black dots) are compared to the simulation (hatched histograms), before (*left*) and after (*right*) applying the reweighting procedure [55].

Electron Energy Resolution Uncertainty

To account for different electron energy reconstruction in data and simulation, the energy in simulation is smeared to reproduce the measured resolution. The uncertainty on the electron energy resolution is obtained using the recommendation by the ATLAS EGamma combined performance group. Variations of $\pm 1\sigma$ on the smearing of the energy resolution of the electron candidate are applied on the electron candidate. The effect on the C_W factors is small ($\sim 2‰$). The effect of the electron energy scale uncertainty is evaluated on data and is described later.

Electron Reconstruction and Identification Uncertainty

As explained previously, the simulation is corrected for all differences observed with respect to data using scale factors SF$= \frac{\varepsilon_{data}}{\varepsilon_{MC}}$ where ε_{data} and ε_{MC} are the data and Monte Carlo efficiencies respectively. As an example, fig. 6.4 shows the data and Monte Carlo reconstruction and tight identification efficiencies as function of η [1]. The scale factors and their uncertainties are again provided by the EGamma performance group. The reconstruction scale factors vary from one by about 1% with an uncertainty of 1%. The tight++ identification scale factors are away from unity by 1% in the low η region and their deviation reaches 3% at high η ($|\eta| > 2$). The uncertainty on the identification scale factors is within 1%. Variations of $\pm 1\sigma$ are applied on the reconstruction

[1] The figure shows the results for the 2010 data since official ATLAS plots are not yet released. In this analysis, the updated reconstruction and identification values derived using the 2011 data are used.

and identification scale factors leading to differences $\sim 0.5\%$ (depending on the bin) for the C_W factors.

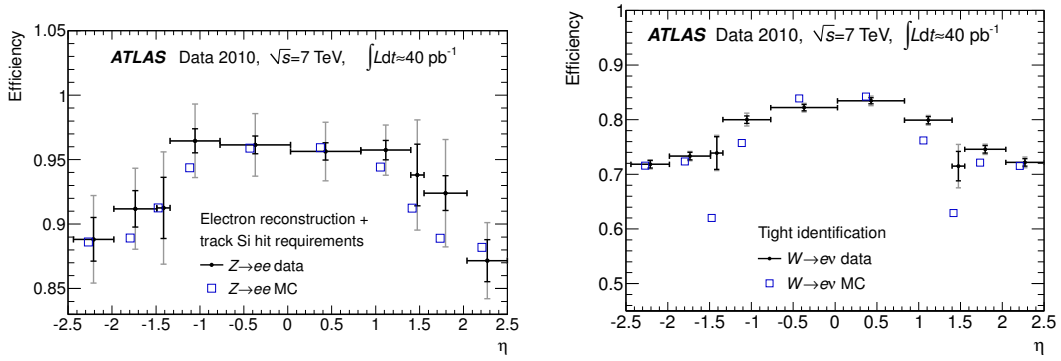

Figure 6.4: *Left plot:* Reconstruction efficiencies measured from $Z \to ee$ events and predicted by Monte Carlo as a function of the pseudorapidity. *Right plot:* Tight identification efficiencies measured from $W \to e\nu$ events and predicted by Monte Carlo as a function of the pseudorapidity [51].

Electron Trigger Efficiency Uncertainty

An additional scale factor used in this analysis takes into account the difference between the efficiency in data and simulation of the electron trigger. For the first two triggers used (EF_e20_medium, EF_e22_medium), the scale factors are within $\sim 2\%$ from unity with an uncertainty of $\sim 1\%$ while for the last trigger (EF_e22vh_medium1) the scale factors are within $\sim 4\%$ with an uncertainty of $\sim 2\%$. Again, a variation of $\pm 1\sigma$ is applied on the scale factor to estimate the systematic uncertainty on the C_W factors ($\sim 0.5\%$).

E_T^{miss} Scale and Resolution Uncertainty

The uncertainty coming from the uncertainty on the E_T^{miss} scale and resolution is evaluated using the tool provided by the Jet/E_T^{miss} combined performance group. There is more than one effect to take into account in this case. Namely the effects studied here are the uncertainty on the electron energy scale and resolution, on the jet energy scale and resolution, on the pile-up modeling and on the soft jets and topological clusters not associated to physics objects (CellOut term of the E_T^{miss}).

Each contribution is studied separately. The electron energy resolution is smeared in simulation and the electron term of the E_T^{miss} is recomputed. The new E_T^{miss} value and the new electron energy value are used to recompute the C_W factors and evaluate the uncertainty on them coming from the E_T^{miss} (see Section 4.8) due to the electron energy resolution. The impact of the electron energy scale is evaluated by recomputing the C_W factors after the scaling of the electron term of E_T^{miss}. Overall the uncertainty on the C_W factors due to the uncertainty of the electron energy scale is at the level of $\sim 3‰$ and the impact from the energy resolution is even lower.

Then the uncertainty on E_T^{miss} from the jet measurement is studied. The uncertainties are evaluated by varying the jet energy scale and separately the jet energy resolution according to their errors and recomputing the term $E_T^{miss,jets}$. The difference caused by this effect is used to estimate the uncertainty due to E_T^{miss}. The uncertainty from the jet energy scale is the dominant one with an effect of $\sim 7‰$ reaching 1% for certain bins. The jet energy resolution has a smaller impact on the C_W uncertainty ($\sim 4‰$).

Finally, two more sources are studied. One is the effect of the calibration of the soft jets and clusters not belonging to physics objects and the other is a pileup uncertainty of the level of 6.6%. The uncertainty from the calibration procedure and the pileup modeling on the C_W factors is $\sim 5‰$ and $\sim 2‰$ respectively.

To estimate the uncertainty of the E_T^{miss} on the C_W factors, the variations of all these different contributions are summed in quadrature. The E_T^{miss} uncertainty is computed for every $|\eta|$ bin and adds to the C_W an uncertainty of $1.1-2.4\%$ with the exception of one bin ($1.52 < |\eta| < 1.74$) where the uncertainty reaches the level of 4% mainly due to the soft jets and topological clusters effect.

6.1.4 Systematic Uncertainties from the Number of W Candidate Events

As indicated by eq. 6.4, in addition to the uncertainty on the C_W factors, the uncertainty on the number of W candidate events also needs to be propagated to the cross-section measurement. In this section, two more sources of uncertainty are taken into account: the electron energy scale and the QCD background uncertainty.

Electron Energy Scale Uncertainty

The electron energy scale uncertainty is applied on data as recommended by the ATLAS EGamma group. Variations of $\pm 1\sigma$ are applied on the electron energy scale on an event-by-event basis. The systematic uncertainty on the number of W candidate events is at the level of $\sim 2‰$.

Electroweak Background Uncertainty

The uncertainty coming from the electroweak background is evaluated by varying the cross-section used to extract the number of events from the simulation by 5% (10% for the $t\bar{t}$ background) as described in Section 5.2. The impact on the uncertainty of the number of W candidate events is within $2‰ - 3‰$.

QCD Background Uncertainty

The evaluation of the QCD background as described in Section 5.3 contributes to the uncertainty of the number of W candidate events by a percentage of x. This uncertainty is propagated to the

final cross-section measurement. The QCD background is found to have an impact of 1.9% on the total cross-section. For the differential cross-section the uncertainty from the QCD background estimation is $1.1\% - 1/9\%$ in the barrel region ($|\eta| < 1.37$) while in the end-cap region it can reach 3.4% depending on the bin.

Isolation Uncertainty

To estimate the uncertainty coming from the calorimetric isolation a shift of 500 MeV is applied on the electroweak Monte Carlo background samples to account for the difference between data and Monte Carlo (see Fig. 5.2). The impact of this shift on the uncertainty of the number of candidate events is negligible ($< 1‰$).

6.1.5 Charge Misidentification Correction

Before computing the W^+ and W^- differential cross-sections, it is necessary to take into account the effect of the charge misidentification. As mentioned previously, the C_W factors are computed for electrons and positrons having a correctly identified charge. We need therefore to correct the number of W^+ and W^- events measured in data, N_{W^+} and N_{W^-}, for the effect of the charge misidentification.

To obtain from N_{W^+} and N_{W^-} the true number of W^+ and W^- the following expressions are used:

$$N_{W^+} = \varepsilon^+ N^+ + (1-\varepsilon^-)N^- \tag{6.6}$$

$$N_{W^-} = \varepsilon^- N^- + (1-\varepsilon^+)N^+ \tag{6.7}$$

where ε^+ is the probability of a positron to be reconstructed as positron, ε^- is the probability of an electron to be reconstructed as electron and N^+, N^- the numbers of true W^+ and W^- events produced.

Using the system of the eq. 6.6 and 6.7, N^+ and N^- are expressed as:

$$N^+ = N_{W^+} + \frac{(1-\varepsilon^-)N_{W^-} - (1-\varepsilon^+)N_{W^+}}{1-\varepsilon^-\varepsilon^+} \tag{6.8}$$

$$N^- = N_{W^-} + \frac{(1-\varepsilon^+)N_{W^+} - (1-\varepsilon^-)N_{W^-}}{1-\varepsilon^-\varepsilon^+} \tag{6.9}$$

In Section 4.7, the charge identification measurement was studied. There, it was found that the probability of correctly identifying the charge of electrons and positrons agree. Therefore, we will assume here that $\varepsilon^- = \varepsilon^+ = \varepsilon$. This choice allows to reduce the statistical uncertainty on the charge identification rates. In addition, given the stability of the charge identification rates in the barrel region ($|\eta| < 1.37$), only one bin for the barrel will be considered. The ε values used are shown in Fig. 6.5. On average, the fraction of particles with correctly identified charge is

$\varepsilon = (99.48 \pm 0.02)\%$.

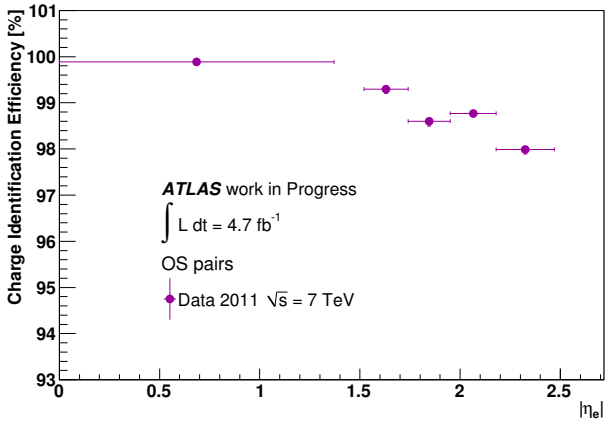

Figure 6.5: Charge identification efficiencies used to correct from the measured number of W^+ and W^- events to the true number of W^+ and W^- produced.

The effect of the uncertainty of the charge identification correction on the number of W^+ and W^- is very small ($< 1‰$).

6.2 W Cross-section Results

After measuring the number of W events in the analysed sample, correcting for charge misidentification effects and computing the C_W factors, the cross-section in the fiducial region is calculated as:

$$\sigma_{\pm} \cdot BR(W \to e\nu) = \frac{N^{\pm}}{C_W^{\pm} \cdot L}. \tag{6.10}$$

The cross-section for the W^+ and W^- bosons in the fiducial region are shown on the top part of Table 6.4. The uncertainty on the luminosity during the 2011 data-taking has been measured in ATLAS and found to be 3.9%. The bottom part of the table shows the theory prediction for the W^+ and W^- cross-sections in the fiducial region calculated at next-to-next-to-leading order using the FEWZ program [56]. The PDF set used is MSTW2008 PDF. The data measurement and the theory prediction are in good agreement. The theory uncertainty includes the variations of the PDF eigenvectors and the α_s uncertainty. The graphical representation of these results are shown in Fig. 6.6.

Table 6.5 shows the comparison between the 2010 and 2011 measurements. and Fig. 6.7 its graphical representation. More precisely, the top part of the table shows the results obtained by the ATLAS experiment in the electron channel $W \to e\nu$ using the 2010 data and the middle part displays the combined electron and muon measurement [57]. The fiducial region for the 2010 measurement is slightly different from the one presented in this thesis and is defined by the fol-

$\sigma_W^{fid} \cdot BR(W \to e\nu)$ [nb]				
		stat	syst	lumi
W^+	2.780	$\pm$ 0.003	$\pm$ 0.079	$\pm$ 0.108
W^-	1.890	$\pm$ 0.002	$\pm$ 0.055	$\pm$ 0.074
$\sigma_W^{fid,TH} \cdot BR(W \to e\nu)$ [nb]				
		stat	PDF+α_s	
W^+	2.875	$\pm$ 0.005	$^{+0.139}_{-0.119}$	
W^-	1.946	$\pm$ 0.005	$^{+0.085}_{-0.082}$	

Table 6.4: Cross-sections times the leptonic branching ratios for W^+ and W^- production within the fiducial region of the measurement. *Top*: The measured cross-sections using the full 2011 data are shown. The uncertainties denote the statistical (stat), the experimental systematic (syst) and the luminosity (lumi) uncertainties. *Bottom*: Theoretical prediction obtained using the FEWZ program at NNLO with the MSTW2008 PDF set.

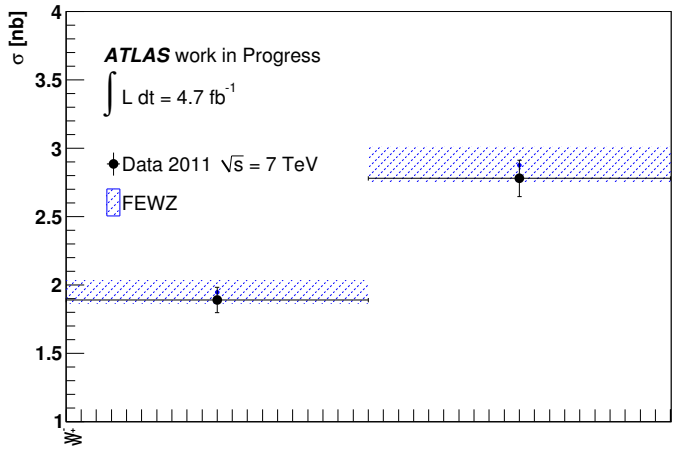

Figure 6.6: The comparison between the 2011 obtained results and the theoretical prediction. The data uncertainties include statistical, systematic and luminosity contributions while the theoretical uncertainties include the PDF and α_s errors.

	$\sigma_W^{fid,2010} \cdot BR(W \to e\nu)$ [nb]				
		stat	syst	lumi	
W^+	2.898	$\pm$ 0.011	$\pm$ 0.052	$\pm$ 0.099	
W^-	1.893	$\pm$ 0.009	$\pm$ 0.038	$\pm$ 0.064	
	$\sigma_W^{fid,2010} \cdot BR(W \to l\nu)$ [nb]				
		stat	syst	lumi	acc
W^+	3.110	$\pm$ 0.008	$\pm$ 0.036	$\pm$ 0.106	$\pm$ 0.004
W^-	2.017	$\pm$ 0.007	$\pm$ 0.028	$\pm$ 0.069	$\pm$ 0.002
	$\sigma_W^{fid,2011} \cdot BR(W \to e\nu)$ [nb]				
		stat	syst	lumi	
W^+	3.048	$\pm$ 0.003	$\pm$ 0.079	$\pm$ 0.119	
W^-	2.020	$\pm$ 0.002	$\pm$ 0.055	$\pm$ 0.079	

Table 6.5: Cross-sections times the leptonic branching ratios for W^+ and W^- production within the fiducial region of the measurement used for the 2010 analysis. *Top*: Results showing the ATLAS electron measurement performed using the 2010 data. *Middle*: Results showing the combined (electron and muon) ATLAS measurement performed using the 2010 data. *Bottom*: Results showing the measurement performed in this thesis extrapolated to the fiducial region of the 2010 measurement. The statistical (stat), experimental systematic (syst), the luminosity (lumi) uncertainties and acceptance (acc) uncertainties are shown.

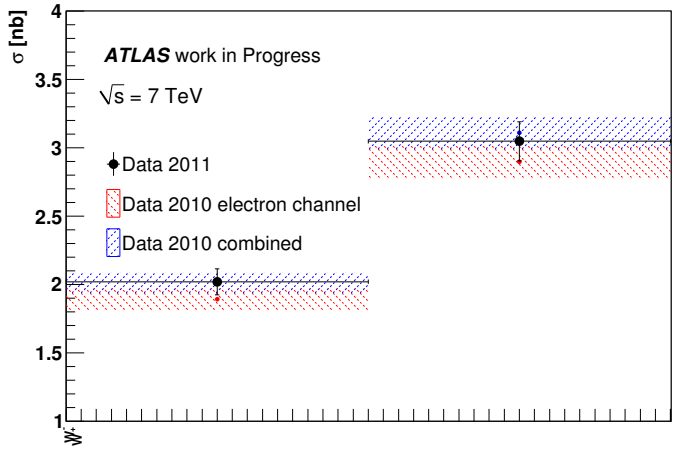

Figure 6.7: The comparison between the 2011 obtained results extrapolated to the fiducial kinematic region used for the 2010 analysis and the 2010 ATLAS published results are shown for the electron channel and for the electron and muon channels combined.

lowing requirements: $E_T^e > 20$ GeV, $E_T^{miss} > 25$ GeV and $m_T^W > 40$ GeV [2]. For this reason, the inclusive fiducial cross-section measured with 2011 data and presented earlier is extrapolated to the fiducial region used for the 2010 analysis. The C_W factors are recomputed and the denominator $N_{MC,gen}^{fid}$ (eq. 6.5) now includes events generated in the fuducial region used for the 2010 measurement. The 2010 and 2011 results presented are compatible.

The fiducial differential cross-sections in bins of the pseudorapidity $|\eta|$ of the electron is also measured. The uncertainties on the C_W factors and on the number of W events in each η bin are propagated to the cross-section. Fig. 6.8 shows the fiducial differential cross-section for W^+ and W^- in units of nb. The left plot shows the fiducial cross-section measured in each $|\eta|$ bin while the results in the right plot are divided by the bin size to better show the shape of the cross-section as a function of $|\eta|$. The error bars show the statistical and the systematic uncertainty while the luminosity uncertainty is not displayed for clarity reasons.

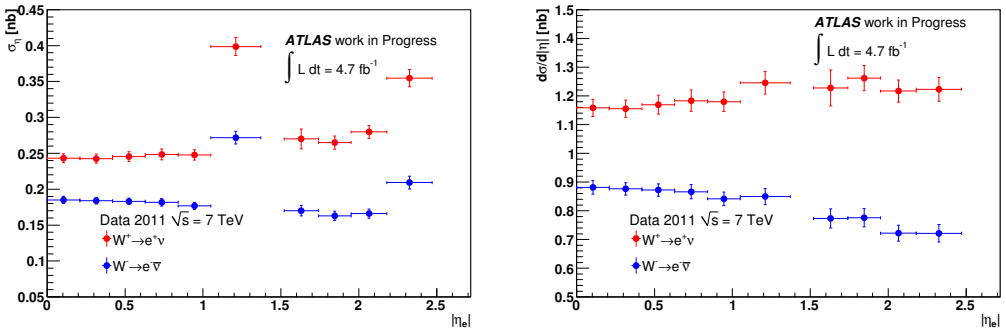

Figure 6.8: The differential $\frac{d\sigma}{d|\eta|}$ cross-section measurements for W^+ and W^- are shown. The left plot shows the cross-section for the W production in each $|\eta|$ bin while the right plot shows the same results divided by the bin size. The luminosity uncertainty is not included.

The differential cross-section measurement has been performed in ATLAS with the 2010 data. Fig. 6.9 shows the published results for the W^+ and W^- cross-sections in the fiducial region used for the 2010 analysis. The method used in 2010 for the QCD background estimation is different and relies on performing a template fit on the E_T^{miss} distribution. The electroweak background is taken from Monte Carlo simulation and the signal template is taken from $W \to e\nu$ MC@NLO simulation. The results presented in the figure are divided by a factor of 2 to account for the absolute value of η.

The comparison between the normalised 2010 published results and the 2011 cross-section measurements presented in this thesis is shown in Fig. 6.10. The 2011 measurement is extrapolated to the fiducial region used for the 2010 analysis. The ratio of the 2011 and 2010 (electron and combined) measurement of the differential cross-sections is shown. The shape as a function of $|\eta|$ is in good agreement.

[2] The reason why the requirement on the E_T was moved to 25 GeV for the 2011 analysis relies on the more stringent trigger requirements.

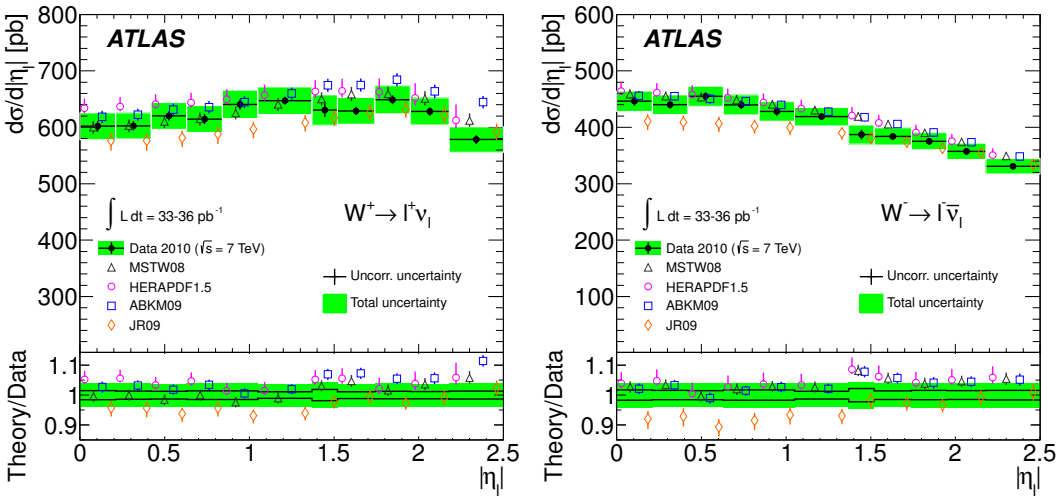

Figure 6.9: The combined differential $d\sigma/d|\eta_l|$ cross sections, for W^+ (*left*) and W^- (*right*) are shown in the fiducial region and their comparison to the NNLO theory predictions using various PDF sets. The ratio of theoretical predictions to data is also shown. Theoretical points are displaced for clarity within each bin [57].

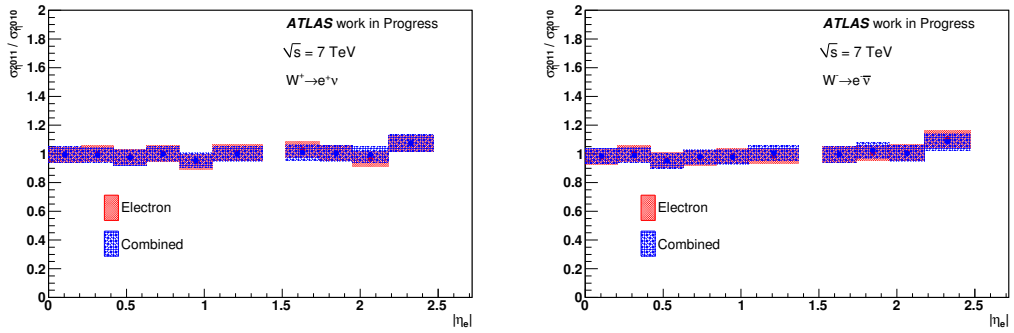

Figure 6.10: Comparison between 2010 and 2011 cross-section results presented as a ratio of cross-sections for W^+ (*left plot*) and W^- (*right plot*). The 2011 results are extrapolated to the fiducial region used for the 2010 measurements. The comparison is shown for the 2010 electron channel and combined results.

In Fig. 6.11 a comparison of the W^+ and W^- differential cross-sections to the theory prediction is shown. To obtain the theory prediction, the MC@NLO simulation was used and reweighted to two different NLO PDF sets.

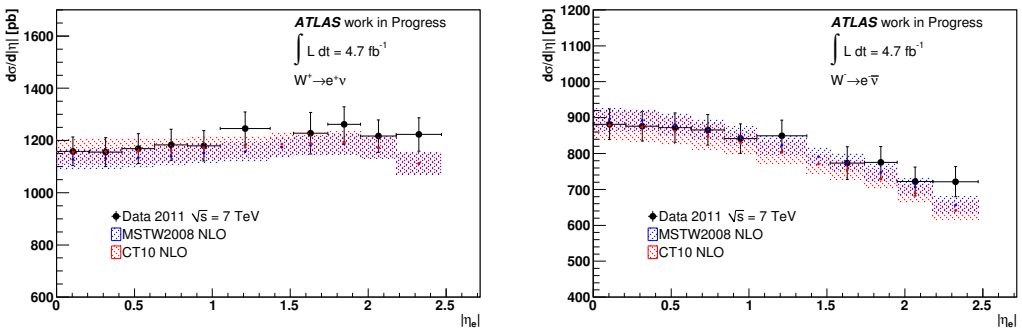

Figure 6.11: Comparison between the measured and predicted differential cross-sections for the W^+ (*left plot*) and W^- (*right plot*) production. The predicted cross-sections are presented at next-to-leading order for the MSTW2008 and CT10 PDF sets.

An example of the use of this kind of results is the evaluation of the strange sea quark using the ATLAS measurement of the W and Z differential cross-sections with the 2010 available statistics. The results indicate an enhanced strange fraction in the proton. The r_s ratio defined as $r_s = 0.5(s+\bar{s})/\bar{d}$ is found to be $r_s = 1.00^{+0.25}_{-0.28}$ at momentum transfer $Q^2 = 1.9\,\text{GeV}^2$ and Bjorken $x = 0.023$, a factor of 2 larger than the theoretical predictions as shown in Fig. 6.12. An enhancement of the strange PDF leads to an improvement in the prediction of the y_Z distribution. This measurement was possible since the ATLAS experiment provided non-normalised W and Z cross-sections.

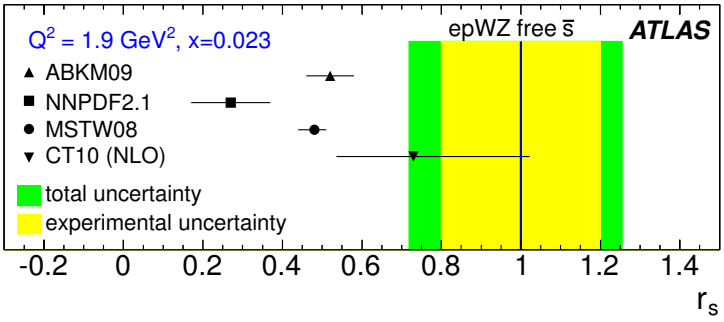

Figure 6.12: Predictions for the ratio $r_s = 0.5(s+\bar{s})/\bar{d}$, at $Q^2 = 1.9\,\text{GeV}^2$, $x = 0.023$. Points: global fit results using the PDF uncertainties using the ATLAS W and Z 2010 measurements and the comparison to different PDF sets [58].

6.3 W Charge Asymmetry Measurement

The W charge asymmetry represents the difference in the production rate of W^+ and W^- bosons divided by the W cross-section. Here it will be presented inclusively and as a function of the charged lepton pseudorapidity.

Using the eq. 6.1 and the results presented in Table 6.4, the inclusive W charge asymmetry is measured and found to be $0.1905 \pm 0.0001 \pm 0.0004$. The first error term represents the statistical uncertainty and the second one the systematic uncertainty after propagating all the cross-section uncertainties presented in the previous Section.

The measurement of the W charge asymmetry will be presented here also as a function of the lepton pseudorapidity according to the following equation:

$$A_e(\eta) = \frac{\frac{d\sigma_{W^+}}{d|\eta|} - \frac{d\sigma_{W^-}}{d|\eta|}}{\frac{d\sigma_{W^+}}{d|\eta|} + \frac{d\sigma_{W^-}}{d|\eta|}}. \tag{6.11}$$

The cross-section measurement described in the previous section will be used here in order to determine the charge asymmetry. Since the asymmetry A_l is a ratio of cross-sections, the luminosity uncertainty does not contribute to the uncertainty of the asymmetry.

The results of the measurement performed with the same selection criteria as described in previous chapters is shown in Fig. 6.13. The uncertainty of each source used in the cross-section measurement is propagated to the asymmetry ratio by varying each term (see Section 6.1.4 and 6.1.3) by $\pm 1\sigma$ and are then summed in quadrature. Table 6.6 shows the W charge asymmetry and its statistical and systematic uncertainty in each bin of pseudorapidity.

$\lvert\eta_e\rvert$	A_l	stat	syst
$[0, 0.21]$	0.1356	$\pm$ 0.0003	$\pm$ 0.0021
$[0.21, 0.42]$	0.1374	$\pm$ 0.0002	$\pm$ 0.0064
$[0.42, 0.63]$	0.1455	$\pm$ 0.0002	$\pm$ 0.0056
$[0.63, 0.84]$	0.1548	$\pm$ 0.0003	$\pm$ 0.0045
$[0.84, 1.05]$	0.1673	$\pm$ 0.0002	$\pm$ 0.0037
$[1.05, 1.37]$	0.1892	$\pm$ 0.0002	$\pm$ 0.0036
$[1.52, 1.74]$	0.2271	$\pm$ 0.0014	$\pm$ 0.0099
$[1.74, 1.95]$	0.2387	$\pm$ 0.0006	$\pm$ 0.0074
$[1.95, 2.18]$	0.2553	$\pm$ 0.0004	$\pm$ 0.0047
$[2.18, 2.47]$	0.2579	$\pm$ 0.0004	$\pm$ 0.0061

Table 6.6: Table showing the asymmetry results as a function of the charged lepton pseudorapidity and its statistical and systematic uncertainties.

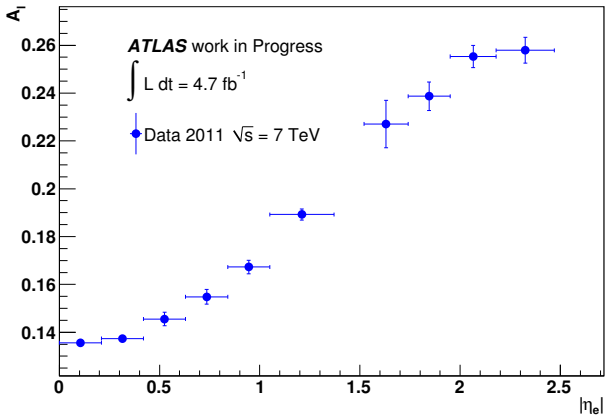

Figure 6.13: Measured W charge asymmetry as a function of the lepton pseudorapidity $|\eta_e|$ compared to theoretical predictions. This measurement uses the full 2011 statistics. The kinematic requirements are $E_T^e > 25$ GeV, $p_T^\nu > 25$ GeV and $m_T^W > 40$ GeV. The transition region $1.37 < |\eta| < 1.52$ is excluded from the analysis.

The W charge asymmetry measurement has been performed in ATLAS using the 2010 data [57]. In Fig. 6.14 the lepton asymmetry is shown combined for the electron and the muon channels. A comparison to different PDF sets is also shown.

The left plot in Fig. 6.15 displays the comparison between the 2010 and 2011 measured charge asymmetry. The fiducial region used for the analysis of this thesis is extrapolated to match the fiducial region of the 2010 measurement. A very good agreement is seen between the 2010 and 2011 results. On the right plot, a comparison of the 2011 measurement to the theory prediction using the MSTW2008 and CT10 PDF sets at next-to-leading order is shown.

The CMS experiment has also performed the charge asymmetry measurement. The published results include two asymmetry measurements where the p_T cut on the lepton differs. Fig. 6.16 shows the lepton asymmetry measurements performed by the CMS collaboration using the 2010 data. The electron and muon combined results are shown for a lepton with $p_T > 25$ GeV on top and for $p_T > 30$ GeV on the bottom. For the QCD background estimation, a template method is used where the E_T^{miss} distribution is fitted.

The LHCb experiment covers a different pseudorapidity region and can probe different x values. The result of the LHCb W charge asymmetry measurement has been performed for the muon channel $W \to \mu\nu$ for a luminosity of $16pb^{-1}$ and is shown in Fig. 6.17. In this region $(2 < |\eta| < 4.5)$ the asymmetry curve is complementary to the one seen at the central region by ATLAS, CMS and previous experiments. In the same figure, a comparison plot of the ATLAS, CMS and LHCb results is shown in the pseudorapidity region $|\eta| < 4$.

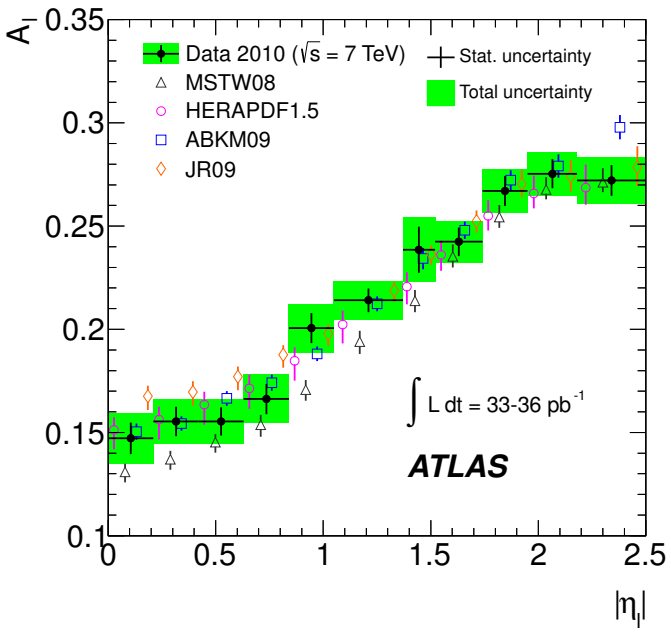

Figure 6.14: W charge asymmetry measured by the ATLAS experiment in 2010 as a function of the lepton pseudorapidity $|\eta_l|$ compared with theoretical predictions calculated to NNLO. Theoretical points are displaced for clarity within each bin [57].

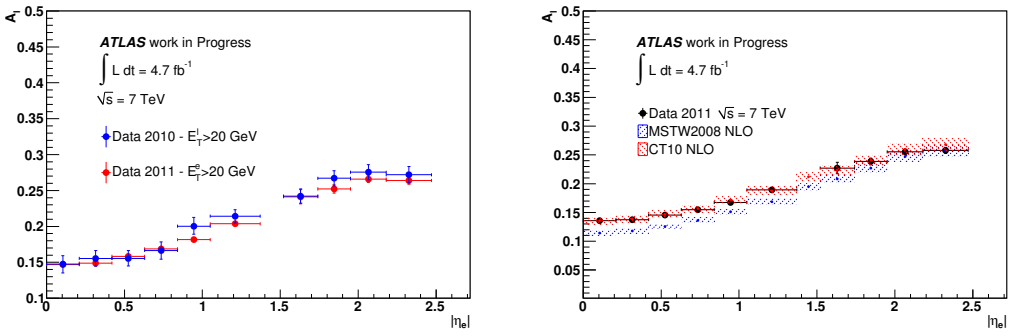

Figure 6.15: *Left*: W charge asymmetry measured using the 2010 (*blue*) and 2011 (*red*) data respectively extrapolated to the same fiducial region. The 2010 measurement represents the combined electron and muon asymmetry measurements while the 2011 analysis includes only the electron measurement. *Right*: Comparison of the 2011 measurement to the theoretical prediction of MC@NLO using the MSTW2008 and CT10 PDFs at NLO.

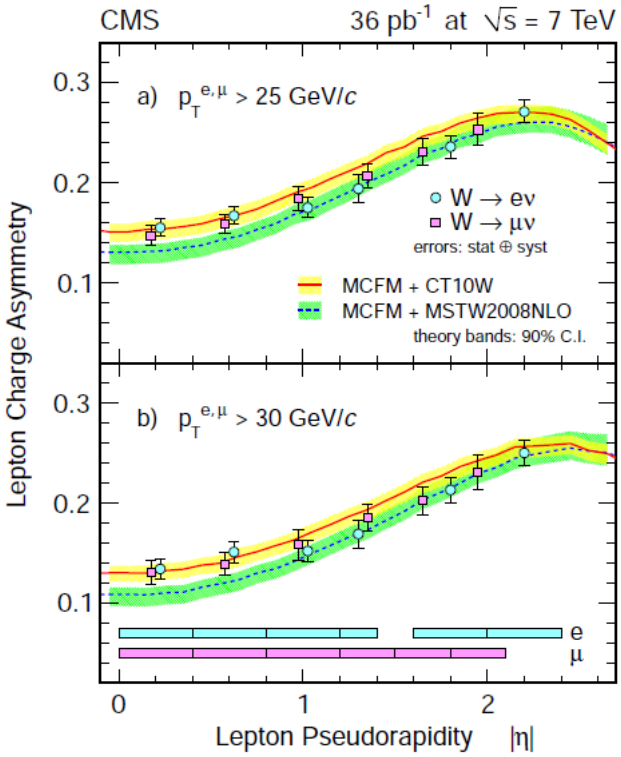

Figure 6.16: CMS results showing the comparison of the measured lepton charge asymmetry to different PDF models for lepton $p_T > 25$ GeV/c (*top*) and lepton $p_T > 30$ GeV/c (*bottom*). The error bars include both statistical and systematic uncertainties. The PDF uncertainty band is corresponding to the 90% confidence interval (C.I.). The bin width for each data point is shown by the filled bars on the bottom. The data points are placed at the centre of pseudorapidity bins, except that for display purposes the first three data points are shifted $+0.025$ (-0.025) for electrons (muons) [59].

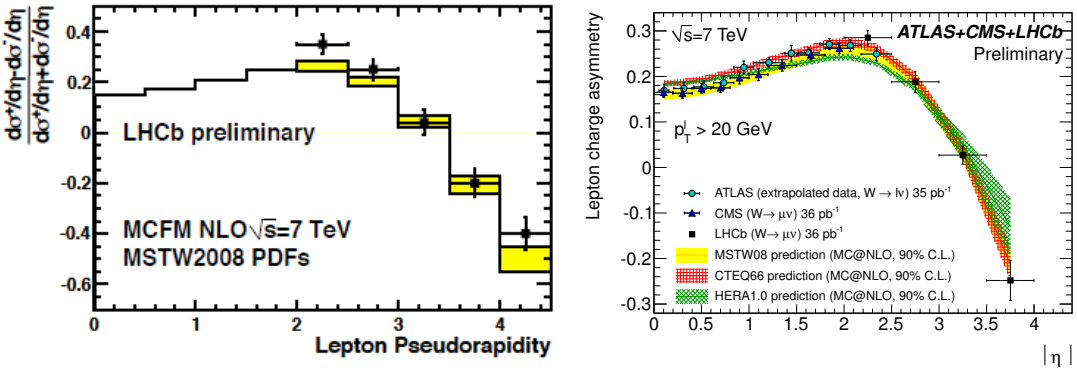

Figure 6.17: *Left:* LHCb results of the W charge asymmetry in bins of lepton pseudo-rapidity compared to the MCFM prediction. The shaded area is the uncertainty arising from the MSTW08NLO PDF set [60]. *Right:* The lepton charge asymmetry from W boson decays in bins of absolute pseudorapidity for the three different experiments ATLAS, CMS and LHCb [61].

6.4 Conclusion

In this chapter, the measurement of the W^+ and W^- cross-sections has been presented inclusively and as a function of the charged lepton pseudorapidity using the 2011 data. The results obtained are in agreement with the theory prediction computed with different parton distribution functions and consistent with the 2010 ATLAS measurement. The dominant systematic uncertainty is the luminosity followed by the uncertainty on the QCD background.

The measurement of the W charge asymmetry has been performed inclusively and gives the following result: $0.1905 \pm 0.0001_{stat} \pm 0.0004_{syst}$. The W charge asymmetry has also been measured as a function of the $|\eta|$ of the charged lepton. The results show good agreement with the 2010 measurement performed by the ATLAS experiment.

Chapter 7

Double Differential Measurement

The measurements of the W cross-sections and of the W charge asymmetry can be extended and analysed not only as a function of the pseudorapidity of the lepton but also as a function of the lepton E_T.

In this chapter, the first double differential measurements of the W^+ and W^- cross-sections and charge asymmetry in ATLAS are presented.

7.1 Analysis

The analysis for the double differential measurement proceeds in a similar way as the single differential one described in the previous Chapters. It is performed in 9 $|\eta|$ bins and 4 E_T bins[1]:

$$|\eta_e| = [0,\ 0.21,\ 0.42,\ 0.63,\ 0.84,\ 1.05,\ 1.37,\ 1.52,\ 1.95,\ 2.18,\ 2.47],$$

$$|E_T^e| = [25,\ 30,\ 35,\ 40,\ 50].$$

The transition region corresponding to the pseudorapidity bin $[1.37,\ 1.52]$ is excluded from the analysis. The binning size has been chosen in order to get a statistical significant result in all bins.

The same event selection described in Section 5.1 is applied here. The electroweak backgrounds ($W \to \tau\nu$, $Z \to ee$, $Z \to \tau\tau$, dibosons WW, WZ, ZZ and the decay of $t\bar{t}$ events) are evaluated using Monte Carlo simulation as before. It is important to mention here that since the Monte Carlo statistics available at the time of this thesis for some of these processes are limited, a larger statistical uncertainty from this source is expected since the analysis is performed in a large number of bins.

[1] The bin $E_T^e > 50$ GeV has not been included in these results. The smaller statistics require a more careful understanding.

The QCD background is estimated as before using the "matrix method" described in Section 5.3. The QCD sample and the sample used for the isolation efficiency measurement with the Tag&Probe analysis are selected with the same requirements described previously. The threshold of the isolation cut applied is optimised depending on the E_T of the electrons (positrons). For the first three E_T bins ($E_T < 40$ GeV), the isolation cut applied is $E_T^{cone30} < 5$ GeV while for the last E_T bin the cut is moved to $E_T^{cone30} < 6$ GeV to compensate for E_T leakage outside the electromagnetic cluster which is observed to be larger for high E_T electrons (see Fig. 7.1). The signal isolation efficiencies are measured on data using a Tag&Probe method on $Z \to ee$ events while the background isolation efficiencies are measured on a specially selected QCD sample.

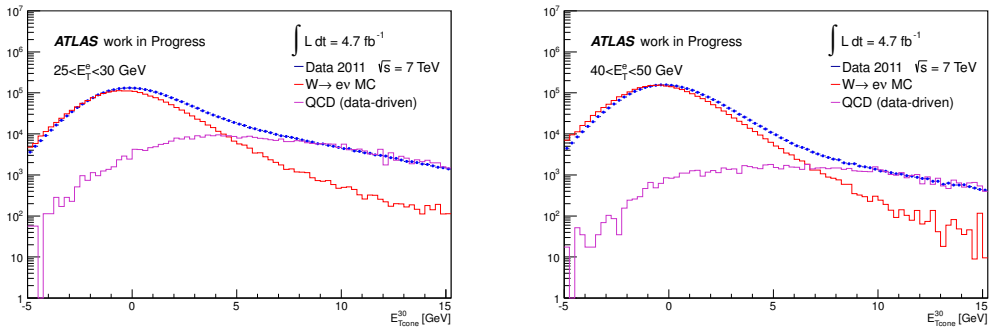

Figure 7.1: Distribution of the isolation variable E_T^{cone30} for the data, signal MC and QCD sample for electrons with transverse energy $25 < E_T < 30$ GeV (*left plot*) and $40 < E_T < 50$ GeV (*right plot*).

From these measured quantities the number of W^+ and W^- events in each bin is evaluated with an uncertainty $\sim 1\%$ in the barrel and $\sim 1.5\%$ in the end-cap. For the first E_T bin — the one with the fewer statistics — the uncertainty is higher at the level of $\sim 4\%$ depending on the bin.

The charge identification rate measurement is repeated in bins of $|\eta|$ and E_T. Due to the observed agreement between the charge identification efficiency for electrons and positrons, it is in this analysis it is measured combining both charges in bins of $|\eta|$ and E_T for this analysis. A slight E_T dependence is observed. The charge identification rates for the first E_T bin are lower by $\sim 2‰$ in the central pseudorapidity region as shown in Fig. 7.2.

Given the levels of the purity of the sample which is greater than 0.68^2 [62] in the defined bins (see Fig. 7.3), no unfolding methods are used. The C_W factors are measured in each ($|\eta|$, E_T) bin and are used to unfold to the true numbers of W boson generated in the fiducial region. The most important uncertainty entering the C_W factors is the uncertainty due to the E_T^{miss} ($\sim 1.5\%$). The C_W factors are shown in Fig. 7.4.

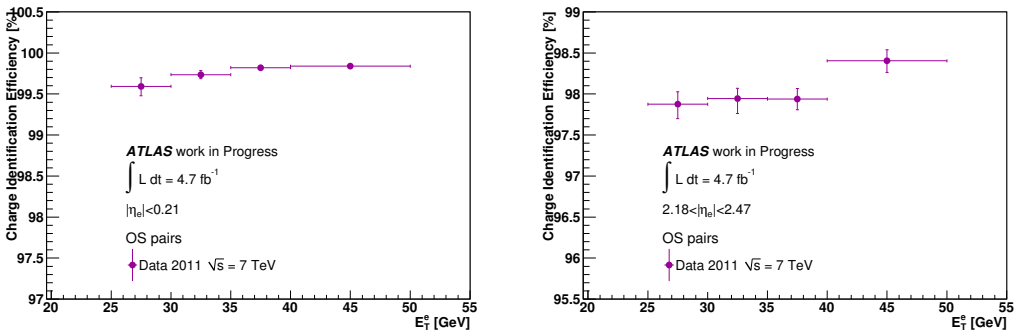

Figure 7.2: Charge-blind identification rates for the pseudorapidity region $|\eta| < 0.21$ (*left*) and $2.18 < |\eta| < 2.47$ (*right*). The charge identification is slightly lower for low E_T electrons*. Similar results are obtained in the other η bins.

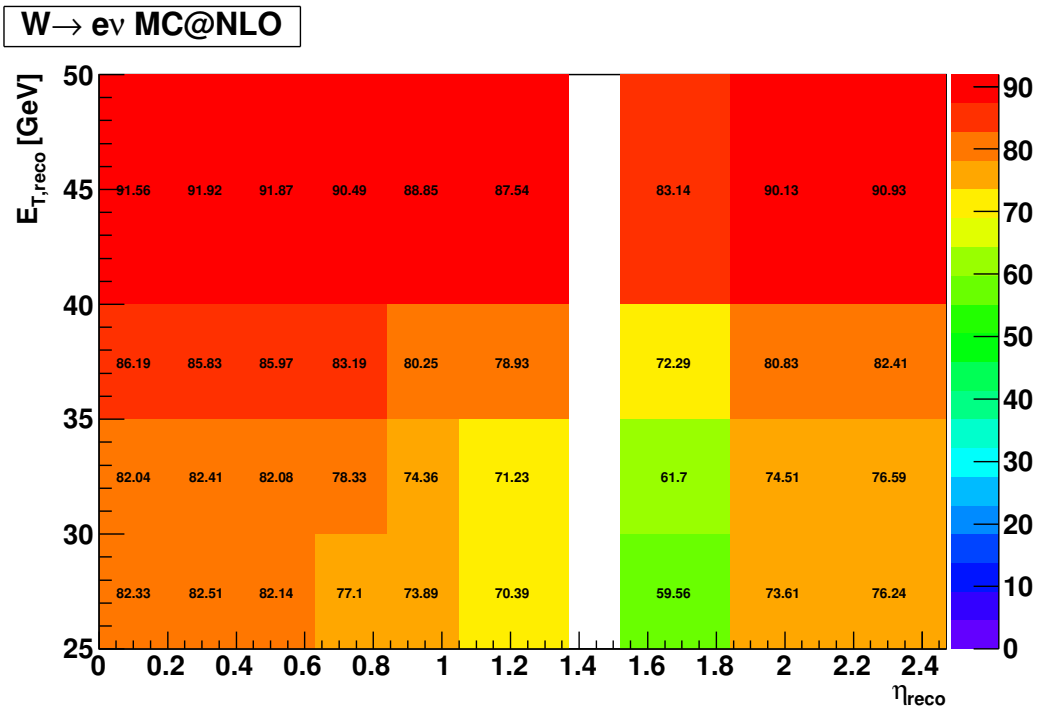

Figure 7.3: Purity of the signal sample for the E_T and $|\eta|$ bins used in this analysis.

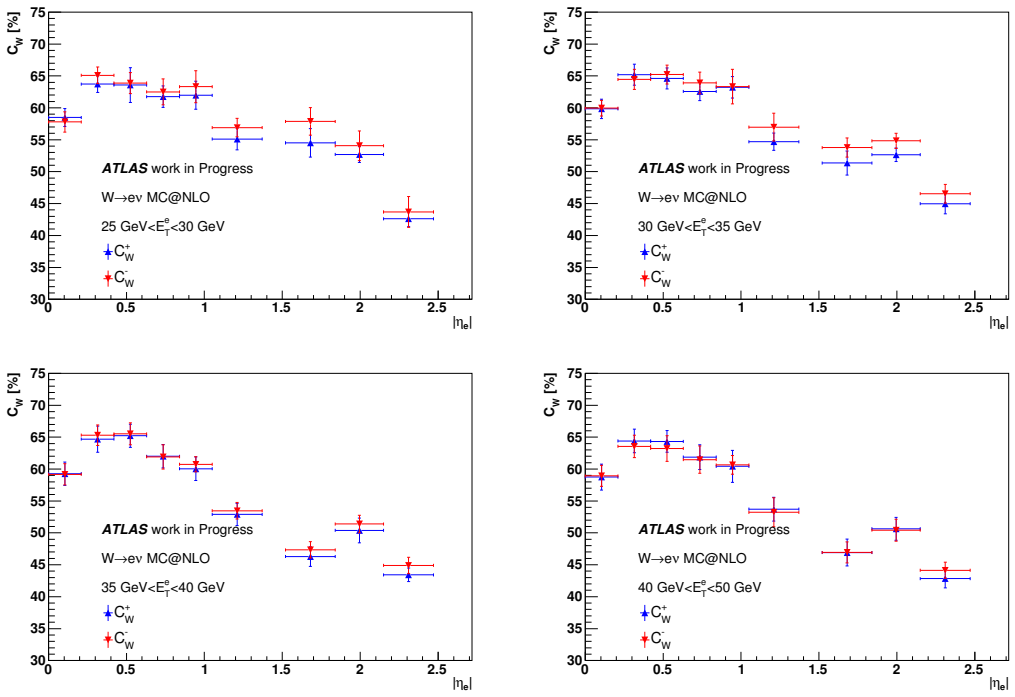

Figure 7.4: C_W correction factors for electrons (*red*) and positrons (*blue*) as a function of the electron pseudorapidity for the four different E_T bins. The error bars represent both statistical and systematic uncertainties.

7.2 W Cross-section Measurement

Using the cross-section formula shown in eq. 6.4, the first measurement of the double differential cross-section times the branching ratio for $W^+ \to e^+\nu$ and $W^- \to e^-\bar{\nu}$ is obtained in the ATLAS experiment. Fig. 7.5 shows the cross-section for W^+ and W^- as a function of the electron pseudorapidity in bins of the E_T of the electron. The luminosity uncertainty is at the level of 3.9%.

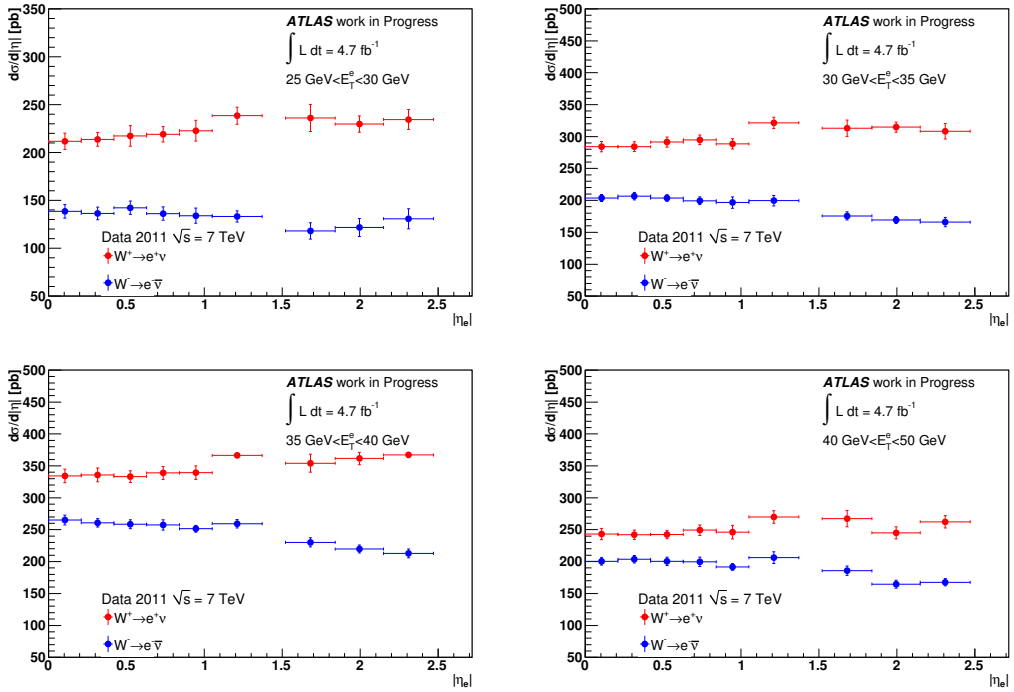

Figure 7.5: Double differential cross-section measurement for W^+ and W^- production. Each plot shows the cross-section as a function of the electron pseudorapidity for different bins of the electron transverse energy. The results are normalised to the bin size. The luminosity uncertainty is not included.

As for the single differential measurement, the cross-sections obtained as a function of the electron pseudorapidity and of E_T are compared to the NLO theoretical prediction of MSTW2008 and NLO PDF sets. The results are presented in Fig. 7.6 and Fig. 7.7 for the W^+ and W^- bosons respectively.

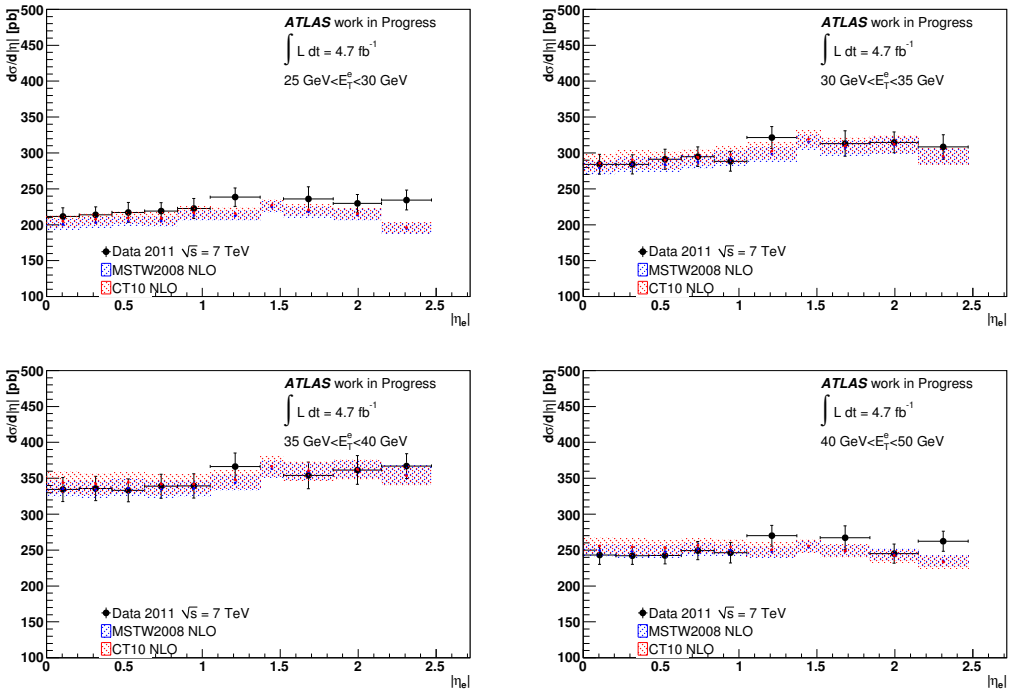

Figure 7.6: Double differential measurement for the W^+ cross-section and its comparison to the theoretical prediction. The MSTW2008 and CT10 PDF predictions are shown at NLO. The results are presented as a function of the positron pseudorapidity for four different E_T regions.

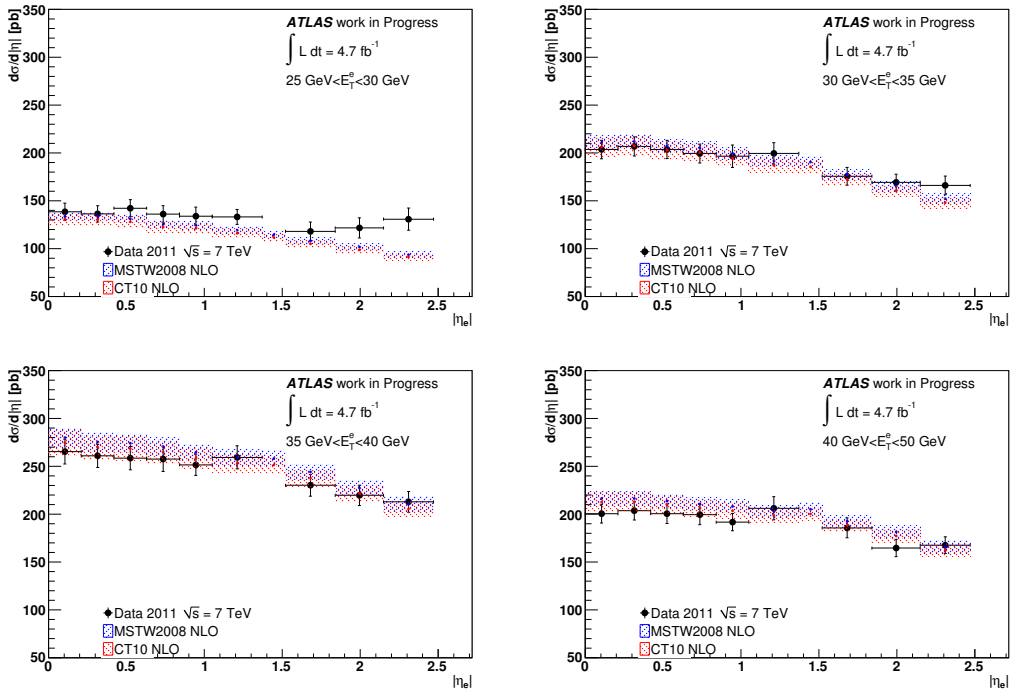

Figure 7.7: Double differential measurement for the W^- cross-section and its comparison to the theoretical prediction. The MSTW2008 and CT10 PDF predictions are shown at NLO. The results are presented as a function of the electron pseudorapidity for four different E_T regions.

7.3 W Charge Asymmetry Measurement

Using the W^+ and W^- cross-sections measured in the previous section, the W charge asymmetry can also be derived as:

$$A_l(\eta, E_T) = \frac{\frac{d^2\sigma_{W^+}}{d\eta dE_T} - \frac{d^2\sigma_{W^-}}{d\eta dE_T}}{\frac{d^2\sigma_{W^+}}{d\eta dE_T} + \frac{d^2\sigma_{W^-}}{d\eta dE_T}}.$$

Fig. 7.8 shows the results of the double differential W charge asymmetry with the full statistical and systematic uncertainty. The uncertainty is at the level of $\sim 2-3\%$ though for some bins it reaches the level of $\sim 7\%$ as seen in the figure. From the plots in Fig. 7.8, it is observed that the charge asymmetry decreases for high E_T electrons. The predictions of the MSTW2008, CT10 and HERAPDF1.5 PDF sets are also shown at next-to-leading order.

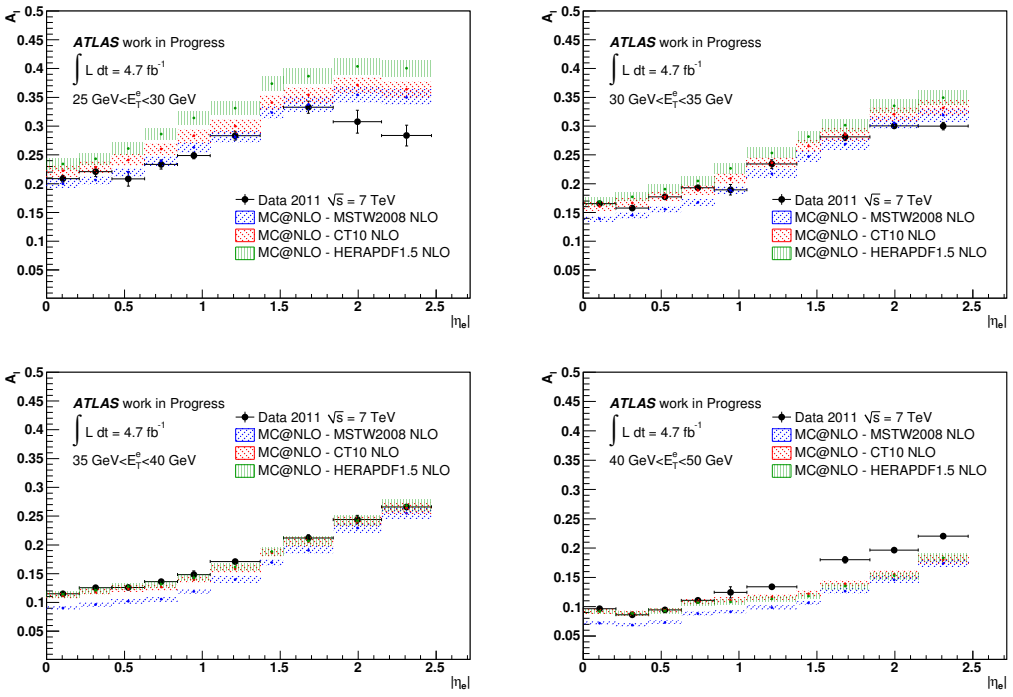

Figure 7.8: Double differential W charge asymmetry measurement as a function of $|\eta|$ and E_T. In each of the plots the W charge asymmetry is shown as a function of the electron pseudorapidity for different bins of the electron transverse energy. Both statistical and systematic uncertainties are considered. The theoretical prediction given by the MSTW2008 (*blue*), CT10 (*red*) and HERAPDF1.5 (*green*) PDF sets is also shown.

7.4 Conclusion

In summary, the first double differential measurement of the $W^+ \to e^+\nu$ and $W^- \to e^-\bar{\nu}$ cross-sections as a function of the charged lepton pseudorapidity and transverse energy performed with the ATLAS experiment has been presented in this chapter. The measurement uses the full 2011 data sample and is statistically limited. In addition to the W charge asymmetry measurement that was presented in the previous chapter, such analyses can be used to provide additional constraints and new PDF fits.

Bibliography

[1] `http://http://en.wikipedia.org/wiki/Standard_Model`

[2] C. Burgess and G. Moore, *The Standard Model: A primer*. Cambridge University Press, 2007.

[3] D.J. Griffith, *Introduction to Elementary Particles*. Wiley-VCH, 21 oct, 2008.

[4] P. Langacker, *The Standard Model and Beyond*. CRC Press, 2010.

[5] D.P Barber et al., *Discovery of Three Jet Events and a Test of Quantum Chromodynamics at PETRA Energies*. Phys. Rev. Lett. 43 830, 1979.

[6] A. Pich, *Aspects of Quantum Chromodynamics*. hep-ph/0001118v1, 2000.

[7] R.K Ellis, W.J. Stirling and B.R. Webber, *QCD and Collider Physics*. Cambridge University Press, 1996.

[8] C.S. Wu et al., *Experimental test of parity conservation in beta decay*. Phys. Rev. 105 1413–1414, 1957.

[9] S. Weinberg, *A Model of Leptons*. Phys. Rev. Lett. 19 1264–1266, 1967.

[10] S.L Glashow, *Partial Symmetries of Weak Interactions*. Nucl. Phys. 22 579–588, 1961.

[11] A. Salam, Abdus and J.C. Ward, *Electromagnetic and weak interactions*. Phys. Lett. 13 168–171, 1964.

[12] S.D. Drell and Tung-Mow Yan, *Partons and their applications at high energies*. Ann. Phys. 66:578, 1971.

[13] G. Altarelli and G. Parisi, *Asymptotic freedom in parton language*. Nucl. Phys. B126:298, 1977.

[14] M.Aharrouche et al., *Double differential Z, W cross sections and their ratios in the electron channels*. ATL-PHYS-INT-2011-081, 2011.

[15] A.D. Martina et al., *Parton distributions for the LHC*. hep-ph/0901.0002v3, 2009.

[16] S. Alekhin et al., *Parton distribution functions and benchmark cross sections at NNLO*. hep-ph/1202.2281v1, 2012.

[17] R. Plunkett for the CDF Collaboration, *High E_T jets at CDF*. Nucl. Phys. B 54A 81-85, 1997.

[18] A.D. Martin et al., *Parton Distributions and the LHC: W and Z Production*. hep-ph/9907231v1, 1999.

[19] J.M. Campbell et al., *Hard Interactions of Quarks and Gluons: a Primer for LHC Physics*. hep-ph/0611148v1, 2006.

[20] K. Nakamura et al. (Particle Data Group), *Review of Particle Physics*. J. Phys. G37, 2010. `http://pdg.lbl.gov`

[21] The UA1 Collaboration, *Intermediate Vector Boson Cross-Sections at the CERN Super Proton Synchrotron Collider and the Number of Neutrino Types*. Phys. Lett., B198:271, 1987.

[22] The UA2 Collaboration, *A Measurement of the W and Z production crosssections and a determination of Γ_W at the CERN $\bar{p}p$*. Phys. Lett. B276:365, 1992.

[23] The CDF Collaboration, *Measurement of $\sigma \cdot B(W \to e\nu)$ and $\sigma \cdot B(Z^0 \to e^+e^-)$ in $p\bar{p}$ collisions at $\sqrt{s} = 1.8$ TeV*. Phys. Rev. Lett. 76:3070, 1996.

[24] The CDF Collaboration, *Measurements of Inclusive W and Z Cross Sections in $p\bar{p}$ collisions at $\sqrt{s} = 1.96$ TeV*. J. Phys. G34:2457-2544, 2007.

[25] The *D*0 Collaboration, *Extraction of the width of the W boson from measurements of $\sigma(p\bar{p} \to W + X) \times B(W \to e\nu)$ and $\sigma(p\bar{p} \to Z + X) \times B(Z \to ee)$ and their ratio*. Phys. Rev. D61:072001, 2000.

[26] The PHENIX Collaboration. Cross Section and Parity Violating Spin Asymmetries *Cross Section and Parity Violating Spin Asymmetries of $W^{\pm}$ Boson Production in Polarized $p + p$ collisions at $\sqrt{s} = 500$ GeV*. hep-ex/1009.0505, 2010.

[27] The ATLAS Collaboration, *Measurement of the $W \to l\nu$ and $Z/\gamma^* \to ll$ production cross sections in proton-proton collisions at $\sqrt{s} = 7$ TeV with the ATLAS detector*. hep-ex/010.2130v1, 2010.

[28] The CDF Collaboration, *Measurement of the lepton charge asymmetry in W boson decays produced in $p\bar{p}$ collisions*. Phys. Rev. Lett. 81:5754-5759, 1998.

[29] The CDF Collaboration, *Measurement of the forward-backward charge asymmetry of electron positron pairs in $p\bar{p}$ collisions at $\sqrt{s} = 1.96$ TeV*. Phys. Rev. D71:052002, 2005.

[30] The *D*0 Collaboration, *Measurement of the electron charge asymmetry in $p\bar{p} \to W + X \to e\nu + X$ eventd at $\sqrt{s} = 1.96$ TeV*. Phys. Rev. Lett. 101:211801, 2008.

[31] The *D*0 Collaboration, *Measurement of the muon charge asymmetry from W boson decays*. Phys. Rev. D77:011106, 2008.

[32] The *D*0 Collaboration, *Measurement of the muon charge asymmetry in* $p\bar{p} \to W + X \to \mu\nu + X$ *events using the D*0 *detector*. Note 5976-CONF, 2006.

[33] The CDF Collaboration, *Direct Measurement of W Boson Charge Asymmetry with 1* fb^{-1} *of Run II Data*. CDF note 8942, 2008.

[34] The ATLAS Collaboration, *The ATLAS Experiment at the CERN Large Hadron Collider*. JINST 3 S08003, 2008.

[35] The ATLAS Collaboration, *A measurement of the material in the ATLAS inner detector using secondary hadronic interactions*. hep-ex/1110.6191v1, CERN-PH-EP-2011-147, 2001.

[36] The ATLAS Collaboration, *Improved electron reconstruction in ATLAS using the Gaussian Sum Filter-based model for bremsstrahlung*. ATLAS-CONF-2012-047, 2012.

[37] The ATLAS Collaboration, *ATLAS Calorimeter Performance*. CERN/LHCC/96-40, 1996.

[38] The ATLAS Collaboration, *ATLAS Liquid Argon Calorimeter Technical Design Report*. CERN/LHCC/96-41, 1996.

[39] A. Bazan et al., *ATLAS liquid argon calorimeter back end electronics*. JINST 2 P06002, 2007.

[40] N.J. Buchanan et al, *Design and implementation of the Front End Board for the readout of the ATLAS liquid argon calorimeters*. JINST 3 P09003, 2008.

[41] M. Aurousseau et al., *Validation of the LAr Calorimeter DSP Physics code*. ATL-COM-LARG-2009-045, 2010.

[42] L. Courneyea et al., *Computation and validation of the electronic calibration constants for the ATLAS Liquid Argon Calorimeters*. ATL-LARG-INT-2010-007, 2010.

[43] J. Colas et al., *Electronics calibration board for the ATLAS liquid argon calorimeters*. NIM A 593 269-291, 2008.

[44] M. Aleksa et al., *ATLAS Combined Testbeam: Computation and Validation of the Electronic Calibration Constants for the Electromagnetic Calorimeter*. ATL-LARG-PUB-2006-003, 2006.

[45] W. Lampl et al., *Calorimeter Clustering Algorithms: Description and Performance*. ATL-LARG-PUB-2008-002, 2008.

[46] M. Aharrouche et al., *Measurement of the response of the ATLAS liquid argon barrel calorimeter to electrons at the 2004 combined test-beam*. NIM A 614 400-432, 2010.

[47] The ATLAS Collaboration, *Reconstructed $Z \to e^+e^-$ invariant mass after electron energy calibration*. ATL-COM-PHYS-2011-1637, 2011.

[48] The ATLAS Collaboration, *Expected Performance of the ATLAS Experiment: Detector, Trigger and Physics*. CERN-OPEN-2008-020, 2008.

[49] D. Banfi et al., *The determination of the energy of electrons and photons in the ATLAS electromagnetic calorimeters*. ATL-PHYS-INT-2010-038, 2010.

[50] The ATLAS Collaboration, *Electron and photon reconstruction and identification in ATLAS: expected performance at high energy and results at 900 GeV*. ATLAS-CONF-2010-005, 2010.

[51] The ATLAS Collaboration, *Electron performance measurements with the ATLAS detector using the 2010 LHC proton-proton collision data*. Eur. Phys. J. C 1909, 2012.

[52] The ATLAS Collaboration, *Reconstruction and Calibration of Missing Transverse Energy and Performance in Z and W events in ATLAS Proton-Proton Collisions at $\sqrt{s} = 7$ TeV*. ATLAS-CONF-2011-080, 2011.

[53] The ATLAS Collaboration, *Performance of the ATLAS Electron and Photon Trigger in p-p Collisions at $\sqrt{s} = 7$ TeV in 2011*. ATLAS-CONF-2012-048, 2012.

[54] J.M. Butterworth et al., *Single Boson and Diboson Production Cross Sections in pp Collisions at $\sqrt{s} = 7$ TeV*. ATL-COM-PHYS-2010-695, 2010.

[55] L. Di Ciaccio et al., *A measurement of the transverse momentum distribution of Drell-Yan lepton pairs at $\sqrt{s} = 7$ TeV using the φ^*_η variable with ATLAS*. ATL-COM-PHYS-2012-472, 2012.

[56] R. Gavin et al., *W physics at the LHC with FEWZ 2.1*. hep-ph/1201.5896v1, 2012.

[57] The ATLAS Collaboration, *Measurement of the inclusive $W^\pm$ and Z/γ^* cross sections in the e and μ decay channels in pp collisions at $\sqrt{s} = 7$ TeV with the ATLAS detector*. hep-ex/1109.5141v2, 2011.

[58] The ATLAS Collaboration, *Determination of the strange quark density of the proton from ATLAS measurements of the $W \to l\nu$ and $Z \to ll$ cross sections*. hep-ex/1203.4051, 2012.

[59] The CMS Collaboration, *Measurement of the Lepton Charge Asymmetry in Inclusive W Production in pp Collisions at $\sqrt{s} = 7$ TeV*. JHEP 1104:050, 2011.

[60] The LHCb Collaboration, *W and Z production at $\sqrt{s} = 7$ TeV with the LHCb experiment*. LHCb-CONF-2011-012, 2011.

[61] The ATLAS Collaboration, *An extrapolation to a larger fiducial volume of the measurement of the W charge asymmetry in proton-proton collisions at $\sqrt{s} = 7$ TeV with the ATLAS detector: Graphical comparison between ATLAS, CMS and LHCb*. ATLAS-CONF-2011-129, 2011.

[62] E. Rizvi, *Experimental Methods in Particle Physics*. `http://pdg.lbl.gov`